Journal of Modern Engineering
International
WWW.IJME.US
Print ISSN: 2157-8052
Online ISSN: 1930-6628

INTERNATIONAL JOURNAL OF MODERN ENGINEERING

Fall/Winter 2016
Volume 17, No. 1

The Leading Journal of Engineering, Applied Science and Technology

Industrial Electronics

Biomedical Civil Aerospace

Computer

Electrical

Chemical

Mechanical

ENGINEERING

THE LEADING JOURNAL OF ENGINEERING, APPLIED SCIENCE, AND TECHNOLOGY

Print ISSN: 2157-8052
Online ISSN: 1930-6628

www.ijme.us

www.iajc.org

INTERNATIONAL JOURNAL OF MODERN ENGINEERING

ABOUT IJME:

- IJME was established in 2000 and is the first and official flagship journal of the International Association of Journal and Conferences (IAJC).
- IJME is a high-quality, independent journal steered by a distinguished board of directors and supported by an international review board representing many well-known universities, colleges and corporations in the U.S. and abroad.
- IJME has an impact factor of **3.00**, placing it among the top 100 engineering journals worldwide, and is the #1 visited engineering journal website (according to the National Science Digital Library).

OTHER IAJC JOURNALS:

- The International Journal of Engineering Research and Innovation (IJERI)
  For more information visit www.ijeri.org
- The Technology Interface International Journal (TIIJ).
  For more information visit www.tiij.org

IJME SUBMISSIONS:

- Manuscripts should be sent electronically to the manuscript editor, Dr. Philip Weinsier, at philipw@bgsu.edu.

  For submission guidelines visit www.ijme.us/submissions

TO JOIN THE REVIEW BOARD:

- Contact the chair of the International Review Board, Dr. Philip Weinsier, at philipw@bgsu.edu.

  For more information visit www.ijme.us/ijme_editorial.htm

INDEXING ORGANIZATIONS:

- IJME is currently indexed by 22 agencies. For a complete listing, please visit us at www.ijme.us.

Contact us:

Mark Rajai, Ph.D.

Editor-in-Chief
California State University-Northridge
College of Engineering and Computer Science
Room: JD 4510
Northridge, CA 91330
Office: (818) 677-5003
Email: mrajai@csun.edu

www.tiij.org

www.ijeri.org

INTERNATIONAL JOURNAL OF MODERN ENGINEERING

The INTERNATIONAL JOURNAL OF MODERN ENGINEERING (IJME) is an independent, not-for-profit publication, which aims to provide the engineering community with a resource and forum for scholarly expression and reflection.

IJME is published twice annually (fall and spring issues) and includes peer-reviewed research articles, editorials, and commentary that contribute to our understanding of the issues, problems, and research associated with engineering and related fields. The journal encourages the submission of manuscripts from private, public, and academic sectors. The views expressed are those of the authors and do not necessarily reflect the opinions of the IJME editors.

EDITORIAL OFFICE:

Mark Rajai, Ph.D.
Editor-in-Chief
Office: (818) 677-2167
Email: ijmeeditor@iajc.org
Dept. of Manufacturing Systems Engineering & Management
California State University-Northridge
18111Nordhoff Street
Northridge, CA 91330-8332

THE INTERNATIONAL JOURNAL OF MODERN ENGINEERING EDITORS

TABLE OF CONTENTS

In This Issue (p.31)
Connecting a Photovoltaic System to the Electrical Grid in a Humid Subtropical Climate

Philip Weinsier, IJME Manuscript Editor

Not that long ago, when asking the average homeowner about photovoltaic (PV) systems, your reply could be expected to range from a blank stare to a confident, "Sure, I've heard about them!" At that time, perhaps only two decades ago or so, PV systems represented an expense that, again, the average homeowner could only gawk at. But there were plenty of well-to-do individuals, who could afford such systems. So why weren't more systems dotting the U.S. landscape? That likely was due to the fact that the older systems were inefficient and either could not connect to the distribution grid or the additional costs to do so were such that the return on investment just didn't compute. Nor were regulatory agencies and government giving the industry much consideration or respect by way of safety regulations.

As if those weren't reasons enough for avoiding involvement with PVs, homeowners also had to take into account their environment—where they lived, average temperature, irradiation levels, amount of sunlight available throughout the year, effects of snow and clouds, type of PV system to buy and its efficiency and $/watt costs. Should I buy monocrystalline, polycrystalline, amorphous, CdTe (cadmium telluride), or CIS/CIGS (coper indium gallium selenide)?

Today, though, is quite another matter. State-of-the-art systems are worth considering; you no longer have to be quite so well-to-do as before, especially if you are willing to invest the time to apply for state/federal rebates. There are also more safety regulations covering installation of PV systems, plus there's no shortage of companies ready to install one for you. For the most part, they are also now rather well-versed on what type of system you should buy, given all of the factors that I noted above. But at the end of the proverbial day, what does a system save you? After all, if there are no savings down the road, why bother? Looking at some of the advertising from PV companies, you can expect to pay (2016) between $3 and $4 per watt to install your system, with the average system in the U.S. weighing in at about 5kW (5000 watts). So, you can expect to lay out $10,000 to $20,000; not exactly chump change.

And what does such an outlay get you? Start by focusing on the long-term; you likely will have to wait a good seven years before you start recognizing some savings. But, over the next 13 years (assuming a 20-year lifespan of your system), you can likely double or triple your investment in savings. That does, of course, depend on where you live: The west coast and upper east coast will generally return your money faster and save you more in the long-run.

But there's more to the story than just how good such a system might be on your pocketbook. We also need to take into account the limited resources available in the way of fossil fuels that the world is burning through—literally and figuratively. At some point, we just have to get on one bandwagon or another and help move the world towards renewable energy resources. For more on this topic, I direct your attention to the article on p.31 in which the authors describe their research aimed at determining the measured and predicted performance of a photovoltaic grid-connected system. By predicted system performance, I mean the authors also developed a computer model of their system and compared the results to experimentally collected data. Finally, the research allowed for long-term simulation analysis of the system under varying conditions that would assist designers with the optimization of the PV system.

Editorial Review Board Members

HIGH-SPEED PERMANENT-MAGNET GENERATOR WITH OPTIMIZED SIZING BASED ON PARTICLE SWARMS FOR SMART GRIDS

Adel El Shahat, Georgia Southern University; Rami J. Haddad, Georgia Southern University;
Youakim Kalaani, Georgia Southern University

Abstract

High-speed, permanent-magnet (HSPM) types of micro-generators play an important role in power generation involving smart grid applications. In this study, the authors developed an optimized analytical design and compared it with an original machine design with a typical 500 kW tip-speed of 250 m/s. The two designs take into consideration multiple factors including classical sizing and problem formulation for optimizing efficiency with bounded constraints. A particle swarm optimization (PSO) algorithm was used to maximize efficiency as an objective or fitness function and to minimize machine size as a non-linear function with bounded parameter constraints. Particle swarm algorithms use population-based on flocks of birds or insects swarming. The parameter variables used for this type of optimization consist of rotor-length-to-diameter ratio, rotor radius, and stack length. Test results including simulations using PSO Tool in Matlab showed significant improvement in machine design and performance. Furthermore, it was observed that the proposed technique has the advantage of limiting losses at higher frequencies with low weight/volume applications, thereby improving overall efficiency. Other system parameters such as power factor were also improved. Finally, several analytical design problems with waveform variations, harmonics distortion, rotor losses, and effects of changing poles are provided to show the merit of the proposed optimization technique.

Introduction

There has been increased interest in smart grid and micro-grid connected systems, especially those dealing with onsite generation [1]. This is mainly due to the limitations in the use of traditional power plants heavily constrained by economic and environmental regulations [2]. Therefore, high-speed permanent-magnet (HSPM) micro-generators represent a viable and compact solution for onsite generation in smart grids and micro-grids. Length-to-diameter is the most important factor, defined as the rotor aspect ratio in high-speed applications [3]. Classical and optimum designs of HSPM generators have been studied for distributed power generation purposes [4]. In the case of a high-speed PM motor, temperature sensitivity of the magnetic materials is an additional, critical factor; therefore, a Samarium Cobalt (SmCo) magnet is often used to realize higher temperature designs [1-5]. In fact, there have been extensive studies dealing with HSPM design and applications [5-22].

In this current study, an optimized design process was developed and compared to the classical approach that uses a typical 500 kW output power generator at a tip speed of 250 m/s. These design methods take into consideration multiple factors, including classical sizing and problem formulation with the objective of optimizing efficiency with bounded constraints. The optimized set of variables used in this study were rotor-length-to-diameter ratio, rotor radius, and stack length. It was observed that this design approach had the potential to limit losses at high frequencies and low weight/volume, resulting in higher overall system efficiency. Other parameters like power factor and maximum ampere-torque ratio were also shown to improve. Finally, analytical design examples with waveform variations, harmonic distortion, rotor losses, and effects of changing poles were also provided to show the merit of the proposed optimization technique.

Classical Sizing

The overall power requirement for HSPM generators is usually within the range of 5-500 kW. The structural and thermal design of a permanent-magnet machine is highly affected by the selections of magnet, stator, and rotor materials. The sizing and performance of HSPM machines depend on the material properties of the permanent magnet [23]. The magnets should be selected in order to provide the required air gap magnetic field and ample coercive force [24].

Additional information regarding the characteristics of typical B-H curves can be found in the study by Hanselmann [25]. Rare earth magnets such as SmCo and NdFeB provide high performance when used in HSPM machines, due to greater power density, high coercivity, high flux densities, and linearity of the demagnetization curves [26]. NdFeB is preferred because it is cheaper and more readily available [27].

Usually, the rotor is built from the same material as the stator to simplify the manufacturing process. However, it is not uncommon to have stators made of economically viable materials such as steel [28]. Some of the most common materials used in the design of stators are low-carbon steels, silicon (Si) steels, nickel (Ni) alloy steels, and cobalt (Co) alloy steels [29]. The M19 is a 29-gauge electrical silicon steel used for its economic viability, thin laminations, and high saturation flux density, which is about 1.8 T [28].

Machine Design Parameters

The main aspect considered in this process is the stator mechanical design, which can be either a slotted or slotless design. Figure 1 shows the slotless stator, which has armature windings located in the air gap of the machine. Figure 2 shows the slotted stator, which has armature windings wound around the slots or teeth.

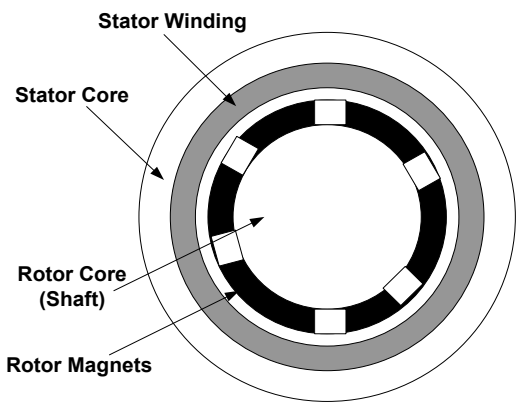

Figure 1. Slotless Stator Design

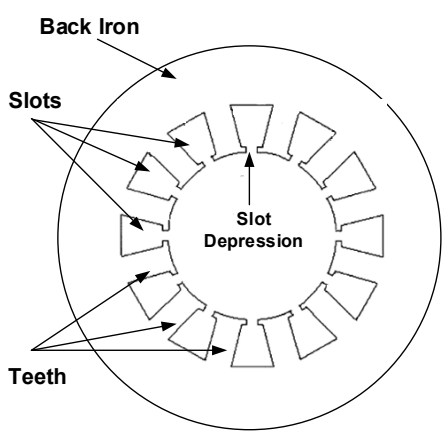

Figure 2. Slotted Stator Design

The overall performance of a slotless stator is always inferior to equivalent slotted stator designs; thus, the slotless stator design is not usually used in high-power applications. On the other hand, the slot openings in the slotted stator design provide a sturdy housing for the windings and their insulation. Figure 3 illustrates the stator slot geometry. A key design factor in the slotted stator is to minimize the difference between the slot depression width and the slot top width. In power applications requiring a high number of phases, 36-slot configurations are typically chosen for the initial machine design.

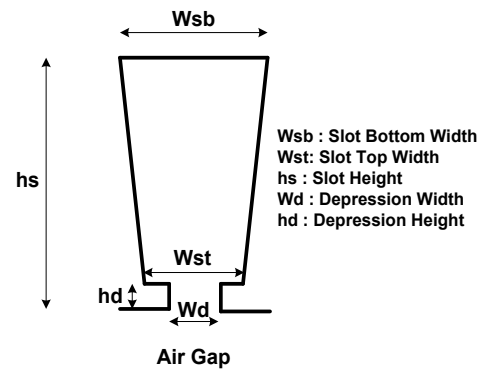

Figure 3. Stator Slot Geometry

Rotor aspect ratio, defined as length-to-diameter (L/D) ratio, is an important factor in high-speed applications. A typical L/D ratio for a wound rotor machine is around 0.5-1.0 compared to around 1-3 for a PM machine [30]. The machine tip speed, which is the surface velocity of the rotor, is governed by the rotational speed and rotor radius, as defined by Equation (1):

$$v_{tip} = r\omega_m \tag{1}$$

where, r is the rotor radius (m) and ω_m is the rotational angular speed (rad/sec).

The tip speed upper bound for most rotating machines is between 100 and 250 m/s, depending on its application and design [31]. In a balanced rotational design, the number of poles is determined by Equation (2):

$$N(2p) = 120f \tag{2}$$

where, N is speed (rpm); p is the number of pole pairs; and, f is the electrical-frequency (Hz).

For a given rotational speed, an efficient solution is to have a large number of poles and higher frequencies [26]. However, this might induce cogging torque and variations in the air gap reluctance, flux, and voltage waveforms. To resolve this issue, magnet poles are skewed to smooth out these variation. Skew-factor is defined by Equation (3):

$$k_{sn} = \frac{\sin(n\theta_s)}{\theta_s/2} \tag{3}$$

where, θ_s is the skew angle (rad) and n is the-harmonic number.

Using a first-order approximation, the air gap flux density, B_g, can be represented by Equation (4) [32]:

$$B_g = \frac{h_m}{h_m + g} B_r \tag{4}$$

where, h_m is the magnet height (mm); g is the air-gap (mm); and, B_r is the magnet remnant flux density (T).

In order to get uniform magnetic fields, the magnet height is usually larger than the air-gap by a factor of 5 to 10.

Power, current, and voltage ratings in an electric machine are determined by the number of phases, given by Equation (5):

$$|P + jQ| = q \times V \times I \tag{5}$$

where, P is the real power (W); Q is the reactive power (VAR); q is the number of phases; V is the RMS phase voltage (V); and, I is the RMS current (A).

The number of slots per pole per phase, m, is an important parameter when considering generator design and can be calculated using Equation (6):

$$m = \frac{N_s}{2 \times p \times q} \tag{6}$$

where, N_s is the number of slots; p is the pole pairs; and q is the number of phases.

A slot fill factor, λ_s, [26] is used to determine the extent to which the slot cross-sectional area is occupied by winding material, as defined by Equation (7):

$$\lambda_s = \frac{Winding\ Area}{Total\ Slot\ Area} \tag{7}$$

Overall, slot fill factors vary in value from 0.3-0.7 [26], depending on the number and size of the conductors in the slots. A slot fill factor of 0.5 was assumed for this current design.

Machine Calculated Parameters

Assuming the machine is balanced, parameters are determined on a per-phase basis and can be applied to all phases, as shown in Figure 4.

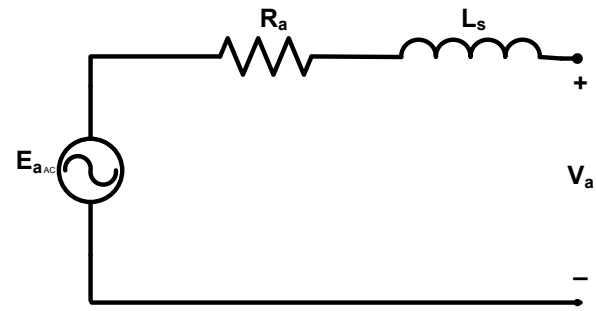

Figure 4. Per-Phase Model

The resistance of the copper phase windings, R_a, can be calculated using Equation (8):

$$R_a = \frac{l}{\sigma \times A} \tag{8}$$

where, l is the conductor length; σ is the winding conductivity; and, A is the winding cross-sectional area.

The conductor cross-sectional area, A_{ac}, can be obtained using the slot area and slot fill factor, as shown in Equation (9):

$$A_{ac} = \frac{A_s \times \lambda_s}{2 \times N_c} \tag{9}$$

where, A_s is the slot area and N_c is the number of turns per coil.

Figure 5 illustrated the power loss resulting from eddy currents in the slot conductors, which increases the resistance in the winding [33], and which can be determined by Equation (10):

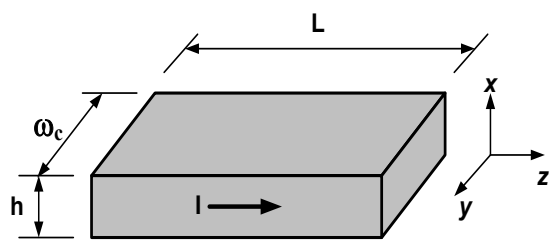

Figure 5. Rectangular Conductor Geometry

$$P_{ec} = \frac{1}{12} \sigma L \omega_c h^3 \omega^2 \mu_0^2 H_m^2 \tag{10}$$

where, H_m is the turn field intensity value and μ_0 is the free-space permeability.

Skin depth is defined by Equation (11):

$$\delta s = \sqrt{\frac{2}{\omega \mu_0 \sigma}} \tag{11}$$

And, Equation (10) can be rewritten as shown in Equation (12):

$$P_{ec} = \frac{L \omega_c h^3}{6 \sigma \delta^4} H_m^2 \tag{12}$$

Assuming that the slot conductors are distributed uniformly in the slot, the total slot eddy current loss can be calculated by substituting field intensity into Equation (12) and summing over all n_s conductors, as defined by Equation (13):

$$P_e = \left(\frac{d_s L h^2 n_s^2}{9 \sigma \delta^4 \omega_s} \right) I^2 \tag{13}$$

where, I is the RMS conductor current; ω_s is the slot width (m); and, d_s is the slot depth (m).

The single-slot resistance, R_{sl}, assuming n_s conductors connected in series, is given by Equation (14):

$$R_{sl} = \frac{\rho n_s^2 L}{k_{cp} \omega_s d_s} \tag{14}$$

where, L is the slot length; k_{cp} is the conductor packing factor, which is the ratio of cross-sectional area occupied by conductors to the entire slot area; and, ρ is the electrical resistivity (Ω.m).

Using Equation (14), the total slot resistance, R_{st}, can be rewritten as Equation (15):

$$R_{st} = R_{sl} + R_{ec} = R_{sl}\left(1 + \Delta_e\right) \tag{15}$$

In Equation (15), $\Delta_e = R_{ec}/R_{sl}$ is a frequency-dependent term. Using Equations (13) and (14), this term can be simplified and rewritten as Equation (16):

$$\Delta_e \equiv \frac{R_{ec}}{R_{sl}} = \frac{1}{9}\left(\frac{d_s}{\delta}\right)^2 \left(\frac{h}{\delta}\right)^2 \tag{16}$$

Winding factor, k_w, is the ratio of flux linked by an actual winding to the flux linked by a full-pitch concentrated-factor, k_p, and a breadth/distribution factor, k_b, as shown in Equation (17):

$$k_{wn} = k_{pn} \times k_{bn} \tag{17}$$

The pitch-factor can then be derived, with the final result shown in Equation (18):

$$k_{pn} = \sin\left(\frac{n \times \alpha}{2}\right) \times \sin\left(\frac{n \times \pi}{2}\right) \tag{18}$$

where, n is the harmonic number and α is the short pitch coil, as illustrated in Figure 6.

A phase winding normally consists of a large number of coils linking flux slightly out of phase with each other, as shown in Figure 7.

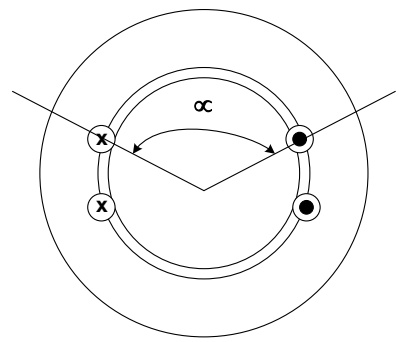

Figure 6. Short-Pitch Coil

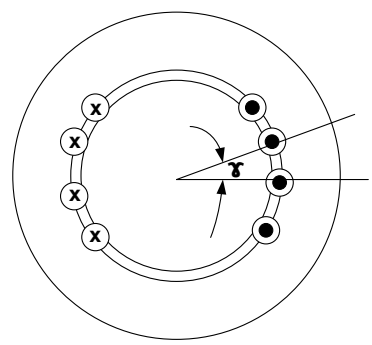

Figure 7. Winding Breadth

Equation (19) can be used to derive the breadth factor either magnetically or geometrically:

$$k_{bn} = \frac{\sin\left(\frac{n \times m \times \gamma}{2}\right)}{m \times \sin\left(\frac{n \times \gamma}{2}\right)} \tag{19}$$

where, m is the number of slots per pole per phase and γ is the electrical angle of the coil.

Equation (20) is the equation for a slotted stator, surface magnet configuration:

$$k_{gn} = \frac{R_i^{\,n_p-1}}{R_s^{\,2n_p} - R_i^{\,2n_p}} \times \left[\left(\frac{n_p}{n_p+1} \right) \times \left(R_2^{\,n_p+1} - R_1^{\,n_p+1} \right) + \frac{n_p}{n_p-1} \times R_s^{\,2n_p} \times \left(R_1^{\,1-n_p} - R_2^{\,1-n_p} \right) \right] \tag{20}$$

where, R_s is the outer magnetic boundary; R_2 is the outer boundary of the magnet; R_i is the inner magnetic boundary; and, R_1 is the inner boundary of the magnet.

$R_s = R + h_m + g$

$R_i = R_1 = R$

$R_2 = R + h_m$

The air gap flux density is also affected by the magnet geometry in the air gap, as depicted by Equation (20). Since the magnet poles rotate north/south, the air gap flux density shape can be approximated using Equations (21)-(25) and is illustrated in Figure 8.

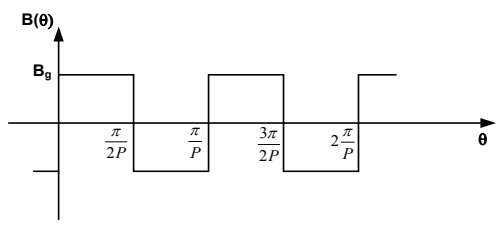

Figure 8. Air Flux Density

$$k_c = \left[1 - \frac{1}{\frac{\tau_s}{w_t} \times \left(5 \times \frac{g}{w_s} + 1 \right)} \right]^{-1} \tag{21}$$

where, w_s is the average slot width; w_t is the tooth width; $\tau_s = w_s + w_t$; and, $w_s = (w_{st} + w_{sb}) / 2$;

$$g_e = k_c \times g \tag{22}$$

where, g_e is the effective air gap;

$$PC = \frac{h_m}{g_e \times C_\phi} \tag{23}$$

where, PC is the permeance coefficient and C_φ is the flux concentration factor (Am/Ag)= $\frac{p \times \theta_m}{180}$;

$$B_g = \frac{k_r C_\phi}{1 + k_r \times \frac{\mu_{rec}}{PC}} B_r \tag{24}$$

where, μ_{rec} is the recoil permeability; B_r is the remnant flux density (T); and, k_r is the reluctance factor;

$$B(\theta) = \sum_{\substack{n=1 \\ nodd}}^{\infty} B_n \times \sin(np\theta)$$

$$B_n = \frac{4}{n\pi} \times B_g \times k_{gn} \times \sin\left(\frac{np\theta_m}{2} \right) \times \sin\left(\frac{n\pi}{2} \right) \tag{25}$$

and where, θ_m is the magnet physical angle.

Assuming the radial flux through coil, B_{flux}, is sinusoidally distributed—Equation (26)—the peak flux, φ_{pk}, for this ideal coil is given by Equation (27):

$$\phi = \int_0^{\frac{\pi}{P}} B_{flux} \times R_s \times L_{st} d\theta \tag{26}$$

$$\phi_{pk} = \frac{2 \times R_s \times L_{st} \times B_{flux}}{p} \tag{27}$$

Through Faraday's Law, the back EMF, E_a, for the machine is given by Equation (29):

$$\lambda(\theta) = \sum_{\substack{n=1 \\ nodd}}^{\infty} \lambda_n \times \sin(np\theta) \tag{28}$$

where,

$$\lambda_n = \frac{2 \times R_s \times L_{st} \times N_a \times B_n \times k_{wn} \times k_{sn}}{p}$$

$$E_a = \sum_{\substack{n=1 \\ nodd}}^{\infty} V_n \times \sin(np\theta) \tag{29}$$

and where,

$$V_n = \frac{d}{dt} \lambda_n = \omega_0 \times \lambda_n$$

The fundamental components are used to determine the internal voltage of the generator, as depicted in Equations (30) and (31) [4, 33, 34]:

$$B_1 = \frac{4}{\pi} \times B_g \times k_g \times \sin\left(\frac{p\theta_m}{2} \right) \tag{30}$$

$$\lambda = \frac{2 \times R_s \times L_{st} \times N_a \times k_w \times k_s \times B_1}{p}$$

$$E_a = \omega_0 \times \lambda \tag{31}$$

The number of armature turns, N_a, can be found using Equation (32), assuming that each slot has two half coils.

$$N_a = 2 \times p \times N_c \tag{32}$$

where, N_c is the number of turns per coil.

The vector relationship, illustrated in Figure 9, between the terminal voltage, V_a, internal voltage, E_a, and the synchronous reactance voltage drop is utilized to obtain Equation (33) [35]:

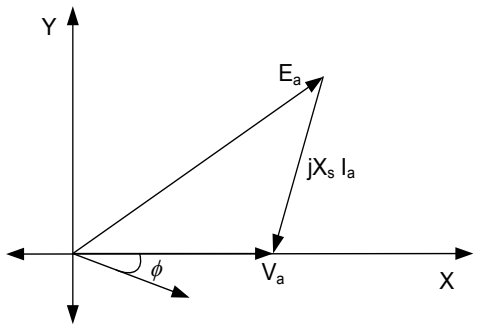

Figure 9. Phasor Relationship

$$V_a = \sqrt{E_a^{\,2} + (X_s \times I_a \times \cos\phi)^2} + X_s \times I_a \times \sin\phi \tag{33}$$

where,

$$I_a = \frac{P_{input}}{q \times V_a \times \cos\phi} \tag{34}$$

By substituting Equation (34) into Equation (33), assuming $\cos\phi = 0.99999 \cong 1$, and performing some mathematical simplification, the terminal voltage, V_a, can be derived from the resulting quadratic equation, as shown in Equation (35):

$$V_a^{\,2} = E_a^{\,2} + X_s^{\,2} I_a^{\,2} = E_a^{\,2} + X_s^{\,2} \frac{P_{input}^{\,2}}{9\left(V_a^{\,2}\right)}$$

$$V_a^{\,4} - E_a^{\,2} V_a^{\,2} - X_s^{\,2} \frac{P_{input}^{\,2}}{9} = 0$$

with,

$$BB = E_a^{\,2}$$

$$CC = X_s^{\,2} P_{input}^{\,2} / 9$$

$$V_a^{\,4} - BB V_a^{\,2} - CC = 0$$

where,

$$V_a = \sqrt{\frac{BB + \sqrt{BB^2 + 4CC}}{2}} \tag{35}$$

and where, the air gap power can be calculated using Equation (36):

$$P_{air\ gap} = 3E_a I_a = T_e \omega_s = P_{wr} + P_{core} + P_{windage} \tag{36}$$

To calculate the air gap inductance, a full-pitch, concentrated winding carrying a current, I, is initially examined, which leads to an air gap flux density determined by Equation (37) [33]:

$$B_{flux} = \sum_{\substack{n=1 \\ n\ is\ odd}}^{\infty} B_n \times \sin(np\theta)$$

$$B_n = \frac{4}{n\pi} \times \frac{\mu_0}{(g + h_m)} \times \frac{N_a \times I}{2p} \tag{37}$$

The air gap flux density becomes

$$B_n = \frac{q}{2} \times \frac{4}{n\pi} \times \frac{\mu_0}{(g + h_m)} \times \frac{N_a \times I}{2p}$$

The flux can be found using Equation (26) and the total flux linkage is $\lambda = Na\ \phi$. With all real winding effects included, the air gap inductance is then given by Equation (38):

$$L_{ag} = \frac{\lambda}{i} = \frac{q}{2} \times \frac{4}{n\pi} \times \frac{\mu_0 \times R_s \times L_{st} \times N_a^{\,2} \times k_{wn}^{\,2}}{n^2 \times p^2 \times (g + h_m)} \tag{38}$$

Assuming that the slot is rectangular with slot depressions as illustrated, in Figure 4, this results in a slot permeance per unit length given by Equation (39) [25, 34]:

$$Perm = \frac{1}{3} \times \frac{h_s}{w_{st}} + \frac{h_d}{w_d} \tag{39}$$

Equations (40)-(42), assuming m slots per pole per phase and a standard double-layer winding, show the slot leakage inductance for self, mutual, and 3-phase windings, respectfully:

$$L_{as} = 2 \times p \times L_{st} \times Perm \times [4 \times N_c^{\,2}\left(m - N_{sp}\right) + 2 \times N_{sp} \times N_c^{\,2}] \tag{40}$$

$$L_{am} = 2 \times p \times L_{st} \times Perm \times N_{sp} \times N_c^{\ 2} \quad (41)$$

$$L_{slot} = L_{as} - L_{am} \quad (42)$$

$$L_{slot} = L_{as} - 2 \times L_{am} \times \cos\left(\frac{2\pi}{q}\right) \quad \text{(higher-odd-phases)}$$

From the work by Hanselmann [33], the total end-turn inductance per phase can be defined by Equation (43):

$$L_e = \frac{\mu_0 \times N_c \times N_a^{\ 2} \times \tau_s}{2} \times \ln\left(\frac{\tau_s \times \pi}{\sqrt{2 \times A_s}}\right) \quad (43)$$

The total inductance for the phase is the sum of the three inductances and is given by Equation (44):

$$L_s = L_{ag} + L_{slot} + L_e, \qquad X_s = \omega_0 \times L_s \quad (44)$$

Basic Losses

Empirical data for M-19 (29-gauge material) were obtained. An exponential curve fit was then applied to the data in order to obtain an equation for estimating the core losses, as defined by Equations (45)-(47) [26]:

$$P_C = P_0 \times \left(\frac{B}{B_0}\right)^{\varepsilon B} \times \left(\frac{f}{f_0}\right)^{\varepsilon f} \quad (45)$$

$$P_{R_c}(\omega) = \frac{V_a^2}{R_c} \quad (46)$$

$$R_c(\omega) = \frac{3\pi^2 L_{st}^{\ 2} N_a^2 \sqrt{\omega}}{8 c_{Fe} k_{Fe} \left(\frac{1}{\omega_0}\right)^{1.5} \left(\frac{1}{B_0}\right)^2 \left[m_{st}\left(\frac{p\beta_{slot}}{b_{st}}\right)^2 + m_{sy}\left(\frac{1}{h_{sy}}\right)^2\right]} \quad (47)$$

where, R_c is the core resistance; c_{Fe} is the correction factor for the iron-loss calculation; b_{st} is the stator tooth width; k_{Fe} is the specific iron loss; m_{st} is the stator teeth-mass; β_{slot} is the slot angle; and, h_{sy} is stator yoke height.

Conductor losses are then evaluated using Equation (48), the power equation, for a resistance defined:

$$P_{cu} = q \times I_a^2 \times R_a \quad (48)$$

For rotors operating at high speeds, friction and windage can cause losses, which result in inefficiency and heat production. Friction/windage-losses [35] are given by Equation (49):

$$P_{wind} = C_f \times \pi \times \rho_{air} \times \omega^3 \times r^4 \times L_{st} \quad (49)$$

where, C_f is the friction coefficient and ρ_{air} is the density of air.

The coefficient of friction can then be approximated using Equation (50):

$$C_f \cong 0.0725 \times R_{ey} - 0.2 \quad (50)$$

where, R_{ey} is the Reynold's number.

Initial Machine Sizing

Air gap magnetic shear stress, τ, is the magnetic shear force developed per unit gap area and is constrained by magnetic design and thermal management [36], as shown in Equation (51):

$$\tau \propto K_z B_g \quad (51)$$

where, τ is the shear stress (psi); K_z is the surface current density; and, B_g is the air gap flux density.

Pepi and Mongeau [36] provide a list of typical values of air gap shear stress for different types of motors. The air gap shear stress of 10 psi was assumed for carrying out basic sizing calculations, assuming the generator were air-cooled. The fundamental output machine power formula was utilized to derive the rotor radius and stack length of the machine, as defined by Equation (52):

$$P_{wr} = 2\pi r L_{st} v_{tip} \tau \quad (52)$$

where, r is the rotor radius and L_{st} is the stack length.

The electrical frequency and rotor surface speed were determined by Equation (53):

$$f = pN/60$$
$$\omega = 2\pi f \quad (53)$$
$$\omega = p\omega_m$$

where, ω is the electrical frequency (rad/sec); ω_m is the mechanical frequency (rad/sec); and, N is the speed (rpm).

Machine Detailed Sizing

Once basic sizing was complete, an in-depth analysis was conducted in order to ascertain the overall performance of the machine with a 500 kW power rating. The detailed sizing method was developed using MATLAB. Using this model, all of the desired machine parameters were calculated. The machine sizing parameters such as length, volume, and generator mass were calculated using the basic geometric equations of Equations (54)-(69):

Rotor variables:
h_m = 0.02 [Magnet thickness (m)]
Br = 1.2 [Magnet remnant flux density]
θ_m = 50° [Magnet physical angle (deg)]
Magnet skew angle (actual deg) = 10°

Stator variables:
q = 3 (number of phases)
N_s = 36 (number of slots)
N_{sp} = 1 (number of slots short pitched)
g = 0.002 [air gap (m)]
t_{frac} = 0.5 (peripheral tooth fraction)
h_s = 0.010 [slot depth (m)]
h_d = 0.0004 [slot depression depth (m)]
w_d = 10^{-6} [slot depression width (m)]
s_{yrat} = 0.7 stator back iron ratio (yoke thick/rotor radius)
N_c = 1 (turns per coil)
λ_s = 0.5 (slot fill fraction)
σ_{st} = 6.0×10^7 (stator winding conductivity)
rms = root-mean-square

Densities:
ρ_s = 7700 [steel density (kg/m^3)]
ρ_m = 7400 (Magnet density)
ρ_c = 8900 (conductor density)

Constants:
μ_0 = $4 \times \pi \times 10^{-7}$ (free-space permeability)
ρ_{air} = 1.205 (air density at 20 °C [kg/m^3])
Magnet Mass:

$$M_m = 0.5(p\times\theta_m)\left((r+h_m)^2 - r^2\right)L_{st}\rho_m \tag{54}$$

Tooth width:

$$w_t = 2\pi(R+g+h_m+h_d)\times t_{frac}/N_s \tag{55}$$

Slot top width (at air gap):

$$w_t = 2\pi(R+g+h_m+h_d)\times(1-t_{frac})/N_s \tag{56}$$

Slot bottom width:

$$w_{sb} = w_{st}\times(R+g+h_s+h_d)/(R+g+h_m+h_d) \tag{57}$$

Stator core back iron depth (as p increases, d_c decreases):

$$d_c = s_{yrat}\times R/p \tag{58}$$

Full pitch coil throw:

$$N_{sfp} = N_s/(2p) \tag{59}$$

Actual coil throw:

$$N_{sct} = N_{sfp} - N_{sp} \tag{60}$$

End turn travel (one end):

$$l_{az} = \pi(R-g+h_m+h_d+0.5h_s)\times N_{sct}/N_s \tag{61}$$

End length (half coil):

$$l_{e_2} = \pi\times l_{az} \tag{62}$$

End length (axial direction):

$$l_{e_1} = l_{e_2}/\pi \tag{63}$$

Overall machine length:

$$L_{mach} = L_{st} + 2l_{e_1} \tag{64}$$

Core inside radius:

$$R_{ci} = R + h_m + g + h_d + h_s \tag{65}$$

Core outside radius:

$$R_{co} = R_{ci} + d_c \tag{66}$$

Overall diameter:

$$D_{mach} = 2R_{co} \tag{67}$$

Tooth flux density:

$$B_t = B_g/t_{frac} \tag{68}$$

Back iron flux density:

$$B_b = B_g\times R/(p\times d_c) \tag{69}$$

Equations (54)-(69) were mainly extracted from the work by Hanselmann [25] and Hendershot and Miller [31].

Particle Swarm Optimization

The particle swarm optimization (PSO) algorithm was used in this current study and formulated to optimize efficiency as an objective function with bounded parameter constraints. Particle swarm is a population-based algorithm based on flocks of birds or insects swarming. The optimizing variables were rotor-length-to-diameter ratio, rotor radius, and stack length. Simulations were performed using PSO toolbox in Matlab. The PSO algorithm is well-suited for solving optimization problems that are too complicated to be solved using conventional optimization methods, such as problems in which the objective function is discontinuous, stochastic, or highly nonlinear.

HSPM Generator Optimum Efficiency Using PSO Sizing

The particle swarm optimization (PSO) algorithm has been used to optimize generator efficiency [37-39]. The optimization variables x_1, x_2, and x_3 are L/D ratio, rotor radius, and rotor stack length, respectively. The efficiency function was implemented in the form of an m-file. The PSO algorithm was then used to maximize the efficiency function and obtain the required variables using [1 0 0] constraints as the lower limit, and [3 1 1] as the upper limit. All of the detailed variables were evaluated for a high-speed permanent-magnet synchronous generator [25, 31] using Equations (70)-(80):

$$M_{Total} = M_{Core} + M_{Magnet} + M_{Shaft} + M_{Conductor} + M_{Service} \quad (70)$$

$$M_{Core} = M_{cb} + M_{ct} \quad (71)$$

$$M_{cb} = \rho_s \pi \left(R_{co}^2 - R_{ci}^2\right) L_{st} \quad (72)$$

where, M_{cb} is the back iron mass (kg); ρ_s is the steel density (kg/m^3); R_{co} is the core outside radius; and, R_{ci} is the core inside radius;

$$R_{ci} = R + h_m + g + h_d + h_s \quad (73)$$

where, h_m is the magnet thickness (m); g is the air gap (m); h_d is the slot depression depth (m); and, h_s is the slot depth (m);

$$R_{co} = R_{ci} + d_c \quad (74)$$

where, d_c is the stator core back iron depth (m);

$$M_{ct} = L_{st}\rho_s\left(N_s w_t h_s + 2\pi R h_d - N_s h_d w_d\right) \quad (75)$$

where, M_{ct} is the teeth mass; N_s is the number of slots; w_t is the tooth width; and, w_d is the slot depression width (m);

$$M_{Magnet} = 0.5\left(p\theta_m\left(\left(r + h_m\right)^2 - r^2\right)L_{st}\rho_m\right) \quad (76)$$

where, θ_m is the magnet physical angle; ρ_m is the magnet density; and, p is the pole pairs number;

$$M_{Shaft} = \pi R^2 L_{st}\rho_s \quad (77)$$

$$M_{Conductor} = 3L_{ac}A_{ac}\rho_c \quad (78)$$

where, L_{ac} is the armature conductor length; A_{ac} is the armature conductor area (assumes form wound); and, ρ_c is the conductor density;

$$L_{ac} = 2N_a\left(L_{st} + 2le_2\right) \quad (79)$$

$$A_{ac} = A_s\lambda_s / \left(2N_c\right) \quad (80)$$

where, N_a is the number of armature turns; le_2 is the end length (half coil); A_s is the slot area; λ_s is the slot fill fraction; and, N_c is the turns per coil.

To account for the additional services associated with machine cooling, a 15% service mass fraction was added to the total mass [36], as defined by Equations (81)-(84):

$$M_{Service} = 0.15\left(M_{Conductor} + M_{Shaft} + M_{Magnet} + M_{Core}\right) \quad (81)$$

$$P_{Total\_Losses} = P_{Core} + P_{Conductor} + P_{Wind} \quad (82)$$

$$P_{input} = P_{Total\_Losses} + P_{out} \quad (83)$$

$$\eta = P_{out} / P_{input} \quad (84)$$

Based on the application, the same techniques could be used to optimize (minimize) the different loss types, mass part of the machine, or any geometric sizing parameter.

Design Comparisons

In order to make a comparison between the classical and the optimum design methods, both design methods were compared using a tip speed of 250 m/s and an output power of 500 kW. Figures 10-12 show the waveforms of flux density, EMF, and harmonic content, respectively, for the classical design. Figures 13-15 show the same for the optimum

design. Tables 1 and 2 show the complete detailed generator parameters for the original and optimized designs, respectively.

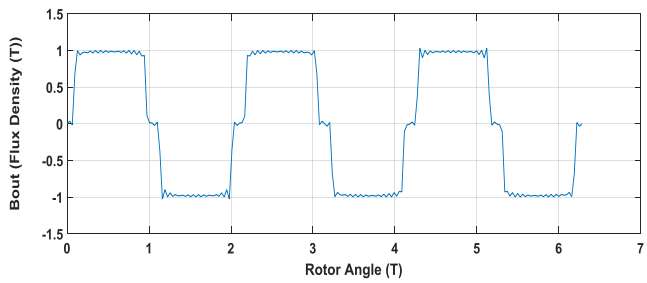

Figure 10. Initial Flux Density Waveform for the Original Design

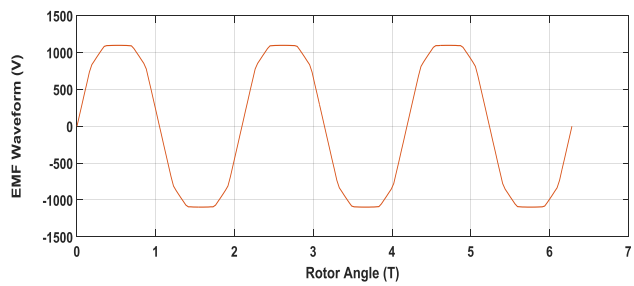

Figure 11. Initial EMF Waveform for the Original Design

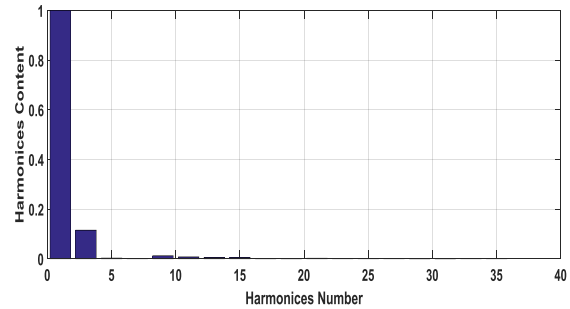

Figure 12. Initial Harmonic Content (12.2077 %) for the Original Design

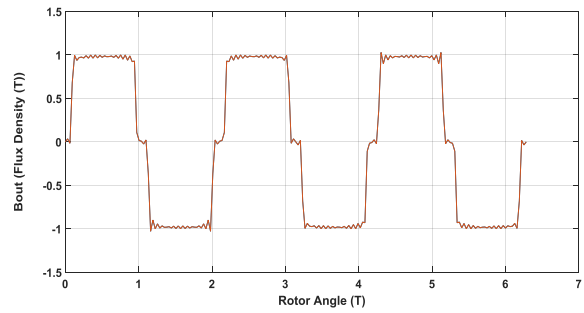

Figure 13. Initial Flux Density Waveform

Table 1. Complete Classical Design Parameters

Machine Size					
D_{mach} = 0.1397 m	D = 0.0608 m	w_s = 0.0042 m	d_c = 0.0071 m	w_{st} = 0.0046 m	w_t = 0.0046 m
L_{mach} = 0.2023 m	L_{st} = 0.1519 m	l_{az} = 0.0252 m	le_1 = 0.0252 m	le_2 = 0.0792 m	w_{sb} = 0.0037 m
L_{ac} = 7.4476 m	A_{ac} = 1.0424e-5 m^2		A_s = 4.1697e-5 m^2	R_{co} = 0.0699 m	R_{ci} = 0.0628 m
Machine Ratings					
Speed = 78,579 rpm	V_a = 1,225.8 V		E_a = 1,284.4 V	P_{in} = 507.42 kW	I_a = 135.9692 A
R_a = 0.0119 Ω	$P_{air\ Gap}$ = 660.4237 Watt		X_s = 0.4216 Ω	eff = 0.97	pf = 0.964
Stator Parameters					
L_s = 1.7077e-2 mH	L_{slot} = 5.0754e-3 mH		B_b = 1.2262 mH	B_t = 1.7166 mH	λ = 0.0736 T
Rotor Parameters					
k_g = 1.1871	g_e = 0.0023 m	B_g = 0.8583 T	L_{ag} = 1.209e-2 mH	τ_s = 0.0088	
Machine Losses					
P_c = 4,289.6 Watt	P_{wind} = 2,465.5 Watt		Total Rotor Losses = 2,544 Watt	P_{cb} = 1,951.4 Watt	
P_{ct} = 2,338.2 Watt		THD = 12.2077 %		$P_{tlosses}$ = 7,415.5 Watt	
Time Harmonic Losses = 239.9 Watt			Space Harmonic Losses = 14.6 Watt		
Machine Weights					
M_{cb} = 3.4555 kg	M_{ct} = 2.0288 kg	M_{core} = 5.4843 kg	M_m = 2.3768 kg	$M_{service}$ = 1.9989 kg	
M_{shaft} = 3.3918 kg		$M_{conductor}$ = 2.0729 kg		M_{tot} = 15.3247 kg	

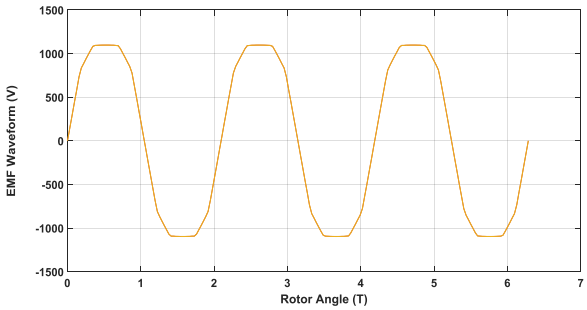

Figure 14. Initial EMF Waveform

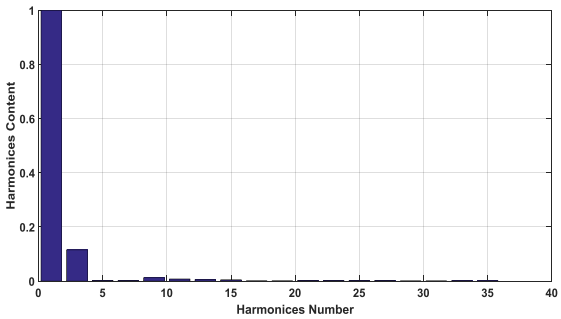

Figure 15. Initial Harmonic Content (11.6276 %)

From these waveform comparisons, it can be seen that THD was improved as a result of reduced losses and enhanced machine performance.

Original Design Results

Efficiency-Optimized Design Results

Optimizing variables: $x_1 = 1.3943$; $x_2 = 0.0407$; $x_3 = 0.1134$.

Effect of Number of Poles on Sizing Parameters and M/C Characteristics

Consider the case of 50 kW of output power with different tip speeds of 250, 200, 150, and 100 m/s for different numbers of poles (4, 6, and 12). The results confirmed that the number of poles affects the electrical, magnetic, and structural performance, which have an impact on machine frequency, voltage waveforms, magnetic flux, magnetic volume, air gap, and the stator-back iron thickness. Figures 16-18 depict these various effects at 50 kW.

Figures 16-18 show that 1) rpm speed was constant at each tip speed because the frequency changed with changing pole numbers; 2) frequency was directly proportional to the number of poles at each tip speed; and, 3) magnet mass increased with the number of poles for a specific tip speed and total losses.

Table 2. Complete Optimized Design Parameters

Machine Size					
D_{mach} = 0.1651 m	D = 0. 0814 m	w_s = 0.0051 m	d_c = 0.0095 m	w_{st} = 0.0055 m	w_t = 0.0055 m
L_{mach} = 0.1729 m	L_{st} = 0.1134 m	l_{az} = 0.0297 m	le_1 = 0.0297 m	le_2 = 0.0933 m	w_{sb} = 0.0046 m
L_{ac} = 7.2023 m	A_{ac} = 1.2671e-5 m^2		A_s = 5.0686e-5 m^2	R_{co} = 0.0826 m	R_{ci} = 0.0731 m
Machine Ratings					
Speed = 58,683 rpm	V_a = 756.8998 V		E_a = 815.273 V	P_{in} = 506.52 kW	I_a = 220.1965 A
R_a = 0.0095 Ω	$P_{air\ Gap}$ = 1,378 Watt		X_s = 0.2562 Ω	eff = 0.992	pf = 0.99
Stator Parameters					
L_s =1.3898e-2 mH	L_{slot} = 3.1234e-3 mH	B_b = 1.2232 mH	B_t = 1.7124 mH	λ = 0.0625 T	
Rotor Parameters					
k_g = 1.1319	g_e = 0.0024 m	B_g = 0.8562 T	L_{ag} = 1.0805e-2 mH	τ_s = 0.0106	
Machine Losses					
P_c = 2,672.9 Watt	P_{wind} = 2,465.5 Watt		Total Rotor Losses = 177.6 Watt	P_{cb} = 1,394.9 Watt	
P_{ct} = 1,278 Watt		THD = 11.6276%		$P_{tlosses}$ = 6,516.3 Watt	
Time Harmonic Losses = 167.5 Watt			Space Harmonic Losses = 10.2 Watt		
Machine Weights					
M_{cb} = 4.0548 kg	M_{ct} = 1.8204 kg	M_{core} = 5.8752 kg	M_m = 2.2277 kg	$M_{service}$ = 2.2622 kg	
M_{shaft} = 4.5417 kg		$M_{conductor}$ = 2.4367 kg		M_{tot} = 17.3436 kg	

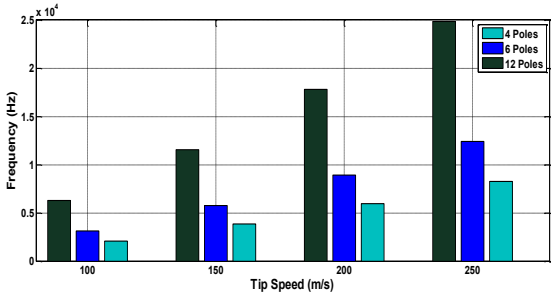

Figure 16. Frequency versus Tip Speed for Various Number of Poles

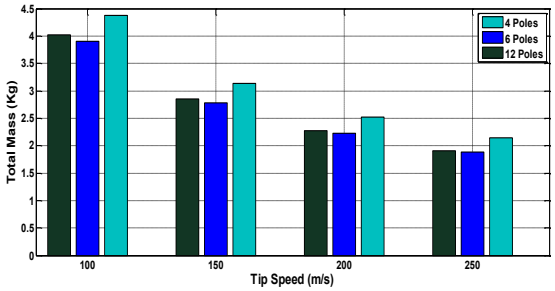

Figure 17. Total Mass versus Tip Speed for Various Number of Poles

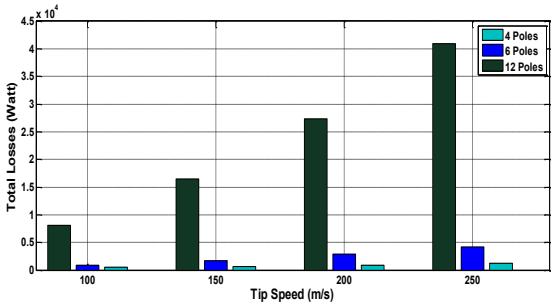

Figure 18. Total Losses versus Tip Speed for Various Number of Poles

Conclusion

In this paper, the authors presented an improved design and performance analysis for a high-speed PM generator, as compared to a traditional design. As a result, significant reductions in both weight and volume were achieved for a case study involving a 500 kW, 250 m/s machine based on previous work. The optimizing variables considered in this study were rotor-length-to-diameter ratio, rotor radius, and stack length, with the objective of maximizing efficiency. It was determined that using the proposed PSO algorithm in HSPMSG sizing resulted in reduced losses and significant improvement in the performance of the machine parameters. Furthermore, it was found that if the rotational speed was held constant as the number of poles increased, the weight of the machine could be decreased and the electrical frequency increased. These design factors can also have an impact on the number of slots/poles/phase affecting THD and the output waveforms of the HSPM generator that could provide further improvement in smart grid applications.

References

[1] Keyhani, A., Marwali, M. N., & Dai, M. (2010). *Integration of Green and Renewable Energy in Electric Power Systems*. Wiley.

[2] Keyhani, A. (2009). Cyber-Controlled Smart Microgrid Systems of the Future: The High Penetration of Renewable and Green Energy Sources. *New Research Directions for Future Cyber-Physical Energy Systems Proceedings*, Baltimore, Maryland.

[3] El Shahat, A., & Keyhani, A. (2012). Sizing High Speed Micro Generators for Smart Grid Systems. *Smart power Grids 2011, Series: Power Systems*. Springer-Verlag Berlin Heidelberg.

[4] El Shahat, A. (2012). PM Synchronous Machine New Aspects; Modeling, control, and design. *LAP Lambert Academic Publishing.*

[5] Ahmad, R. A., Pan, Z., & Saban, D. M. (2007). On-Board Electrical Network Topology Using High Speed Permanent Magnet Generators. *IEEE Electric Ship Technologies Symposium*, *7*, 356–362.

[6] Scridon, S., Boldea, I., Tutelea, Blaabjerg, L., F., & Ritchie, E. (2004). BEGA–A Biaxial Excitation Generator for Automobiles: Comprehensive Characterization and Test Results. *39th IEEE IAS Annual Meeting Conference*, *3*, 1682–1690.

[7] Binder, A., Schneider, T., & Klohr, M. (2006). Fixation of Buried and Surface- Mounted Magnets in High-Speed Permanent-Magnet Synchronous Machines. *IEEE Trans. on Industry Applications*, *42*, 1031–1037.

[8] Hosseini, S. M., Mirsalim, M. A., & Mirzaei, M. (2008). Design, Prototyping, and Analysis of a Low Cost Axial-Flux Coreless Permanent-Magnet Generator. *IEEE Trans. on Magnet.*, *44*, 75–80.

[9] Mellor, P. H., Burrow, S. G., Sawata, T., & Holme, M. (2005). A Wide–Speed–Range Hybrid Variable–Reluctance / Permanent–Magnet Generator for Future Embedded Aircraft Generation Systems. *IEEE Trans. on Industry Applications*, *41*, 551–556.

[10] Sadeghierad, M., Lesani, H., Monsef, H., & Darabi, A. (2007). Design considerations of High Speed Axial Flux permanent magnet Generator with Coreless Stator. *The 8th International Power Engineering Conference (IPEC)*, 1098–1102.

[11] Arnold, D. P., Das, S., Park, J. W., Zana, I., Lang, J. H., & Allen, M. G. (2006). Micro fabricated High-

Speed Axial-Flux Multi watt Permanent- Magnet Generators—Part II: Design, Fabrication, and Testing. *Journal of Micro Electromechanical Systems*, *5*, 1351–1363.

[12] Binder, A., Schneider, T., & Klohr, M. (2006). Fixation of Buried and Surface-Mounted Magnets in High -Speed Permanent - Magnet Synchronous Machines. *IEEE Trans. on Industry Applications*, *42*, 1031–1037.

[13] Paulides, J. J. H., Jewell, G., Howe, W. (2004). An Evaluation of Alternative Stator Lamination Materials for a High – Speed, 1.5 MW, Permanent Magnet Generator. *IEEE Trans. on Magnetics*, *40*, 2041-2043.

[14] El–Hasan, T. S., Luk, P. C. K., Bhinder, F. S., & Ebaid, M. S. (2000). Modular Design of High–Speed Permanent–Magnet Axial–Flux Generators. *IEEE Trans. on Magnetics*, *36*, 3558–3561

[15] Jang, S. M., Cho, H. W., & Jeong, Y. H. (2006). Influence on the rectifiers of rotor losses in high–speed permanent magnet synchronous alternator. *Journal of Applied Physics*, American Institute of Physics, 08R315-3.

[16] Hwang, C. C., Tien, C. L., & Chang, H. C. (2007). Performance and applications of a small PM generator. *phys. stat. sol., 4*, 4635–4638.

[17] Kolondzovski, Z. (2008). Determination of critical thermal operations for High–speed permanent magnet electrical machines. *The International Journal for Computation and Mathematics in Electrical and Electronic Engineering*, *27*, 720-727.

[18] Sahin, F., & Vandenput, A. J. A. (2003). Thermal modeling and testing of a High–speed axial–flux permanent–magnet machine. *The International Journal for Computation and Mathematics in Electrical and Electronic Eng.*, *22*, 982–997.

[19] Vandenput, A. J. A., & Sahin, F. (2008). Design considerations of the flywheel-mounted axial-flux permanent-magnet machine for a hybrid electric vehicle. *8th European Conference on Power Electronics and Applications*.

[20] Nagorny, A. S., Dravid, N. V., Dravid, R. H., & Kenny, B. H. (2005). Design Aspects of a High Speed Permanent Magnet Synchronous Motor/Generator for Flywheel Applications. *International Electric Machines and Drives Conference*, San Antonio, Texas.

[21] Caricchi, F., Crescimbini, F., Mezzetti, F., & Santini, E., (1996). Multistage axial flux PM machine for wheel direct drive. *IEEE Trans. on Industry Applications*, *32*, 882-887.

[22] Binns K. J., & Shimmin, D. W. (1996). Relationship between rated torque and size of permanent magnet machines. *IEE Proc. Electr. Power Appl.*, *143*, 417-422.

[23] Fengxiang, W., Wenpeng, Z., Ming, Z., & Baoguo, W. (2002). Design considerations of high speed PM generators for micro turbines. *IEEE trans. energy conversion*.

[24] Pavlik, D., Garg, V., Repp, J., & Weiss, J. (1988). A finite element technique for calculating the magnet sizes and inductances of permanent magnet machines. *IEEE trans. of energy conversion*, *3*.

[25] Hanselmann, D. C. (1994). *Brushless Permanent Magnet Motor Design*. New York: McGraw-Hill.

[26] Kang, D., Curiac, P., Jung, Y., & Jung, S. (2003). Prospects for magnetization of large PM rotors: conclusions from a development case study. *IEEE trans. on Energy Conversion*, *18*(3).

[27] Website for Magnetic Component Engineering. Inc., 2004.

[28] Polinder, H., & Hoeijmakers, M. J. (1999). Eddy – Current Losses in the Segmented Surface Mounted Magnets of a PM Machine. *IEE Proceedings, Electrical Power Applications*, *146*(3).

[29] Rippy, M. (2004). An overview guide for the selection of lamination materials. Porto Laminations, Inc.

[30] Bianchi, N., & Lorenzoni, A. (1996). Permanent magnet generators for wind power industry: an overall comparison with traditional generators. *Opportunities and advances in international power generation conference*, 419.

[31] Hendershot J. R., & Miller, T. J. E. (1994). *Design of Brushless Permanent Magnet Motors*. Oxford, U.K.: Magna Physics Publishing and Clarendon Press.

[32] Rahman, M. A., & Slemon, G. R. (1985). Promising Applications of Neodymium Iron Boron Iron Magnets in Electrical Machines. *IEEE Trans. On Magnetics*, *5*.

[33] Hanselmann, D. C. (1994). *Brushless Permanent Magnet Motor Design*. New York: McGraw-Hill.

[34] Hendershot J. R., & Miller, T. J. E. (1994). *Design of Brushless Permanent Magnet Motors*. Oxford, U.K.: Magna Physics Publishing and Clarendon Press.

[35] Rucker, J. E., Kirtley, J. L., & McCoy, Jr. T. J. (2005). Design and Analysis of a Permanent Magnet Generator for Naval Applications. *IEEE Electric Ship Technologies Symposium*, 451–458.

[36] Pepi, J., & Mongeau, P. (2004). High power density permanent magnet generators. DRS Electric power technologies, Inc.

[37] Kennedy, J., & Eberhart, R. (1995). Particle swarm optimization. Proc. *IEEE International Conf. on Neural Networks*, Perth, Australia.

[38] Clerc, M. (2004). *Discrete Particle Swarm Optimization*. New Optimization Techniques in Engineering Springer-Verlag.

[39] Yasuda, K., Ide, A., & Iwasaki, N. (2003). Adaptive particle swarm optimization. *Proceedings of IEEE International Conference on Systems, Man and Cybernetics*, 1554-1559.

Biographies

ADEL EL SHAHAT is an assistant professor of Electrical Engineering in the Department of Electrical Engineering at Georgia Southern University. He received his BSc degree and MSc degree (Power and Machines) in Electrical Engineering from Zagazig University, Egypt, in 1999 and 2004, respectively. He received his PhD (Joint Supervision) from Zagazig University, Egypt, and The Ohio State University in 2011. His research focuses on various aspects of power systems, smart grid systems, power electronics, electric machines, renewable energy systems, energy storage, and engineering education. Dr. El Shahat may be reached at aahmed@georgiasouthern.edu

RAMI J. HADDAD is an assistant professor in the Department of Electrical Engineering at Georgia Southern University. He received his BS degree in Electronics and Telecommunication Engineering from the Applied Sciences University, Jordan; his MS degree in Electrical and Computer Engineering from the University of Minnesota; and his PhD from the University of Akron. He is an IEEE senior member. His research focuses on various aspects of optical fiber communication/networks, broadband networks, multimedia communications, multimedia bandwidth forecasting, and engineering education. Dr. Haddad may be reached at rhaddad@georgiasouthern.edu

YOUAKIM KALAANI is an associate professor and Chair of the Electrical Engineering Department at Georgia Southern University. Dr. Kalaani received his BS degree in Electrical Engineering from Cleveland State University. He graduated from CSU with masters and doctoral degrees in Electrical Engineering with a concentration in power systems. Dr. Kalaani is a licensed professional engineer (PE) and served as ABET Program Evaluator. He is a senior member of IEEE and has research interests in distributed power generation, optimization, and engineering education. Dr. Kalaani may be reached at yalkalaani@georgiasouthern.edu

A SIMPLE BLOCK CODING SCHEME FOR PEAK-TO-AVERAGE POWER RATIO REDUCTION IN MULTI-CARRIER SYSTEMS

Yoonill Lee, Purdue University Northwest

Abstract

Orthogonal frequency-division multiplexing (OFDM) is an attractive modulation technique for mitigating effects of delay spread in a multipath channel. However, the main disadvantage of OFDM is that it has a large peak-to-average power ratio (PAPR). One technique for PAPR reduction is Scheme I, introduced by Jones et al. [1], which is a block coding scheme using an odd parity check bit and mapping a 3-bit data word onto a 4-bit code word. One disadvantage of Scheme I is that it can only reduce PAPR when the length of the code word is an integer multiple of four. Another technique is Scheme II, introduced by Fragiacomo et al. [2], for longer code words. In Scheme II, where M and N are defined as the length of a code word and the length of a data word, respectively, one additional bit representative of the complement of the (N-1)th bit of the data word is upended as the (N+1)th bit of the data word such that M becomes N+1. Effectively, PAPR can be reduced even though M is not an integer multiple of four, allowing for a less-limiting selection of M. However, gains in PAPR reduction are marginal as M increases. In this paper, the author proposes a new approach called Scheme III to obtain more PAPR reduction, by adding two additional bits to Scheme I. Accordingly, M becomes N+2 rather than N+1, as in Scheme II. Scheme III is suited for large numbers of sub-carriers at the expense of two additional bits.

Introduction

A multi-carrier transmission scheme such as orthogonal frequency-division multiplexing (OFDM) has been proposed for many wireless applications because it is an attractive modulation technique for mitigating effects of delay spread in a multi-path channel. However, the main disadvantage of OFDM is that it has a large peak-to-average power ratio (PAPR), which can result in significant distortion when OFDM signals are passed through a nonlinear device such as a transmitter power amplifier. OFDM can be combined with multiple-input multiple-output (MIMO) technology (e.g., multiple antennas at the transmitter and receiver) to increase the diversity gain to enhance the capacity of the system. Such a MIMO-OFDM system is a key technology for next generation mobile communications as well as wireless local area network (WLAN) [3-5]. The large PAPR problem in OFDM carries over to a MIMO-OFDM system because it is based on OFDM.

A number of approaches have been proposed to reduce PAPR for multi-carrier transmission. In general, the PAPR reduction techniques can be classified into the following categories: clipping and filtering, coding, selective mapping, partial transmit sequence, nonlinear companding transforms, tone reservation, tone injection, and scrambling [6-11]. In this study, however, the focus was on the coding technique category.

Block Coding Scheme with an Odd Parity Check Bit (Scheme I)

The complex envelope of the transmitted OFDM signal can be written as shown in Equation (1):

$$s(t) = \sum_{n=-\infty}^{\infty} \sum_{m=0}^{M-1} d_{n,m} e^{j2\pi f_m t} g(t-nT) \tag{1}$$

where, $d_{n,m}$ is the data symbol for the m-th sub-carrier of the n-th OFDM symbol; M is the number of sub-carriers (or length of the code word); f_m is the m-th sub-carrier; T is an OFDM symbol duration; and, $g(t)$ is a rectangular pulse shape of duration T.

With no loss in generality, index n can be omitted for simplicity. Then Equation (1) can be simply expressed as Equation (2):

$$s(t) = \sum_{m=0}^{M-1} d_m e^{j2\pi f_m t} \tag{2}$$

Let $p(t)$ be the envelope power of the OFDM signal. Since $s(t)$ is a complex number, $p(t)$ is $s(t)s^*(t)$, where * denotes a conjugate of a complex number. If the power in each sub-carrier is normalized to 1 watt, then the average power is M watts. The PAPR Γ (in dB) is defined in Equation (3). First, the uncoded data words will be discussed. Subsequently, how the block coding scheme using an odd parity check bit works for four sub-carriers (M = 4) will be explained. Table 1 shows the peak envelope powers for all

possible uncoded data words. Let us define PEP as the peak envelope power of *p(t)*. The first PEP was 16.00 watts when the data words were 0000, 0101, 1010, and 1111. The second PEP was 9.44 watts when the data words were 0011, 0110, 1001, and 1100. All other PEPs were the same values of 7.07 watts. Thus, if data words that generate large PEPs such as 16.00 watts and 9.44 watts can be removed, the PAPR can be reduced. This is the main motivation behind block coding.

$$\begin{aligned}\Gamma &= 10\log_{10}\left\{\frac{peak\ envelope\ power}{average\ power}\right\} \\ &= 10\log_{10}\left\{\frac{peak\ p(t)}{M}\right\}\end{aligned} \tag{3}$$

Table 1. PEP for All Possible Uncoded Data Words (N = 4)

Data Words	d_1	d_2	d_3	d_4	PEP (watt)
0	0	0	0	0	16.00
1	0	0	0	1	7.07
2	0	0	1	0	7.07
3	0	0	1	1	9.44
4	0	1	0	0	7.07
5	0	1	0	1	16.00
6	0	1	1	0	9.44
7	0	1	1	1	7.07
8	1	0	0	0	7.07
9	1	0	0	1	9.44
10	1	0	1	0	16.00
11	1	0	1	1	7.07
12	1	1	0	0	9.44
13	1	1	0	1	7.07
14	1	1	1	0	7.07
15	1	1	1	1	16.00

The block coding scheme using an odd parity check bit was introduced by Jones et al. [1]. The basic idea is that a 3-bit data word is mapped onto a 4-bit code word using an odd parity check bit. The first three bits c_1, c_2, and c_3 in the code word are the same as d_1, d_2, and d_3 in the data word. However, the fourth bit, c_4, in the code word is an odd parity check bit. For example, if a 3-bit data word is $d_1 = 0$, $d_2 = 1$, and $d_3 = 0$, then the 4-bit code word using an odd parity check bit is $c_1 = 0$, $c_2 = 1$, $c_3 = 0$, and $c_4 = 0$. The peak envelope powers for all possible code words using an odd parity check bit are shown in Table 2. Table 2 shows that the peak envelope powers have the same value, 7.07 watts, because the first and second PEPs are removed.

Table 2. PEP for All Possible Code Words Using Scheme I (M = 4)

Code Words	c_1	c_2	c_3	c_4	PEP (watt)
0	0	0	0	1	7.07
1	0	0	0	1	7.07
2	0	0	1	0	7.07
3	0	0	1	0	7.07
4	0	1	0	0	7.07
5	0	1	0	0	7.07
6	0	1	1	1	7.07
7	0	1	1	1	7.07
8	1	0	0	0	7.07
9	1	0	0	0	7.07
10	1	0	1	1	7.07
11	1	0	1	1	7.07
12	1	1	0	1	7.07
13	1	1	0	1	7.07
14	1	1	1	0	7.07
15	1	1	1	0	7.07

Table 3 show the results of PAPR with different lengths of the code word for uncoded data words and Scheme I for comparison. Table 3 further shows that Scheme I works well when the length of the code word was an integer multiple of four. The PAPR value was 2.48 dB in the case of M = 4. Thus, the amount of PAPR reduction (ΔdB_I) relative to the uncoded data words was as much as 3.54 dB. However, it has the same PAPR as the uncoded data words if the length of the code word is not an integer multiple of four. This is the main drawback of Scheme I. Block coding Scheme II, explained in the next section, addresses how to solve this problem.

Block Coding Scheme with One Additional Bit (Scheme II)

As shown in the previous section, the disadvantage of block coding using an odd parity check (Scheme I) is that it

can only reduce PAPR when the length of the code word is an integer multiple of four. To be specific, it has the smallest PAPR value with M = 4. When the length of the code word is not an integer multiple of four, it does not eliminate the code word that generate large powers.

Table 3. PAPR (in dB) Comparisons for Uncoded Data Words and Scheme I

Length of Code Words (M)	Uncoded	Scheme I	DdB_I
4	6.02	2.48	3.54
5	6.99	6.99	0
6	7.78	7.78	0
7	8.45	8.45	0
8	9.03	6.53	2.50
9	9.54	9.54	0
10	10.00	10.00	0
11	10.41	10.41	0
12	10.79	9.21	1.58
13	11.14	11.14	0
14	11.46	11.46	0
15	11.76	11.76	0
16	12.04	10.88	1.16

Another approach was introduced by Fragiacomo et al. [2] for longer code words. Let M and N be defined as the length of a code word and the length of a data word, respectively. Instead of using an odd parity check bit, one additional bit, representative of the complement of the (N-1)th bit of the data word, is upended as the (N+1)th bit of the data word such that M becomes N+1. Table 4 show the PEP for all possible code words using one additional bit with M = 5. The first PEP was 13.33 watts and the second PEP was 13.00 watts.

Table 5 shows the PAPR for different lengths of code words for uncoded data words using Scheme II for comparison. The PAPR values were reduced even though the length of the code word was not an integer multiple of four. Thus, Scheme II has a more general way to select the length of the code word compared to Scheme I. However, the amount of PAPR reduction (ΔdB_{II}) does not improve much when the length of the code word increases. To obtain better PAPR reduction for large code words, a new approach is proposed by adding two additional bits to Scheme I.

Table 4. PEP for All Possible Code Words Using Scheme II (M = 5)

Code Words	c_1	c_2	c_3	c_4	c_5	PEP (watt)
0	0	0	0	0	1	10.51
1	0	0	0	1	1	13.33
2	0	0	1	0	0	10.48
3	0	0	1	1	0	13.00
4	0	1	0	0	1	13.33
5	0	1	0	1	1	10.51
6	0	1	1	0	0	13.00
7	0	1	1	1	0	10.48
8	1	0	0	0	1	10.48
9	1	0	0	1	1	13.00
10	1	0	1	0	0	10.51
11	1	0	1	1	0	13.33
12	1	1	0	0	1	13.00
13	1	1	0	1	1	10.48
14	1	1	1	0	0	13.33
15	1	1	1	1	0	10.51

Table 5. PAPR (in dB) Comparisons for Uncoded Data Words and Scheme II

Length of Code Words (M)	Uncoded	Scheme II	DdB_{II}
4	6.02	3.73	2.29
5	6.99	4.26	2.73
6	7.78	5.09	2.69
7	8.45	5.58	2.87
8	9.03	6.53	2.50
9	9.54	7.36	2.18
10	10.00	8.06	1.94
11	10.41	8.67	1.74
12	10.79	9.21	1.58
13	11.14	9.69	1.45
14	11.46	10.12	1.34
15	11.76	10.52	1.24
16	12.04	10.88	1.16

Proposed Coding Scheme Adding Two Additional Bits to Scheme I (Scheme III)

The proposed block coding algorithm is as follows:

Step 1: Apply Scheme I to the data words.
Step 2: Upend the complement of the (N-1)th bit of the code word as the (N+1)th bit of the code word.
Step 3: Upend the complement of the odd parity check bit as the (N+2)th bit of the code word.

Accordingly, M becomes N+2 rather than N+1, as in Scheme II. Table 6 shows the peak envelope power with M = 6 for the proposed Scheme III. The first PEP was 16.98 watts and the second PEP was 13.29 watts. Although these values are larger than those in Scheme I and II, the PAPR values are smaller compared to the two previous schemes. Moreover, the amount of PAPR reduction (ΔdB_{III}) is much larger than the two previous schemes, when the length of the code word increases. Thus, Scheme III is suited for large numbers of sub-carriers at the expense of two additional bits. Table 7 shows a comparison for all schemes with different lengths of code words.

Table 6. PEP for All Possible Code Words Using Scheme III (M = 6)

Code Words	c_1	c_2	c_3	c_4	c_5	c_6	PEP (watt)
0	0	0	0	1	1	0	13.29
1	0	0	0	1	1	0	13.29
2	0	0	1	0	0	1	16.98
3	0	0	1	0	0	1	16.98
4	0	1	0	0	1	1	13.29
5	0	1	0	0	1	1	13.29
6	0	1	1	1	0	0	16.98
7	0	1	1	1	0	0	16.98
8	1	0	0	0	1	1	16.98
9	1	0	0	0	1	1	16.98
10	1	0	1	1	0	0	13.29
11	1	0	1	1	0	0	13.29
12	1	1	0	1	1	0	16.98
13	1	1	0	1	1	0	16.98
14	1	1	1	0	0	1	13.29
15	1	1	1	0	0	1	13.29

Simulation Results

Figures 1 and 2 show the envelope powers for uncoded data words and under Scheme I, respectively. Figures 3 and 4 show the PAPR values for uncoded data words and under Scheme II, respectively. Similarly, Figures 5 and 6 show the PAPR values for uncoded data words and under Scheme III, respectively. Finally, Figures 7 and 8 show the PAPR comparison and reduction for all of the schemes, respectively. As can be seen, the proposed Scheme III shows improved performance compared to those of the two previous schemes, when the length of the code word increases.

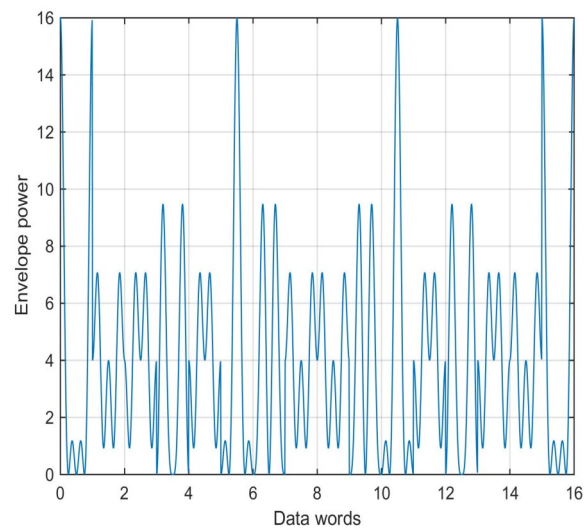

Figure 1. Envelope Power for Uncoded Data Words (N = 4)

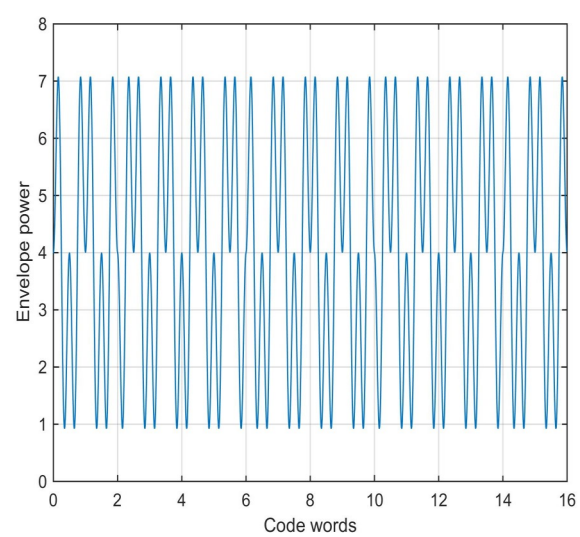

Figure 2. Envelope Power Using Scheme I (M = 4)

Table 7. PAPR (in dB) Comparisons for All Schemes

Length of Code Words (M)	Uncoded	Scheme I	DdB_I	Scheme II	DdB_{II}	Scheme III	DdB_{III}
4	6.02	2.48	3.54	3.73	2.29	3.73	2.29
5	6.99	6.99	0	4.26	2.73	4.26	2.73
6	7.78	7.78	0	5.09	2.69	4.52	3.26
7	8.45	8.45	0	5.58	2.87	5.58	2.87
8	9.03	6.53	2.50	6.53	2.50	6.02	3.01
9	9.54	9.54	0	7.36	2.18	6.59	2.95
10	10.00	10.00	0	8.06	1.94	6.64	3.36
11	10.41	10.41	0	8.67	1.74	7.44	2.97
12	10.79	9.21	1.58	9.21	1.58	7.78	3.01
13	11.14	11.14	0	9.69	1.45	8.15	2.99
14	11.46	11.46	0	10.12	1.34	8.54	2.92
15	11.76	11.76	0	10.52	1.24	9.07	2.69
16	12.04	10.88	1.16	10.88	1.16	9.54	2.50

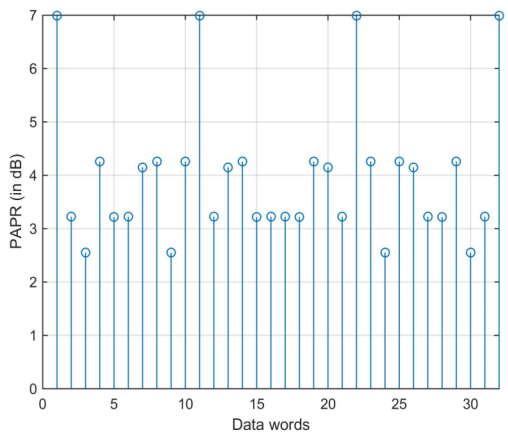

Figure 3. PAPR (in dB) for Uncoded Data Words (N = 5)

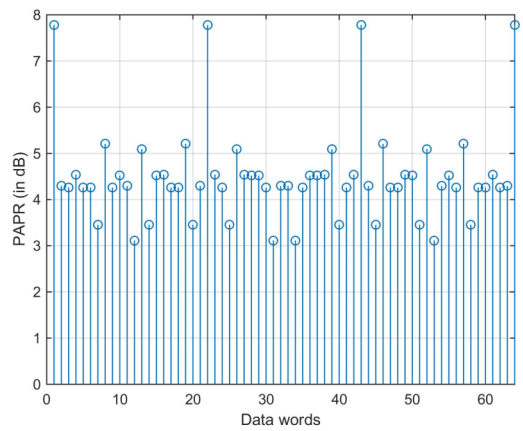

Figure 5. PAPR (in dB) for Uncoded Data Words (N = 6)

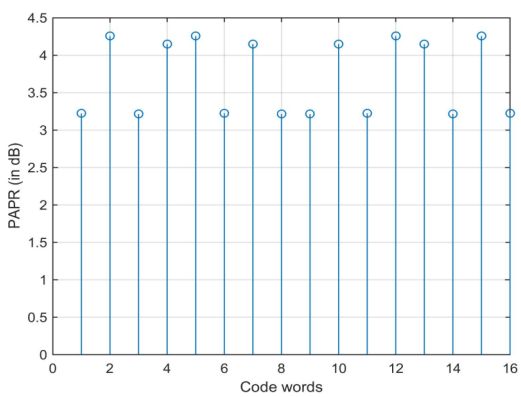

Figure 4. PAPR (in dB) Using Scheme II (M = 5)

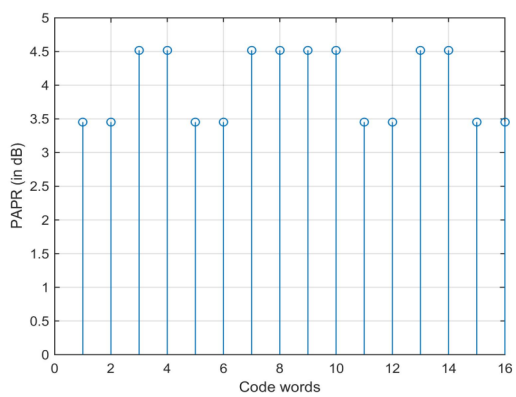

Figure 6. PAPR (in dB) Using Scheme III (M = 6)

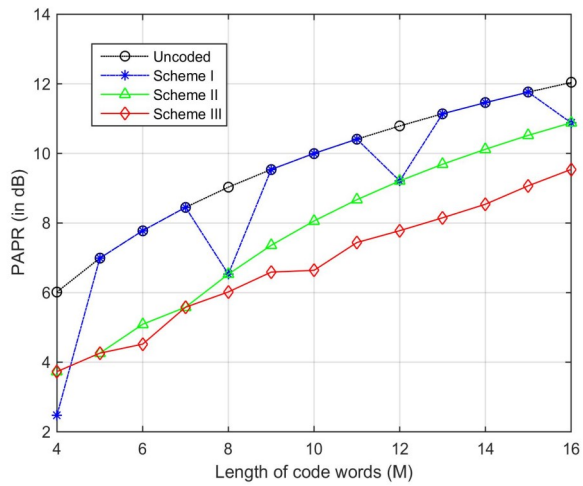

Figure 7. PAPR (in dB) Comparison for All Schemes

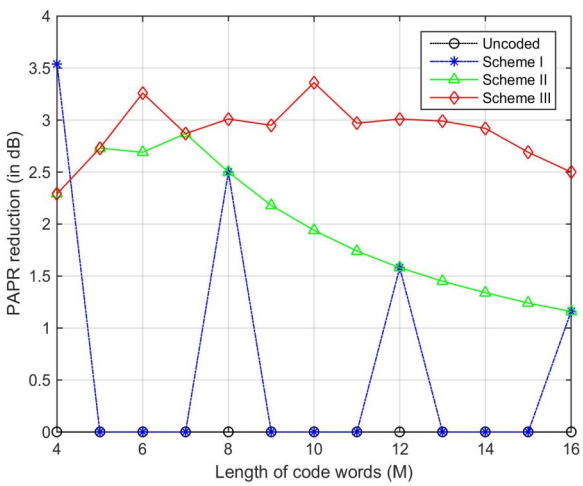

Figure 8. PAPR Reduction (in dB) for All Schemes

Conclusion

As a PAPR reduction scheme, a new block coding scheme, referred to as Scheme III, was created by adding two additional bits to Scheme I. Scheme I only reduces PAPR when the length of the code word is an integer multiple of four. This is the main drawback of Scheme I. Scheme II reduces PAPR even though the length of the code word is not an integer multiple of four. However, the PAPR reduction gains are marginal when the length of the code word increases. Scheme III shows improved performance compared to those of the two previous schemes, when the length of the code word increases. For example, the amount of PAPR reduction with M = 8 for Scheme I, Scheme II, and Scheme III are 2.50 dB, 2.50 dB, and 3.01 dB, respectively. For M = 16, they are 1.16 dB, 1.16 dB, and 2.50 dB, respectively. As a result, Scheme III is suited to large numbers of sub-carriers, though at the expense of two additional bits.

References

[1] Jones, A. E., Wilkinson, T. A., & Barton, S. K. (1994). Block Coding Scheme for Reduction of Peak to Mean Envelope Power Ratio of Multi-Carrier Transmission Schemes. *Electronics Letters*, 2098-2099.

[2] Fragiacomo, S., Matrakidis, C., & O'Reilly, J. J. (1998). Multi-Carrier Transmission Peak to Average Power Reduction Using Simple Block Code. *Electronics Letters*, 953-954.

[3] Stuber, G. L., Barry, J. R., Mclaughlin, S. W., Li, Y., Ingram, M. A., & Pratt, T. G. (2004). Broadband MIMO-OFDM Wireless Communications. *Proceedings of the IEEE*, *92*(2), 271-294.

[4] Iqbal, Z., Nooshabadi, S., & Lee, H. N. (2012). Analysis and Design of Coding and Interleaving in a MIMO-OFDM Communication System. *IEEE Transactions on Consumer Electronics*, *58*(3), 758-766.

[5] Cho, Y. S., Kim, J. W., Yang, W. Y., & Kang, C. G. (2013). *MIMO-OFDM Wireless Communications with MATLAB*. John Wiley & Sons (Asia) Pte Ltd.

[6] Han, S. H., & Lee, J. H. (2005). An Overview of Peak-to-Average-Power Ratio Reduction Techniques for Multicarrier Transmission. *IEEE Wireless Communications*, *12*(2), 56-65.

[7] Jiang, T., & Wu, Y. (2008). An Overview: Peak-to-Average Power Ratio Reduction Techniques for OFDM Signals. *IEEE Transactions on broadcasting,* 54(2), 257-268.

[8] Nee, R. V. (1996). OFDM Codes for Peak-to-Average-Power Reduction and Error Correction. *IEEE GLOBECOM*, 740-744.

[9] Tellambura, C. (1997). Use of M-Sequences for OFDM Peak-to-Average-Power Ratio Reduction. *Electronics Letters*, 1300-1301.

[10] Davis, J. A., & Jedwab, J. (1999). Peak to Mean Power Control in OFDM, Golay Complementary Sequences, and Reed-Muller Codes. *IEEE Transactions Information Theory*, *45*(7), 2397-2417.

[11] Zhang, Y., Yongacoglu, A., Chouinard, J. Y., & Zhang, L. (1999). *OFDM Peak Power Reduction by Sub-Block Coding and Its Extended Versions*. IEEE Vehicular Technology Conference, 695-699.

Biography

YOONILL LEE is currently an assistant professor of Electrical Engineering Technology at Purdue University Northwest. He earned his BS and MS degrees in Electrical Engineering from Yonsei University in Seoul, South Korea, in 1984, 1986, respectively; MS in Electrical Engineering from Oklahoma State University in 1992; and, PhD in Electrical Engineering from the University of South Florida in 2001. He also worked at Cisco Systems as a communications engineer. His research interests include CDMA, multi-carrier systems, and MIMO technology. Dr. Lee may be reached at lee2273@pnw.edu

BATTERY ENERGY STORAGE FOR A LOW-VOLTAGE DC MICROGRID SYSTEM

Dale H. Litwhiler, Penn State University; Nicholas Batt, Ecoult Energy Storage Solutions;
Jason Hoffman, Ecoult Energy Storage Solutions

Abstract

As part of an ongoing collaborative project with local industry, an advanced lead-acid battery energy storage system was designed and installed into an existing 24 VDC microgrid power system. A small rooftop solar array was used to provide energy for the lighting load in a laboratory and classroom space. A building grid-powered AC-DC power supply provided supplemental energy when the solar array could not meet the demand of the load. The energy was distributed throughout the space to the load via a two-conductor microgrid network embedded in the ceiling tile support framework. This ceiling grid energy distribution technology is available as a commercial product and was installed as part of an earlier collaboration with the manufacturer. In this latest phase of the project, advanced lead-acid batteries were added to the system to store surplus solar energy for later use. A PLC-based control system provided supervisory monitoring and control of the charging and discharging of the batteries. The installed energy storage system served as a testbed for similar projects under development by the industry partner. In this paper, the authors provide a brief overview of the 24 VDC microgrid system. The battery energy storage system motivation, design goals, and tradeoffs are also described. System hardware and software are presented and discussed. A simple system model developed to predict performance is also presented. Preliminary energy storage system performance data is discussed. Ongoing system improvements and lessons learned are also presented.

Introduction

An emerging technology in building power distribution involved the use of a room ceiling tile support grid to create a low-voltage microgrid network. With this network, 24 VDC power was routed throughout the room via conductors embedded in the drop-ceiling support structure. Users could then tap into the low-voltage supply from any location in the room. The microgrid effort was organized by a consortium of industry and university partners called the Emerge Alliance [1]. The Emerge Alliance promotes the use of low-voltage DC indoor power distribution for a variety of commercial, industrial, and residential applications. An example of applications on the load side includes lighting and ventilation devices. Input power for the microgrid can be derived from many sources including standard building AC power and alternative sources such as solar. A 24 VDC ceiling system was installed in one room of the engineering building at Penn State Berks. The room serves as both laboratory and classroom space. Students in the engineering technology programs have been involved with designing and fabricating devices to use and/or control power derived from the 24 VDC microgrid system. Devices include room lighting control and portable device charging stations. The low-voltage microgrid provides a relatively safe environment in which to experiment with new devices for occupied space environmental control [2].

The 24 VDC microgrid receives its energy from multiple sources. During periods of sunshine, the microgrid load energy is supplied primarily by a rooftop-mounted solar array. The system also contains an AC-DC power supply to maintain the 24 VDC bus voltage regulation during times when no other sources are available. The utility of the 24 VDC microgrid was further enhanced by incorporating battery energy storage into the system. Figure 1 shows a simplified system diagram.

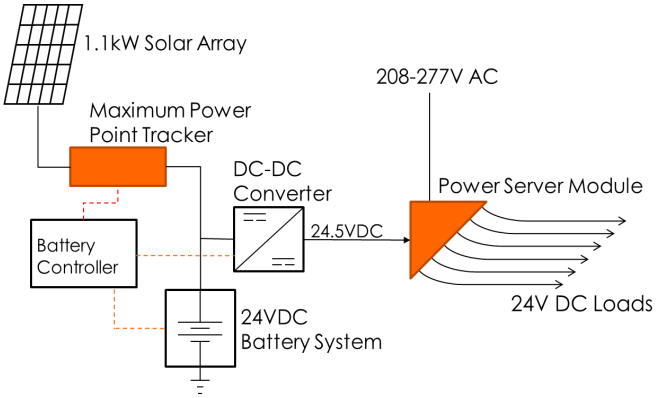

Figure 1. Simplified 24 VDC Microgrid System Diagram

Due to the intermittent occupancy of the room during daylight hours, there is significant opportunity to store otherwise unused energy collected by the solar array. The stored energy can then be used by the microgrid to supply the room load as needed. Together with industry partner Ecoult, an advanced lead-acid battery technology, UltraBattery®, energy storage system was developed and installed

as part of the 24 VDC microgrid. The UltraBattery® operates very efficiently in continuous Partial State of Charge (PSoC) use without frequent overcharge maintenance cycles. It can be utilized to continually manage energy intermittencies, smooth power, and shift energy, using a band of charge that is neither totally full nor totally empty [3]. The UltraBattery was developed by the CSIRO in Australia and taken to market by Ecoult [4]. The installed system is very similar to that already commissioned in Australia to power remotely located cellular telephone tower equipment [5].

Figure 1 shows how energy from the solar array (five Canadian Solar 235W panels) is processed by the maximum power point tracker (MPPT) unit (MidNite Solar Classic 250). The DC-DC converter (Vicor MegaPAC, 1600 watts) provides a regulated 24.5 VDC output voltage, while the battery voltage varies depending on its State of Charge (SoC). The control algorithm of the battery controller provides control signals to the MPPT and DC-DC converter, based on the SoC of the battery. When the battery SoC is in the range where it could accept charge, the MPPT is enabled. Likewise, when the SoC of the battery is in a suitable range for providing energy (discharging), the DC-DC converter is enabled. When the DC-DC converter is enabled, its 24.5 VDC output voltage overrides the 24 VDC produced by the AC-DC converter in the Power Server Module. Thus, no energy is drawn from the AC line to supply the bus loads, it is all provided by the battery via the DC-DC converter.

Battery Selection and Sizing

The intermittent nature of solar energy and the sporadic demand profile of the room lighting load align well with the performance capability of the UltraBattery. As shown in Figure 2, the UltraBattery's construction incorporates a traditional lead-acid battery in parallel with a supercapacitor structure. This combination produces an energy storage package that performs very well under partial state-of-charge conditions, as are typically experienced in this type of application. The laboratory/classroom space is lit by ceiling fluorescent lighting fixtures. These fixtures were equipped with electronic dimming ballasts designed for 24 VDC input voltage. The ballasts receive their input voltage from the microgrid with a total power of about 850W at full brightness. The initial design used this load power and a goal of providing enough energy to sustain this load for two hours (the typical duration of an evening laboratory class session). Therefore, the battery was sized at a nominal energy rating of 2 kWh. The battery arrangement was then four, 12V battery units configured as two parallel strings of two batteries each.

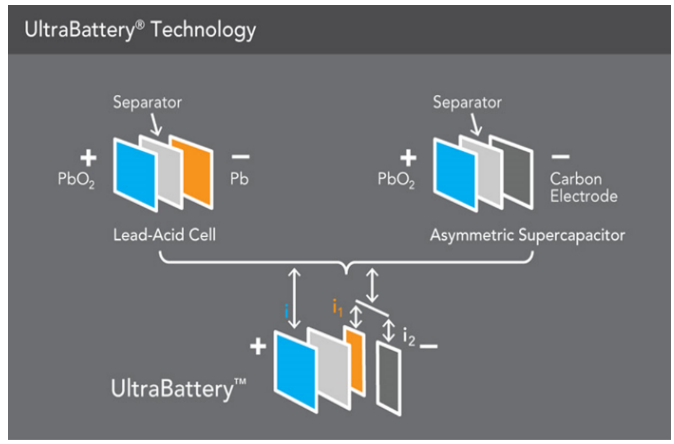

Figure 2. UltraBattery Construction Diagram

Figure 3 shows that each of the four batteries in the energy storage system was equipped with battery-monitoring electronics mounted directly on the positive and negative terminals. The monitoring hardware and software continuously measured key parameters of voltage, current, and cell temperature and could also be configured to monitor ambient temperature and gas concentrations for enhanced safety and performance.

Figure 3. Battery Monitor Mounted on an UltraBattery

Figure 4 shows the batteries housed in an industrial battery cabinet. Each battery monitor was connected to the main monitoring and control electronics via infrared link to provide galvanic isolation and eliminate grounding issues. Remote monitoring and control of the entire battery system was accomplished with a web-enabled PC contained within the battery cabinet control compartment. This arrangement also provided a means for remote software updates and system troubleshooting. For the system installed on campus, a wired LAN connection is used, however, a cellular connection was used for previous similar systems installed in remote locations.

Figure 4. Battery Cabinet and Control/Monitoring Electronics Enclosure

Control System Architecture

The battery controller was implemented using a Programmable Logic Controller (PLC). The primary function of the PLC is to monitor the batteries and protect them from overcharging or over-discharging. This function is accomplished by controlling the MPPT (the battery charging component) and the DC-DC converter (the battery discharging component). A simple discrete enable/disable signal is sent from the PLC to the MPPT and the DC-DC converter based on the current SoC of the battery. A diagram of these control signals is shown in Figure 5. A small bit of hysteresis was added to each signal to minimize excessive system cycling near the extremes of the SoC.

System Modeling

To get a first-order estimate of expected system performance, a simple discretized system model was developed to describe the battery state-of-charge for various solar array power and DC bus load power profiles. Equation (1) shows a simplified linear model (constant) for the battery SoC that was used:

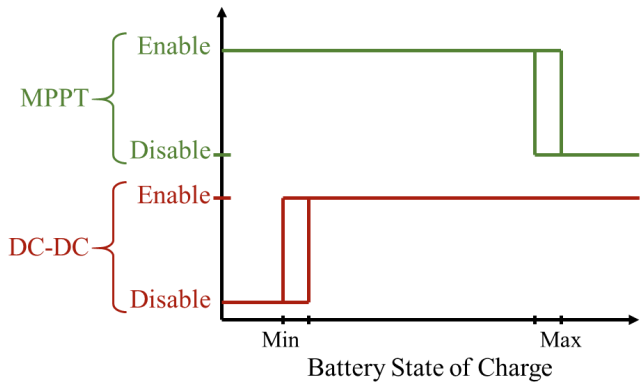

Figure 5. Battery Charge and Discharge Enable Signal Hysteresis Curves

$$K_{SoC} = \frac{SoC_{Max} - SoC_{Min}}{\text{Wh capacity}} \quad \% / \text{Wh} \tag{1}$$

A discrete time step of one minute was used for the simulation. The change in stored energy during each time step can be calculated using Equation (2), a Coulomb-counting method [6]:

$$\Delta E = [(P_{Solar})(Eff_{MPPT}) - (P_{Load})/Eff_{DC\text{-}DC}]/60 \quad \text{Wh} \tag{2}$$

where, P_{Solar} is the output power of the solar array; Eff_{MPPT} is the input-output efficiency of the MPPT unit; P_{Load} is the power consumed by the room lighting load; and, $Eff_{DC\text{-}DC}$ is the input-output efficiency of the DC-DC converter.

The model was implemented in Matlab. Table 1 shows the generic pseudocode.

Table 1. Listing of System Model Pseudocode

```
Loop{
ΔE = ((P_Solar)*(Eff_MPPT) – (P_Load)/(Eff_DC-DC))/60
if ((ΔE > 0 AND OK2Chrg = True) OR (ΔE < 0 AND
OK2Dischrg = True))
        SoC = SoC + K_SoC *(ΔE)
if ((SoC < Max AND OK2Chrg = True) OR (SoC < (Max –
Hyst))
        OK2Chrg = True
else
        OK2Chrg = False
if ((SoC > Min AND OK2Dischrg = True) OR (SoC > Min +
Hyst))
        OK2Dischrg = True
        V_Bus = 24.5
else
        OK2Dischrg = False
        V_Bus = 24.0
}
```

Using this simple system model, various profiles for available solar energy, P_{Solar}, and room lighting load, P_{Load}, could be explored to see the effects on the SoC profile. In the actual Matlab code, the P_{Solar} and P_{Load} arrays were contained in spreadsheet files which were imported when the simulation was run. Figure 6 shows the simulation results for typical solar array power (~900W) and room lighting load (~ 850W) profiles. Efficiencies used for the MPPT and DC-DC converter were 90% and 80%, respectively. The SoC limits were SoC_{Min} = 30% and SoC_{Max} = 80%.

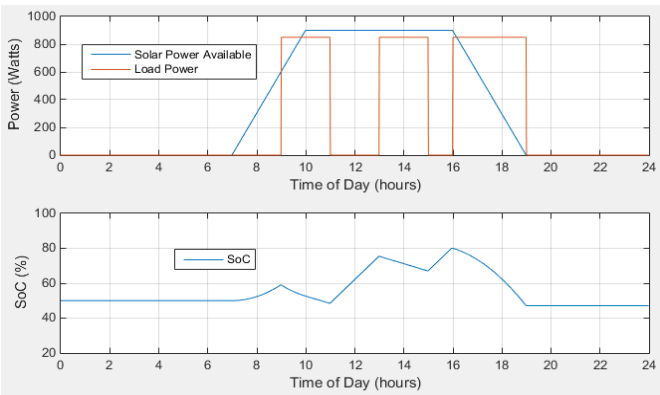

Figure 6. First Example of System Simulation Results

Figure 6 shows how the SoC begins at a random initial value (energy leftover from the previous day) and begins to increase when solar power becomes available at sunrise. The intermittent use of the room is indicated by the rectangular load power profile. Due to the inefficiency of the MPPT and the DC-DC converter, the solar array was not quite able to supply the entire lighting load, therefore a slight discharge occurred during those intervals. However, during times when the room was unoccupied, significant charging occurred. The net change in the SoC for the day was slightly negative for this profile combination.

Figure 7 shows the simulation results for a different load profile. In this example, the solar power input profile is the same as the first example. The load profile shows some periods of reduced demand (only some of the room lighting turned on), as would typically be experienced in the actual room. In this scenario, the net change in the SoC for the day was positive.

System Data

Battery data were collected and stored by the system's PC at a sampling rate of about one sample each 10 seconds. Each battery monitor unit measured and reported the battery's voltage, current and temperature. State-of-charge was calculated using a proprietary algorithm. Figure 8 shows a plot of data for an early spring day with significant sunshine and typical room lighting profile. For the day shown, the battery began with a significant SoC and ended the day nearly exhausted. On the subsequent day, a lighter load allowed for a substantial recharge of the battery, thus producing an overall reduction in grid power used by the room lighting load when averaged over several days.

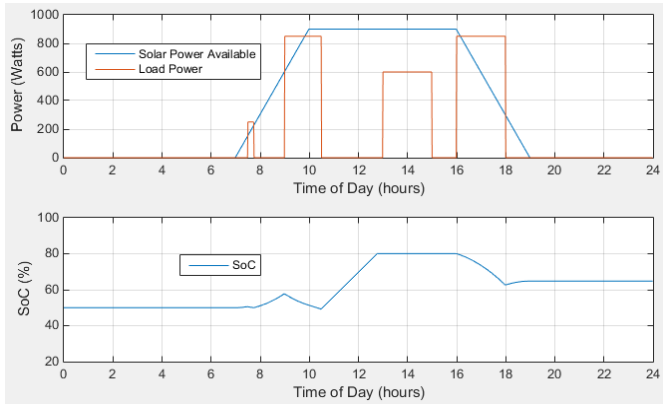

Figure 7. Second Example of System Simulation Results

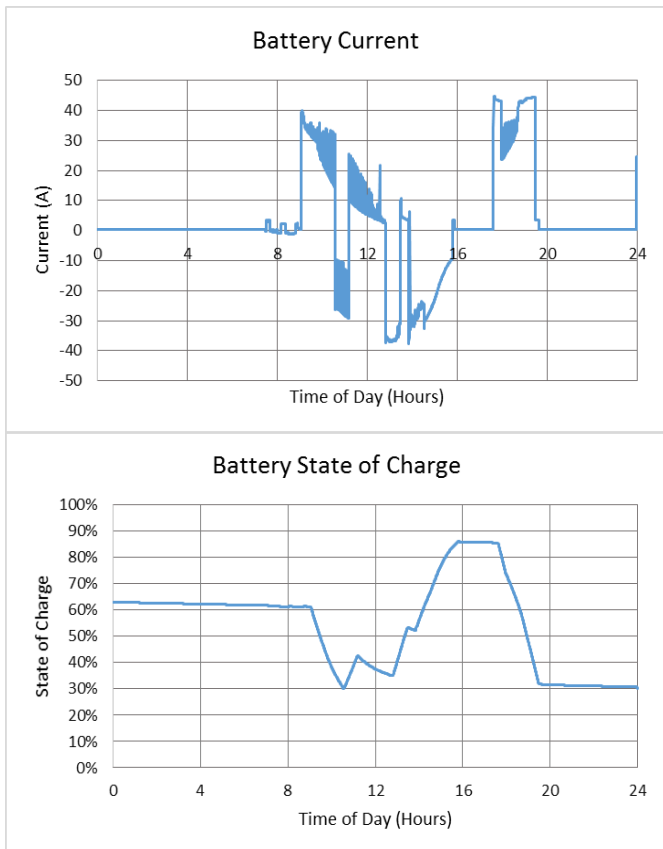

Figure 8. System Data for a Sunny Day with Typical Room Load Profile

Ongoing Work

The 24 VDC microgrid installation continues to evolve. Efficiency improvement changes on both the distribution and consumption of the microgrid energy were underway at the time of the writing of this paper. A grant has also been received to help support research to develop better system models for this type of application. The DC-DC converter consumed a large amount of quiescent energy from its input side just to power the cooling fan and other supervisory electronics, even when the unit was disabled. This energy was taken from the batteries and, during periods of sustained cloudiness, can cause the SoC to drop below the design minimum. A change is being developed to provide a solid-state switch disconnect between the battery and the DC-DC converter. A similar switch will also be installed on the output side of the DC-DC converter to minimize quiescent loading on the 24 VDC bus. On the load side, the consumed power can be reduced by managing the light level in the room, rather than just allowing users to turn the lights on or off. The installed fluorescent ballasts are dimmable so this change could be implemented with minimal hardware changes.

The current model for the battery state of charge as a function of input/output power is very simplistic. Although many parameters would be needed to completely model the energy system behavior, significant improvement can be achieved by including a few key parameters in a new empirical behavioral model. Performance data will be used to help develop this model. Also, as more data are obtained on the UltraBattery, the SoC limits may be able to be widened to make use of even more stored energy for a given battery size.

Conclusions

The 24 VDC microgrid is an evolving technology. Low-voltage DC allows for more experimentation and faster development of technology than higher voltages which impose more safety and regulatory restrictions. Energy storage and alternative energy sources can easily be added to the 24 VDC microgrid. Although in this study energy storage was added at the top level (the main 24V bus), energy could be injected into or stored in any of the 96 watt, class-2 partitions of the microgrid. With proper modeling, the energy storage system can be appropriately sized to meet the load requirements. Proper sizing will also help to ensure that the system uses minimal energy from the AC grid.

References

[1] Merge Alliance. Retrieved from http://www.emergealliance.org

[2] Litwhiler, D. H., & Wiggins-Lopez, E. (2013). Low Voltage Power Distribution System Provides Incubator for Energy-Related Student Projects. *ASEE Annual Conference*, Atlanta, Georgia.

[3] UltraBattery. Ecoult Energy Storage Solutions. Retrieved from http://www.ecoult.com/technology/ultrabattery.

[4] Background—Ecoult Energy Storage Solution. Retrieved from http://www.ecoult.com/media/background.

[5] Batt, N. (n.d.). Ecoult: Hampton Project—Utilising storage technologies to smooth ramp rates, moderate peaks and troughs in wind output and variability. Retrieved from http://www.slideshare.net/informaoz/7-nicholas-batt-ecoult

[6] Chang, W. Y. (2013). The State of Charge Estimating Methods for Battery: A Review. *ISRN Applied Mathematics*, *2013*. http://dx.doi.org/10.1155/2013/95379

Biographies

DALE H. LITWHILER is an associate professor at Penn State, Berks Campus. He received his BS from Penn State University, MS from Syracuse University, and PhD from Lehigh University, all in electrical engineering. Prior to beginning his academic career, he worked with IBM Federal Systems and Lockheed Martin Commercial Space Systems as a hardware and software design engineer. Dr. Litwhiler may be reached at dale.litwhiler@psu.edu

NICHOLAS BATT leads the Application Engineering team at Australian energy storage provider Ecoult. His team works across kW and MW systems. The team seeks out new applications that can benefit from the Ecoult UltraBattery, invented by CSIRO in Melbourne Australia. Nicholas has over 10 years of experience as a Power and Control engineer, and has focused on renewable energy and smart grids. Mr. Batt may be reached at nicholas.batt@ecoult.com

JASON HOFFMAN is a senior engineer with Ecoult. He is focused primarily on managing the design and implementation of large-scale grid-connected energy storage systems. He received his BS from Bucknell University and his MS from Penn State University, both in electrical engineering. Following his education, he has been working in the power industry, primarily in the renewable energy and energy storage areas. Mr. Hoffman may be reached at Jason.hoffman@ecoult.com

MEASURED AND SIMULATED PERFORMANCE OF A GRID-CONNECTED PV SYSTEM IN A HUMID SUBTROPICAL CLIMATE

Fredericka Brown, The University of Texas at Tyler; Racquel Lovelace, The University of Texas at Tyler

Abstract

In this paper, the authors describe research aimed at determining the measured and predicted performance of a photovoltaic grid-connected system in a humid subtropical climate. The performance was modeled and the predicted performance of the systems was compared to the experimentally collected data for the system. In addition, the research allowed for long-term simulation analysis of the system under varying conditions and can assist with the optimization of the photovoltaic system.

Introduction

As the global population increases along with the advancement of human development and technology, so does the increase in global energy demand. According to the U.S. Energy Information Administration's 2013 report, the world energy consumption was expected to grow by 56% between 2010 and 2040, from 524 quadrillion British thermal units (Btu) to 820 quadrillion Btu [1]. Through these projections, it was estimated that fossil fuels will continue to supply roughly 80% of the world's energy through 2040 [1]. Fossil fuels are non-renewable resources with supplies that are being drastically depleted. It was calculated that the depletion time for oil, gas, and coal was to be about 35, 37, and 107 years, respectively [2]. Though the accurate timing for fossil fuel depletion is an arguable topic among researchers and scientists, it is an inarguable fact that fossil fuels cannot last forever at current usage rates. The increase in demand for energy coupled with the knowledge of depleting fossil fuels has led to an increase in demand for research into developing alternatives to using fossil fuels, the most viable being solar energy by means of photovoltaic (PV) modules.

PV production has been doubling every two years, increasing by an average of 48% each year since 2002, making it the world's fastest-growing energy technology [3]. PV systems depend on a variety of factors including weather, irradiation levels, temperature, and efficiencies in all components of the system. Various methods have been developed to determine the maximum power output of these photovoltaic systems to improve overall efficiency. In this study, the authors aimed to determine and analyze the power output of a photovoltaic grid-connected system using the TRNSYS simulation program, compared to the recorded performance of the system.

Description of the System

The University of Texas at Tyler's Texas Allergy, Indoor Environment and Energy (TxAIRE) Institute developed realistic test facilities for the development and demonstration of new technologies related to energy efficiency. The photovoltaic system used for this study was the system supplying the energy for TxAIRE House 2, a net-zero energy house with all the power provided by the PV system. It is located in Tyler, Texas, which is classified as a humid subtropical climate.

The house has a photovoltaic grid-connected system, consisting of 33 SolarWorld SunModule Plus polycrystalline 225-watt solar panels, rated at 7.4 kW. Tables 1 and 2 show the performance standards under standard test conditions as well as the thermal characteristics as supplied by the manufacturer on the data sheet, respectively, for the solar modules. The photovoltaic modules cover an area of 590 ft^2 and are situated 25 ft away from the roofline of the house and are at a 55.8º angle as shown in Tables 1 and 2.

Table 1. Performance under Standard Test Conditions of 1000 W/m2, 25ºC, AM 1.5

Characteristic	Variable	SW 225
Maximum power	P_{max}	225 Wp
Open circuit voltage	V_{oc}	36.8 V
Maximum power point voltage	V_{mpp}	29.5 V
Short circuit current	I_{sc}	8.17 A
Maximum power point current	I_{mpp}	7.63 A

Table 2. Thermal Characteristics of Solar Panels

Characteristic	Parameter
NOCT	45ºC
TC I_{sc}	0.034 %K
TC_{Voc}	-0.34 %K
TC P_{mpp}	-0.48 %K
Operating range	-40ºC to 90ºC

The solar panels used for this study were installed in three circuits of eleven modules per circuit for a total of 33 modules (see Figures 1 and 2). This array converts the solar radiation into DC electricity, while an inverter unit, SMA Technology model #SB7000US, converts the DC electricity to AC so that it can feed into the house's electrical system.

Figure 1. Back View of Photovoltaic Panels

Figure 2. Front View of Photovoltaic Panels

The archival data used for comparison in this study were the PV performance and weather data collected from TxAIRE House 2, from August 17, 2012, to December 31, 2014. The variables of interest in terms of PV performance included solar panel energy (W) and the total solar radiation on the tilted surface (W/m^2). The radiation data were recorded as total radiation. The TRNSYS program requires that data be input as beam and diffuse radiation; therefore, the assumption that beam was approximately 85% of the total and diffuse was 15% the total recorded radiation was split into the two before being input into the program. Weather data were also collected throughout the same time period. The variables of interest in terms of weather data were temperature (°F) and wind speed (mph).

The data for the house were collected using the NI-cRIO-9074 processor, a 400 MHz industrial real-time processor for control, data logging, and analysis. PR-T24 thermocouple wires and polyvinyl insulated wires were also used in retrieving the outside temperature. The data acquisition system (DAQ) was connected by USB to a personal software notebook to retrieve the data. The weather data were collected from a Davis Vantage Pro 2 weather station situated above the TxAIRE House 2 on the roof as Figure 3 shows. Data were collected every 30 minutes for the time period used for this study for weather and PV performance.

Figure 3. Location of the Weather Station on the Roof of the TxAIRE House 2

System Modeling in TRNSYS

TRNSYS was the software package used to simulate the PV system. It uses a one-diode, five-parameter model, as developed by De Soto [4]. The simulation had the basic outline as shown in Figure 4 and used the following components: Type9 (user-entered data labeled as weather data),

unit conversion (to convert units to SI), Type 194b PV-Inverter (uses a five-parameter model, as presented by De Soto, labeled as PV-Inverter) and Type65d (graphs the output data labeled as graph output). The component labeled "Start and Stop Times" was the area in which to input the start and stop times of the simulation. Weather data were input into the Type9 component as a CSV file with temperature, total radiation on the tilted surface, and wind speed, along with the date and time. These values were then converted into SI units with the unit conversion component and input into the Type 194b PV-Inverter component and output graphically using Type65d. The components labeled radiation and power output, voltage, and current also output those data points for the simulation as a .dat file that could then be opened with Excel.

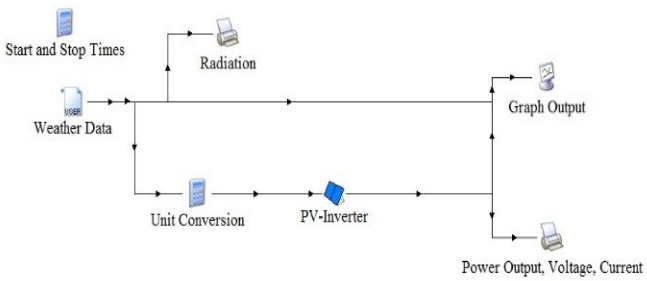

Figure 4. TRNSYS Simulation Setup

The first part of the system included the controls, labeled as start and stop times, which were input into this component in terms of hours of the year. For example, if the data file started on the 145th day of the year at midnight, then the input for start time would be 3480 (24x145). One of the most important components in the simulation was the Type9 component (labeled weather data). Type9 is a component that reads data at regular time intervals from a user-defined data file. This allows the user to input data from weather data recorded experimentally rather than data from the weather database that are included in the TRNSYS package. The component read the data for the solar radiation, temperature, and wind speed and output them to the unit converter in terms of W/m^2, Fahrenheit, and mph, respectively. The unit conversion component then converted the units to SI units (radiation had been converted to kJ/m^2, the temperature to Celsius, and the wind speed to m/s) to be input into the Type194b PV-Inverter component.

The most important component in the simulation was the Type194b PV-Inverter component. Type194b determines the electrical performance of a photovoltaic array and may be used with simulations involving electrical storage batteries, direct load coupling or utility grid connections such as the system used in this study. The model determines the current and power of the array at a specified voltage and will also output the current and voltage at the maximum power point. This component uses De Soto's one-diode, five-parameter model to calculate the PV performance. Other components in TRNSYS determine the output of PV systems; however, this component differs from the others because it also considers the inverter's effects and efficiency. Therefore, this component was chosen to model the PV system because of the added calculation of the inverter efficiency. The inputs of the component came from two sources. One source was the output of the Type9 weather data file, which contained the solar radiation, temperature, and wind speed. The other source was from the user of the solar panel parameters mentioned in Tables 1 and 2.

The last part of the simulation file output the data from Type194b into a graph using component Type65d, an online graphics component used to display selected variables, while the simulation was progressing. The component was used to display solar radiation, temperature, wind speed, and PV power against date and time. The power at maximum power point, open-circuit voltage, and the short-circuit voltage were also output into an external data file.

Results and Discussion

PV performance was determined using the TRNSYS simulation software; the recorded weather data served as input variables. Figure 5 shows the graphical output of the TRNSYS software as a comparison of all the variables (date/time, total incident radiation, temperature, and wind speed) with the predicted PV output, as determined using the five-parameter model in the software package.

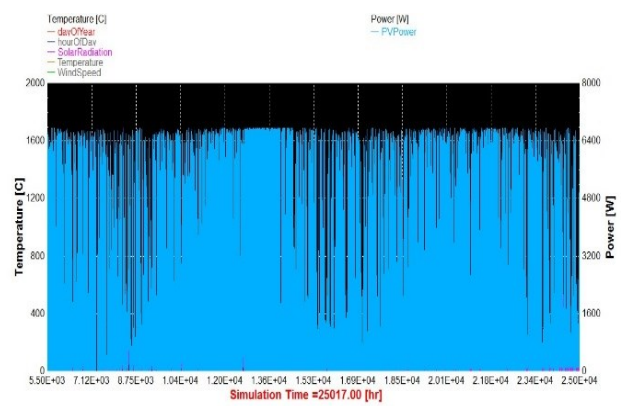

Figure 5. TRNSYS Output Results of Solar Radiation and Power Over Time

As shown, the TRNSYS simulation had a max power output of 6770.99 watts, showing a 9.2% difference from the manufacturer-calculated max power of 7425 watts. To determine the accuracy of the simulation, the power output

was compared to the power output as recorded by the NI-cRIO-9074 data logging processor for the years used in this study. Figure 6 shows the correlation between the predicted PV output and the recorded output as a function of radiation. The average value for recorded power was calculated to be 783 watts with a max of 7095 watts. The average value for predicted power calculated by TRNSYS was 1052 watts with a max of 6771 watts. The percent difference between the averages was -29% and the maximum was -5%.

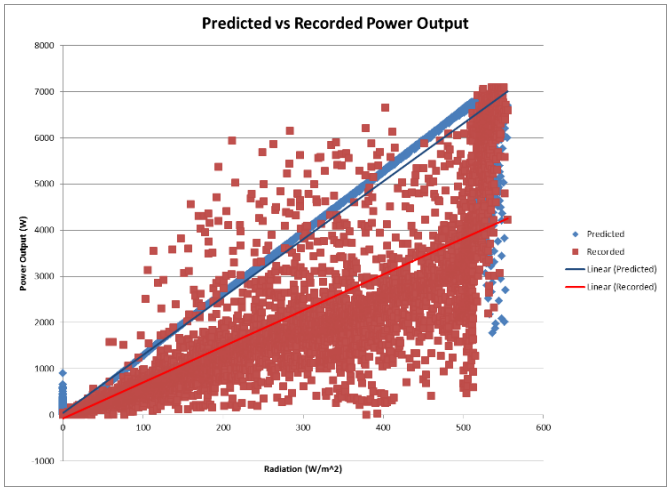

Figure 6. Predicted versus Recorded Power Output in Terms of Radiation

Statistical Analysis

To compare the recorded data to the TRNSYS data, a statistical analysis was conducted using an analysis of variance (ANOVA) in *Excel*. The maximum daily values of power output of the recorded data were compared to the maximum daily values of power output supplied by TRNSYS. The ANOVA determined whether or not there was a difference in the data. H_0 represented no difference in the data and H_1 represented differences in the data. If the resulting P value were less than alpha (alpha, in this case, was 0.05), H_0 would be rejected and the H_1 condition accepted as true; if the P value were greater, then the opposite would be true. Three ANOVA scenarios were run: 1) using the complete data sets (August 2012-December 2014), 2) using only the summer months (June-September), and 3) using only the winter months (December-March).

Figure 7 shows the results of the first analysis. Using the data set for the complete time, the resulting P value was 6.97E-27, which indicates a difference between the two data sets. The average of the maximums for the recorded data was 5157 watts with the average of the maximums for the TRNSYS data being 6002 watts. The TRNSYS data were over predicting the power output. As a maximum, TRNSYS under predicts the data, as shown in Figure 6.

Total						
Anova: Single Factor						
SUMMARY						
Groups	*Count*	*Sum*	*Average*	*Variance*		
Column 1	859	4429803.00	5156.93	3260446.02		
Column 2	859	5155426.26	6001.66	1880342.94		
ANOVA						
Source of Variation	*SS*	*df*	*MS*	*F*	*P-value*	*F crit*
Between Groups	306477944.75	1	306477944.75	119.23	6.97E-27	3.85
Within Groups	4410796928.14	1716	2570394.48			
Total	4717274872.89	1717				

Figure 7. ANOVA Analysis of Statistical Comparison of TRNSYS Total Power Output and Recorded Power Output

The next analysis was run using only data from the summer months. Figure 8 shows the results. This resulted in a P value of 1.65E-74, again showing a difference between the two data sets and a larger difference than using the entire data set. The average of the recorded data was 4070 watts and the average of the TRNSYS output was 6616 watts. The last analysis used only data from the winter months. The resulting P value was 0.204, meaning that there was not a difference in the data (see Figure 9). The average of the recorded data was 5176 watts and the average of the TRNSYS data was 5493 watts.

Summer2013						
Anova: Single Factor						
SUMMARY						
Groups	*Count*	*Sum*	*Average*	*Variance*		
Column 1	122	496485.00	4069.55	780638.17		
Column 2	122	807155.76	6616.03	317253.12		
ANOVA						
Source of Variation	*SS*	*df*	*MS*	*F*	*P-value*	*F crit*
Between Groups	395558685.26	1	395558685.26	720.58	1.65091E-74	3.88
Within Groups	132844846.16	242	548945.65			
Total	528403531.42	243				

Figure 8. ANOVA Analysis of Statistical Comparison of TRNSYS Power Output and Recorded Power Output during the Summer Months

The analysis showed a difference in the data sets, evident in the summer months, while the winter months showed no difference. TRNSYS over predicted during the summer months but accurately predicted in the winter months. Based on Figure 6, the hourly data showed that the TRNSYS data were higher than the recorded data on average but were lower at the maximum power.

Winter2013						
Anova: Single Factor						
SUMMARY						
Groups	*Count*	*Sum*	*Average*	*Variance*		
Column 1	121	626343.00	5176.39	4561738.06		
Column 2	121	664614.61	5492.68	2905151.97		
ANOVA						
Source of Variation	*SS*	*df*	*MS*	*F*	*P-value*	*F crit*
Between Groups	6052546.50	1	6052546.50	1.62	0.20	3.88
Within Groups	896026802.66	240	3733445.01			
Total	902079349.16	241				

Figure 9. ANOVA Analysis of Statistical Comparison of TRNSYS Power Output and Recorded Power Output during the Winter Months

Root mean square error (RMSE), mean absolute deviation (MAD), absolute percentage error (MAPE), and model efficiency (EF) were also used to compare the recorded data to the simulated data. The RMSE is given by Equation (1):

$$RMSE = \sqrt{\frac{1}{n}\sum_{t=1}^{n}(H_t - F_t)^2} \tag{1}$$

where, H_t is the recorded value; F_t is the simulated value; and, n is the number of values in the data set. RMSE was used to measure the differences between data set values, with the best results being as close to zero as possible.

The mean absolute deviation was used to calculate the average distance from each data point to the mean of the recorded data. MAD is given by Equation (2):

$$MAD = \frac{1}{n}\sum_{t=1}^{n}\left|(H_t - F_t\right| \tag{2}$$

Absolute percentage error is another measure of accuracy between the recorded and simulated data points, defined by Equation (3):

$$MAPE = \frac{1}{n}\sum_{t=1}^{n}\left|\frac{(H_t - F_t)}{H_t}\right| \times 100\% \tag{3}$$

The last method for determining accuracies between the data points used Equation (4) for model efficiency:

$$EF = \frac{\sum_{t=1}^{n}(H_t - z)^2 - \sum_{t=1}^{n}(F_t - H_t)^2}{\sum_{t=1}^{n}(H_t - z)^2} \tag{4}$$

where, z is the average value of the recorded data.

Table 3 shows the TRNSYS model accuracy results. The values for RMSE and MAD were higher than desired, though they matched the ANOVA analysis, showing differences in the average data though similar data for the maximum.

Table 3. Model Accuracy Analysis Results Using RSME, MAD, MAPE, and EF

RMSE	MAD	MAPE (%)	EF (%)
1468	-884	34.88%	33.85%

Effects of Radiation, Temperature, and Wind Speed

To further develop the simulation model, radiation, temperature, and wind speed data were purchased for 10 years, from 2004 to 2014 for the Tyler, Texas, area from Meteonorm and used in the TRNSYS simulation model. The differences in data between the recorded and the purchased sources showed a 1.3% difference between the temperature data, 41.5% difference in the wind speed data, and a 30.8% difference in the radiation data. The wind speed data were not used in the simulation, and the results ended with an 88% difference of the TRNSYS results with the purchased data and the recorded data.

Due to the differences in the data results, during the analysis of the TRNSYS simulation power output compared to the recorded power output, the effects of the variables of radiation, temperature, and wind speed were reviewed. The results showed that radiation was the leading factor in determining power output, as compared to temperature and wind speed. According to Khatib et al. [5], the power produced by PV systems is proportional to the amount of the solar radiation it collects. Standard test conditions (STC) assume 1000 W/m^2; Khatib et al. explained that if only half of the STC conditions are available then the PV output will also only produce about half of the power. It was also explained that temperature negatively affects the power output of PV systems.

As ambient temperature increases, the cell temperature also increases. With each 1°C increase of cell temperature, the PV module's power decreases by 0.5-0.6%. Bhattacharya et al. [6] showed a correlation coefficient value, R, between ambient temperature and PV performance to be 0.9642, suggesting a strong positive correlation between the two. The value of the coefficient of determination, R^2, was determined to be 0.9297, meaning that a 92.97% correlation between the variables indicating a direct proportionality. According to Bhattacharya et al., the value of the correlation

coefficient between wind speed and PV performance is 0.6857, with a coefficient of determination of 0.4702. This means that 52.68% of the total variation in the PV performance variable is unexplained.

Conclusions

The results of this study showed that in determining the performance of a PV grid-connected system, the following should be taken into account:

- The weather data have the most significant effect on prediction performance, with the most effect coming from the radiation data followed by temperature and lastly wind speed. Therefore, carefully selecting the correct weather data set is crucial, particularly for the radiation data.
- The TRNSYS simulation was able to accurately predict the max power output within 5% difference; however, the average prediction had a 45% difference with most of the difference coming from calculations during the summer months.

Though accuracy can be increased with the addition of the losses due to shading, dirt, differences with the nominal power, mismatch, and temperature, as well as additional data for radiation, the model using TRNSYS was determined to provide an accurate model of power performance. This model is simple but accurate and can help to design future PV systems in the East Texas area as well as help to improve current PV systems.

Acknowledgments

The investigative effort presented in this paper was completed in the frame of research work in the Department of Mechanical Engineering, University of Texas at Tyler, Texas, master's program. The authors gratefully acknowledge Dr. Fredericka Brown for her support and guidance in the research work for this paper, and Dr. Harmonie Hawley for her support in the statistical analysis of this study.

References

[1] US Energy Information Administration. (n.d.). *2013 world energy consumption*. Retrieved from http://www.eia.gov/todayinenergy/detail.cfm?id=12251

[2] Shahriar S., & Topal, E. (2009). When will fossil fuels reserves be diminished? *Energy Policy*, *37*, 181-189.

[3] Kropp, R. (2009, March 3). Solar expected to maintain its status as the world's fastest-growing energy technology. *Sustainability Investment News*. Retrieved from http://www.socialfunds.com/news/article.cgi/2639.html

[4] De Soto, W., Klein, S. A., & Beckman, W. A. (2006). Improvement and validation of a model for photovoltaic array performance. *Solar Energy*, *80*, 78-88.

[5] Khatib, T., Mohamed, A., Mahmoud, M., & Sopian, K. (2012). A new approach for meteorological variables prediction at Kuala Lumpur, Malaysia, using artificial neural networks: Application for sizing and maintaining photovoltaic systems. *Journal of Solar Energy Engineering*, *134*(2), 021005-021005-10. doi:10.1115/1.4005754

[6] Bhattacharya, T., Chakraborty, A. K., & Pal, K. (2014). Effects of ambient temperature and wind speed on performance of monocrystalline solar photovoltaic module in Tripura, India. *Journal of Solar Energy*, *2014*, id #817078. doi: http://dx.doi.org/10.1155/2014/817078

Biographies

FREDERICKA BROWN is currently an associate professor of Mechanical Engineering at The University of Texas at Tyler. She earned her BS degree in Physics from Xavier University; MS and PhD degrees in Mechanical Engineering from The University of Nevada, Las Vegas; and, an MBA from The University of Texas at Tyler. Dr. Brown is currently teaching at The University of Texas at Tyler. Her research interests include renewable energy and thermal system design. Dr. Brown may be reached at fbrown@uttyler.edu

RACQUEL LOVELACE is an engineer at STEMCO LP. She earned her BS degree in Mechanical Engineering from Kettering University and MS in Mechanical Engineering from The University of Texas at Tyler. Her research interests include renewable energy and thermal system design. Ms. Lovelace may be reached at rlovelace@patriots.uttyler.edu

THE EFFECTS OF ANCHOR ROD FAILURE ON THE PERFORMANCE OF THE NEW BAY BRIDGE TOWER

Abolhassan Astaneh-Asl, University of California, Berkeley; Maryam Tabbakhha, University of California, Berkeley;
Xin Qian, University of California, Berkeley

Abstract

The single tower of the new Bay Bridge opened in 2013, and was connected to its footing by 424 high-strength ASTM A354 BD, hot-dip galvanized anchor rods. The bridge was expected to experience strong earthquakes from the nearby Hayward or San Andreas faults. Bridge specifications did not recommend the use of ASTM A354 BD hot-dip galvanized anchor rods, due to the high probability of hydrogen embrittlement in these anchor rods leading to their fracture. A few months before the bridge opened, 32 A354 BD anchor rods fractured after tightening. In this study, the authors investigated the pushover behavior of the main tower of the SAS Bay Bridge in the likely event of fracture of the anchor rods at the base of the tower due to hydrogen embrittlement. At least two anchor rods have already fractured at this writing.

In this project, the pushover behavior of the main bridge tower without anchor rods connecting its base to the pile cap footing was analyzed through numerical simulation. A realistic non-linear model of the tower was created in ANSYS. The bridge tower, base plate, and the concrete-steel composite pile cap were modeled in detail. No anchor rods were included in the model to connect the tower to the footing. After applying the gravity load, the top of the tower was pushed in the transverse direction until it collapsed. The results of the realistic pushover analysis indicated that the lateral strength of the tower drops relatively fast after the peak, due to local buckling of the legs of the main tower, yielding of the base plate, and crushing of the concrete under the base plate.

During late stages of the pushover, the partial joint penetration (PJP) welds connecting the tower to the base plate also fractured. When the anchor rods are in place and tightened, these PJP welds are in compression; however, without the anchor rods, the welds will be directly subjected to tension and eventually fracture. The bridge design team indicated that the anchor rods were not needed. The authors of this current study, however, question the validity of the statement and suggest the implementation of necessary retrofit measures to restore the strength, stiffness, and ductility of the tower.

Introduction

The new East Spans of the San Francisco-Oakland Bay Bridge is a self-anchored suspension (SAS) bridge with a single tower. The bridge opened to traffic in 2013 and is located between two active seismic faults, the Hayward and San Andreas faults. Figure 1 shows the elevation and plan view of the new self-anchored suspension Bay Bridge. More information on the properties of the bridge can be found in studies by Astaneh-Asl and Qian [1] and Caltrans [2].

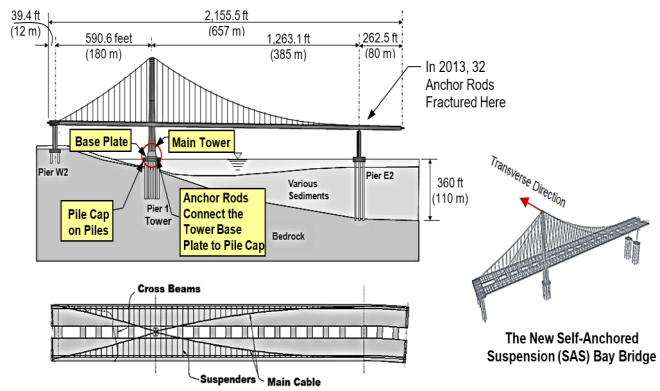

Figure 1. Elevation and Plan View of the SAS Bay Bridge

Figure 2 shows the pile cap, a concrete-steel composite box, supporting the tower. The shafts, as well as the base plate, are made of ASTM A709 Gr. 50 steel with a minimum specified yield stress of 50 ksi (345 MPa) and an ultimate strength of 65 ksi (448 MPa). The shafts are connected to each other by steel I-shaped shear links along the height of the tower by a saddle at the top and by steel vertical shear plates at the base. For more information on the tower, see Astaneh-Asl and Qian [1]. Figure 3 shows a plan view of a quarter of the base plate with the locations of 3-in. (75 mm) and 4-in. (100 mm) diameter ASTM A354 BD hot-dip galvanized anchor rods, 6-in. diameter ASTM A633 shear dowels, and the anchorage plates. The rods are made of SAE 4140 steel with a minimum yield strength of 115 ksi (793 MPa) and a minimum ultimate strength of 140 ksi (965 MPa) [3]. The base plate of the tower is made of 14 separate plates, as shown in Figure 3(b). Figure 4 shows the

typical details of the connection of the tower shafts to the base plate and anchorage of the tower base to the pile cap by anchor rods.

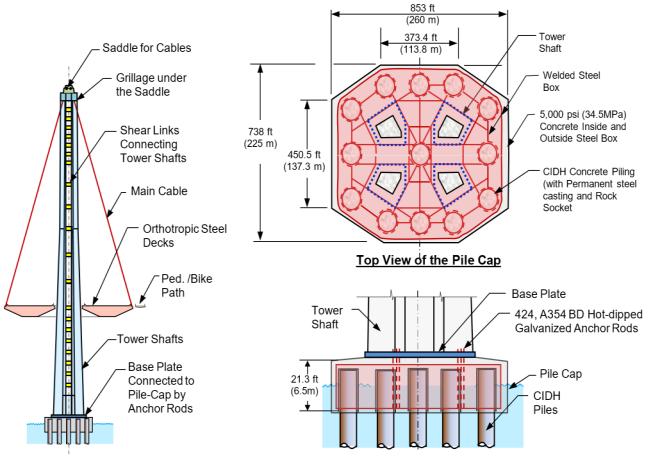

Figure 2. Elevation of the Tower (left) and Plan and Elevation of the Pile Cap Footing Supporting the Tower

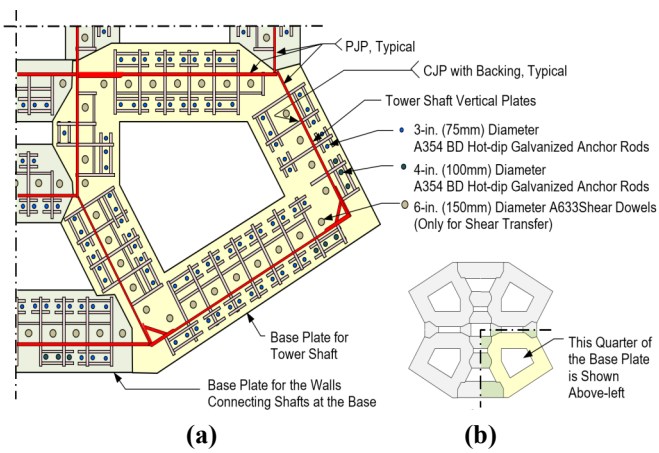

Figure 3. Plan of the Base Plate and Location of Anchor Rods

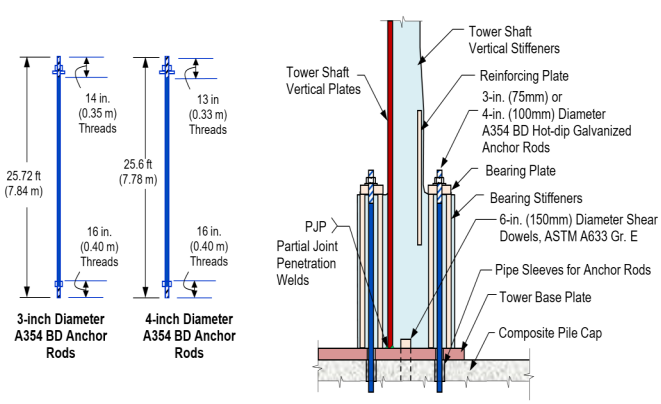

Figure 4. Anchor Rods and Details of Tower Anchorage to the Pile Cap

Investigation of the Fracture of the A354 BD Anchor Rods in the SAS Bay Bridge

The use of A354 BD hot-dip galvanized anchor rods in this important bridge created a serious, undesirable behavior. In 2013, and a few months before the opening of the bridge, 32 of the 96 anchor rods connecting the seismic shear keys to the top of Pier E2 on the east end of the SAS Bay Bridge fractured when tightened (refer to Figure 1 for location).

In 2015, Nader (of the TYLI/Moffitt Joint Venture) [4-5], the Chief Engineer and Engineer of Record for the SAS Bay Bridge, presented an analysis of the bridge subjected to a selected number of ground motions. He concluded that even without any anchor rods, the response of the bridge to six ground motion records (that the bridge design team had considered in the design of the bridge) will be almost the same as the response with all anchor rods present. A critical review of the validity of this claim as well as the correctness of the analysis is not possible at this time since Nader did not provide much information on the analysis itself. However, the bridge model that the bridge design team used did not seem to include local buckling of the tower shaft plates, and fracture of the partial joint penetration (PJP) welds that connect the base of the tower to the base plate (see again Figure 4).

The performance criteria established for this "lifeline" bridge by Caltrans [6] state that, "The bridge shall have a clearly defined inelastic mechanism for response to lateral loads and inelastic behavior shall be restricted to piers, tower shear links, and hinge beam fuses." According to this statement in the performance criteria [6] for the bridge and publications by the bridge design team [7-8], local buckling, yielding, or fracture of any other element of the tower, including plates, bolts, anchor rods, and welds, is not allowed. To assess whether the performance criteria can be fulfilled with fractured anchor rods, this paper provides a summary of the results of a realistic pushover analysis of the tower of the SAS Bay Bridge without anchor rods connecting the tower to the pile cap. Moreover, if the pushover behavior is not acceptable, a measure of retrofit is suggested that can prevent premature failure of the tower during future seismic events.

Objective

The main objective of the research summarized in this paper was to investigate pushover behavior of the main tower of the new SAS Bay Bridge with no anchor rods connecting the base of the tower to the top of the pile cap.

In 2013, it was discovered that two out of the 424 anchor rods connecting the tower to the pile cap were fractured. The cause of fracture was the hydrogen embrittlement of the A354 BD anchor rods. Since all 424 anchor rods were hydrogen embrittled [9-10], it is likely that more anchor rods would fracture during the service life of the bridge. The fracture of the remaining anchor rods due to hydrogen embrittlement is the reason why this study was undertaken in order to find out what would happen to the bridge tower during future major seismic events without any anchor rods.

Realistic Pushover Analysis of the Tower with No Anchor Rods at the Base

The remainder of the paper focuses on the realistic pushover analysis of the tower of the SAS Bay Bridge in the transverse direction (most critical) with no anchor rods connecting the tower base plate to the pile cap.

Finite Element Modeling

ANSYS Workbench finite element nonlinear software was used to simulate the behavior of the main tower, base plate, and pile cap supporting the tower. All anchor rods were assumed to have fractured and they were not included in the model. Proper gap elements were used to allow uplifting of the base plate (see Figure 5).

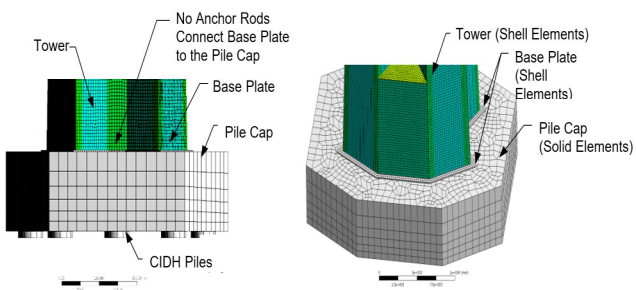

Figure 5. Finite Element Model of the SAS Bay Bridge Tower, Base Plate, and Pile Cap

The detailed model of the base plate and pile cap was added to be able to investigate the effects of failure modes associated with the connection of the tower to the base plate, the base plate, and the pile cap, while there were no anchor rods present. Two types of steel were used in the modeling of the tower structure. Almost all components of the main tower and the tower base plate were ASTM A709 Gr. 50 with a minimum specified yield stress of 50 ksi (345 MPa). The connection plates of the shear links to the tower shafts were modeled with Gr. 70 steel with a minimum specified yield stress of 70 ksi (485 MPa). A bi-linear kinematic hardening model was considered for the steel with an elastic modulus of 29,000 ksi (200 GPa), a Poisson ratio of 0.3, and a strain hardening ratio of 1%. The concrete used in this analysis to model the pile cap and the piles had an elastic modulus of 4350 ksi (30 GPa), a Poisson ratio of 0.18, and a compressive strength of f'_c=5.073 ksi (35 MPa), which was obtained from the construction drawings [2] as the specified values. The concrete inside the steel box was modeled as confined concrete. More detailed information on modeling of the tower itself can be found in the study by Astaneh-Asl and Qian [1]. After applying the gravity force to the tower, incremental horizontal displacements were applied to the cable saddle groove location under the ANSYS displacement controlled iteration algorithm [11].

Results of the Pushover Analysis of the SAS Bay Bridge Tower with No Anchor Rods

Figure 6 shows the pushover curve of the tower in the transverse direction regarding horizontal force on the vertical axis versus applied horizontal displacement of the cable saddle on top of the tower on the horizontal axis. As the figure shows, the tower does not have a clear yield plateau, which would be a desirable characteristic of structures in resisting seismic effects. The tower behaves elastically from origin to the point of "initial yielding" (see Figure 6) and continues to yield more elements until it reaches the defined "yield point" at point Y. In large structures, due to local yielding of very small areas, the pushover curve starts deviating from the initial elastic stiffness line very early, see point Y in Figure 6. This point cannot be considered the yield point, since the structure is essentially elastic. For these cases, a yield point was defined where the pushover curve deviates from the initial elastic line, a horizontal distance equal to 10% of the horizontal elastic deformation [1].

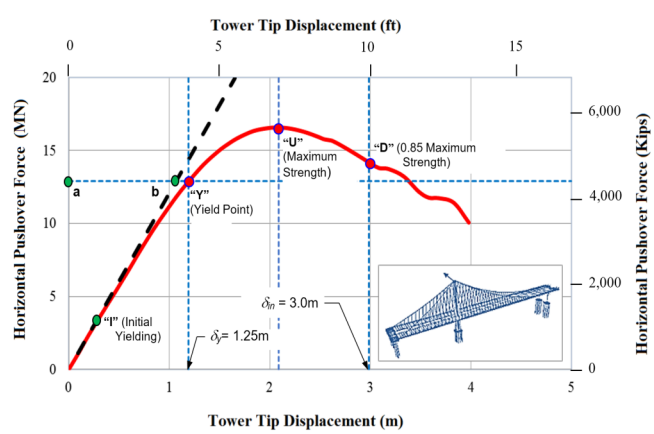

Figure 6. Transverse Pushover Curve When There Are No Anchor Rods at the Base

As pushover continued beyond the yield point, point Y in Figure 6, the tower continued to accept larger forces due to strain hardening, while the stiffness continued to decrease due to further yielding. During the pushover, the shear links yielded first then, as pushover continued, yielding of the shear links continued, but the base of the tower started uplifting on the tension side and yielding on the compression side of the base plate. As the tower reached its maximum strength at point U (see Figure 6), significant yielding and local buckling of the compression side of the base of the tower had already occurred. Point D on the pushover curve in Figure 6 is an important point related to the behavior, since it represents the point where the ductility of the system is measured. For a relatively large structural system such as the SAS Bay Bridge tower, the ductility is defined as the ratio of the displacement at a point where the strength is 85% of the maximum strength (δ_{in} in Figure 6) and the displacement at the yield point (δ_y in Figure 6). Figure 6 further shows that δ_{in} and δ_y were 9.8 ft (3.0m) and 4.1ft (1.25m), respectively. Therefore, the pushover ductility of the tower was 9.8/4.1 = 2.5.

Performance of the Main Elements of the Tower during the Pushover

In this section, the authors present the results of the behavior of the main elements of the tower during pushover, when all anchor rods were assumed to have fractured due to a combination of hydrogen embrittlement and seismic forces.

Tower Behavior under Pushover:
Figure 7 shows the equivalent von Mises stresses in the tower at points Y, U, and D during the pushover in the transverse direction. Red represents yielding in the shell elements, or plates. In this case, yielding is defined as equivalent von Mises stress reaching the specified minimum yield stress of the steel plates, 50 ksi (345 MPa), for all steel plates including the shear links, and 70 ksi (483 MPa) for the end connection plates of the shear links to the tower shafts. The points Y, U, and D correspond to the same points as in Figure 6; that is, yield, maximum strength, and 0.85 maximum strength points on the pushover curve.

At yield point, Figure 7(a) shows two out of seven pairs of shear links at the top portion of the tower yield, while the other parts mainly remain elastic. High stresses are generated on the compression side of the tower in the middle portion and at the base of the tower. At the point of maximum strength, point U in Figure 6, shear links in the upper part, as well as in the middle part of the tower have yielded in shear, as shown in Figure 7(b). There is also yielding and some local buckling in the compression side of the tower in the middle portion. However, the compression side of the tower at the base shows severe yielding and local buckling. After reaching the maximum strength, pushover strength of the tower drops relatively quickly, due to local buckling in several areas of the tower base and corner stiffeners. At the point where the applied force has dropped to 85% of the maximum strength, point D in Figure 6, and where ductility is measured, more yielding of the shear links at the top and middle portions of the tower occurs, as shown in Figure 7 (c). Moreover, the base of the tower shows widespread yielding and severe local buckling on the compression side.

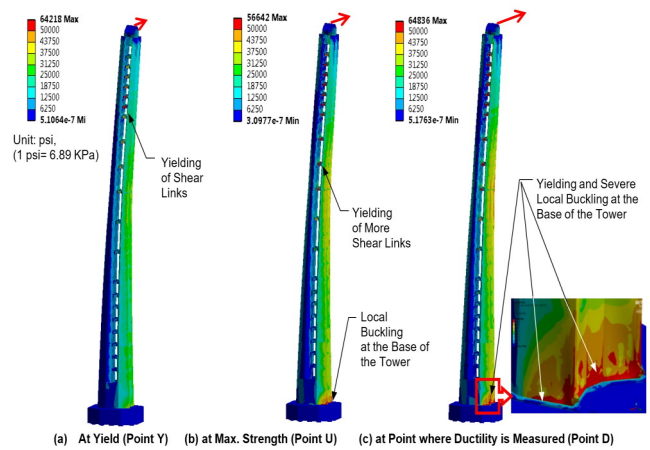

Figure 7. Equivalent (von Mises) Stresses at the Yield Point, Maximum Strength, and 85% Maximum Strength Points for Transverse Pushover of Tower

The Behavior of PJP Welds Connecting the Tower to the Base Plate:
Figure 4 shows partial joint penetration welds connect the tower legs to the base plates. Notice that when anchor rods are present and tightened to the specified amount of pretensioning (i.e., 70% of their tensile strength), the base of the tower and the entire area of the base plate are compressed down on top of the pile cap. The tower pressing on the base plate results in the PJP welds connecting the base of the tower shafts to the base plate to be in compression. However, when there are no anchor rods in place, or if the anchor rods are not tightened to 70% of their tensile strength, during the pushover, part of the base plate can uplift, resulting in subjecting the PJP welds to tension. Therefore, it is important to determine if the welds connecting the tower's vertical plates to the base plate have the strength to transfer the tensile uplift stresses from the vertical plates of the tower to the base plate.

The pushover analysis indicated that, when the pushover horizontal displacement reaches 7.6 ft (2.34m), the PJP welds at the base of the tower will fracture. Obviously, this

is unacceptable performance for a lifeline bridge in which, according to its performance criteria, the only damage allowed in the tower is the ductile shear yielding of the shear links, while no fracture of welds is allowed.

Figure 8(a) shows the equivalent von Mises stresses on the bottom surface of the tower base plate when the tower reaches its maximum strength (i.e., point U in Figure 6). At this point, some areas of the base plate have yielded. Such yielding of the base plate during the pushover is in violation of the performance criteria for this bridge, which allow only yielding of the shear links, while the rest of the tower remains elastic. Figure 8(b) shows the vertical pressures that the bottom surface of the base plate exert on the top of the pile cap at point U during the pushover, when the tower, without anchor rods, reaches its maximum strength during the pushover. Since the concrete under the base plate is confined, the maximum compression strength on it can reach $1.7f'c$, where f'_c is the specified compressive strength of the concrete measured using cylinder specimens. Therefore, in Figure 8, red corresponds to the locations with pressure on the concrete exceeding $1.7f'_c$, which indicates compressive crushing of concrete under the base plate.

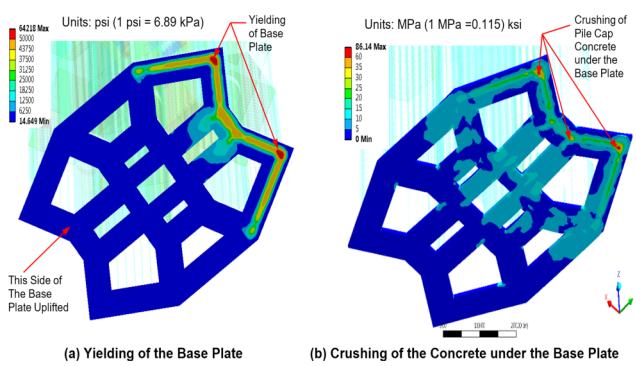

Figure 8. Equivalent (von Mises) Stresses at Two Locations: (a) the Bottom Surface of the Base Plate and (b) the Top Surface of the Pile Cap

Comparison of Tower Behavior with and without Anchor Rods

Figure 9 shows a comparison of the pushover behavior of the tower with and without anchor rods connecting it to the pile cap. The curve for the tower pushover with the anchor rods is extracted from the work done previously by Astaneh-Asl and Qian [1]. On the curve for the tower with the anchor rods, points Y, U, and D correspond to points of yield, maximum strength, and 85% of maximum strength (i.e., the point where ductility is measured). Points Y', U', and D' are similar points on the pushover curve for the tower without any anchor rods. The initial elastic stiffness for both curves was almost identical, which means, before significant yielding, under dynamic loading during the earthquakes, the tower with or without anchor rods connecting it to the pile cap will be subjected to almost the same seismic inertia forces. However, comparing force at points Y and Y', the tower without the anchor rods will yield the shear links at about 70% of the force that will yield the tower with the anchor rods.

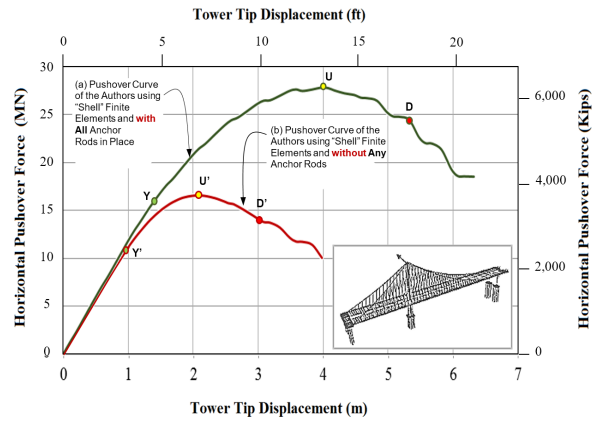

Figure 9. Comparison of Pushover Curves of the Tower with and without Anchor Rods

As for the maximum strength, comparing points U and U', the tower without the anchor rods reaches its maximum and drops the load at about 63% of what the tower with anchor rods could take. To compare ductility of these two cases of the tower with and without anchor rods, the ratio of displacements at D and Y to the ratio of displacements at D' and Y' should be compared. This process indicated that ductility of the tower without the anchor rods was reduced to 2.5 compared to 3.2, which is the ductility of the tower with the anchor rods.

Suggested Retrofit to Mitigate the Hazard Posed by Brittle Tower Anchor Rods

The problem of SAS Bay Bridge anchor rods is directly related to the following aspects:

(a) The design decision to use ASTM A354 BD hot-dip galvanized anchor rods in a very corrosive offshore environment.
(b) The failure during construction in leaving the anchor rods in the open environment unprotected for more than two years.
(c) Embedding the anchor rods in the pile cap concrete inside sleeves and not filling the sleeves with grout. The lack of protective grout resulted in the seawater seeping into the pile cap to collect around the anchor rods and caused further stress corrosion in them.

In this paper, the authors show that not having the anchor rods resulted in the undesirable behavior of the main tower. To mitigate the problem, the following summary of retrofit measures is proposed.

1. The tower needed to be retrofitted to prevent yielding and local buckling of the tower legs. The issue of the local buckling of the tower legs is also an issue even when anchor rods have no problem [1]. Hence, the vertical stiffeners inside the tower legs needed to be strengthened by adding stiffening material to them [1]. The satisfactory performance of such stiffeners was established by Qian and Astaneh-Asl [12].
2. The partial joint penetration (PJP) welds connecting the tower legs to the base plate needed to be strengthened to develop the yield strength of the tower leg plates.
3. Many of the 3-in. (7.6 cm) diameter unacceptable brittle A354 BD anchor rods that were not above the piles should have been replaced, albeit at a very high cost, with 3.5-in. (8.9 cm) ductile "upset" A354 BC anchor rods. To do so would have required boring through the existing anchor rods through the entire 19.7 ft (6m) depth of the composite pile cap, then attaching a steel reaction frame to the bottom of the pile cap, and finally installing the new A354 BC upset anchor rods connecting the tower base plate to the new steel structure at the bottom of the pile cap.
4. Water-sealed caisson around the pile cap needed to be constructed to prevent seawater from reaching pile cap. The seawater caused not only corrosion of the anchor rods but also corrosion of the steel plate box of the composite pile cap. This latter problem is not part of this paper but also needs to be solved. So, this retrofit step could have protected the pile cap as well.

Summary of the Anchor Rod Issue and Conclusions of the Pushover Analysis

In 2013, a few months before the SAS Bay Bridge was opened, 32 3-in. diameter A354 BD hot-dipped galvanized anchor rods connecting the shear keys on the east end of the bridge fractured after tightening. The cause of the fracture was established to be hydrogen embrittlement [9-10]. Bridge specifications did not recommend the use of A354 BD high-strength anchor rods and bolts, and specifically prohibited hot-dip galvanizing them because of the possibility of hydrogen embrittlement, as happened in this bridge. The fracture of the 32 anchor rods in the shear keys after tightening, and then fracture of at least one anchor rod at the base of the tower, which was not even fully tightened, created a serious concern about the safety of the bridge [13]. In addition to hydrogen embrittlement of the anchor rods, when one of the anchor rods at the base of the tower also failed because of thread stripping, the safety of the entire bridge came under question. More than 2200 A354 BD hot-dip galvanized bolts and anchor rods were used in the most critical connections of the bridge superstructure. In particular, the single tower of the bridge was anchored to its pile cap support by 424 A354BD hot-dip galvanized anchor rods. These are the anchor rods that had the problem of hydrogen embrittlement and thread stripping.

After fracture of the first anchor at the base of the tower, the transportation officials in charge of the bridge initiated an investigation of the case to establish the cause and to develop a repair and retrofit strategy. As the investigation continued, it became apparent that the cause of fracture of the anchor rod at the base of the tower was hydrogen embrittlement, exacerbated by the presence of the salty ocean water inside the pipe sleeves around the anchor rods, which, in many cases, were not filled with grout, as specified in the drawings. The fact that the threads on the anchor rods were also suspect to stripping made it very likely that, in the long-term, the anchor rods at the base of the tower would have been susceptible to fracture during or even before a major earthquake. Since the bottom ends of the anchor rods were embedded in the pile cap, removal of the existing brittle anchor rods and replacing them with sound anchor rods was almost impossible and cost prohibitive. In 2015, the bridge design team in a presentation to the Toll Bridge Program Oversight Committee (TBPOC) provided results of their analysis. They concluded that the anchor rods at the base of the tower were not needed, and the seismic performance of the bridge with or without anchor rods at the base of the tower would be almost the same during major earthquakes. They only recommended some limited repair, maintenance, and monitoring activities for the anchor rods and leaving the anchor rods in their places.

The main objective of this current investigation was to establish the pushover behavior of the tower without the anchor rods connecting it to the pile cap. Also, the two pushover curves with and without anchor rods were compared. In the model used in this study, and summarized previously by Astaneh-Asl and Qian [1], all plates in the shafts were modeled as inelastic shell elements capable of yielding and buckling.

Based on the results of realistic pushover of the SAS Bay Bridge tower, using shell elements for the plates, the following observation were made and conclusions reached.

1. This study showed that the pushover strength and ductility of the tower without anchor rods connecting

it to the pile cap was only about 60% and 80% of that for the case with the anchor rods, respectively.

2. There was a need for seismic retrofit of the tower itself and its base anchored to the pile cap by removing the brittle A354 BD hot-dip galvanized anchor rods. Retrofit plans were proposed, which, if implemented, could mitigate the problems and bring the performance of this bridge to the level of a lifeline bridge, and satisfy the corresponding performance criteria. The lifeline performance is for the bridge to open to traffic almost immediately after a major earthquake, with limited damage in specifically designated areas.

Lessons Learned and How This Problem Could Have Been Avoided

Following is a list of important lessons learned from this case study, which also applies to the design and construction of other structures with similar details.

(a) As many bridge design codes recommend, the A354 BD high-strength anchor rods should not have been used in this structure in the corrosive environment over seawater, where the anchor rods are embedded in the pile cap and the pile cap is submerged in seawater.

(b) The A354 BD anchor rods and bolts should not have been hot-dip galvanized, which is well-known to cause hydrogen embrittlement in high-strength steel. Instead, they should have been mechanically galvanized with zinc or aluminum, which is a very common procedure.

(c) The anchor rods should not have been left at the site in the open environment for more than three years to be exposed to the rain and seawater environment.

(d) The number of threads per inch and the depth of the thread should have been specified correctly to avoid thread stripping under tension.

(e) The anchor rods should not have been embedded in the concrete of the pile cap. Instead, the following solutions were recommended in this case. First: the anchor rods should have been passed through the pile cap with the bottom nut under the pile cap to ease replacement. Second: the anchor rods should have had a small segment at the top, weaker than the main body of the anchor rods, to ensure that the small portion at the top acts as a fuse and prevents damage to the main body of the anchor rod embedded in the concrete. The top segment could be replaced easily in case of corrosion during the service life or damage after a seismic event.

(f) Instead of using A354 BD high-strength anchor rods, not allowed to be hot-dip galvanized, upset A3254 BC anchor rods should have been used. The A354 BC has a specified minimum yield stress of 99 ksi (683 MPa) [3]. The A354 BC bolts can be galvanized either by hot-dip galvanizing, without developing hydrogen embrittlement, or by mechanical galvanizing.

(g) In regular straight anchor rods and bolts, threads are cut into the cross section of the shanks, resulting in the fracture of the under-thread area of the threaded part to be the tensile failure mode. This failure mode is quite brittle and is not desirable in high-seismic applications, where ductile failure modes need to govern. In upset bolts and anchor rods, the shank cross-sectional area is smaller than the under-thread area such that the yielding of the gross area of the shank is the governing failure mode instead of the fracture of the under-thread area. If instead of problematic 3-in. A354 BD bolts, A365 BC upset anchor rods had been used in this bridge, the diameter of the anchor rods (outside of the upset portion) would have been 3.5 inches (8.9 cm) instead of 3 inches (7.6 cm) for the anchor rods that were used. With this relatively small but very important design decision, there would have been no problem of hydrogen embrittlement and thread-stripping for bolts and anchor rods, as occurred in the new $6.5 billion SAS Bay Bridge.

Acknowledgements

This study was part of a larger project on Investigation of Seismic Performance of the New Self-Anchored Suspension Bay Bridge East Spans at the University of California Berkeley, USA, with Professor Abolhassan Astaneh-Asl as the Principal Investigator. The authors would like to express their sincere appreciation for the tremendous technical support provided by Ozen Engineering Inc. (https://www.ozeninc.com) on the use of the powerful ANSYS nonlinear structural analysis software featured in this project. The authors would like to acknowledge the input from material scientists Yun Chung and Lisa Fulton.

References

[1] Astaneh-Asl, A., & Qian, X. (2016). Pushover Analysis of the Tower of the New Self-Anchored Suspension Bay Bridge. *Proceedings of the 2016 IAJC-ISAM Joint International Conference.* Nov. 6-8, Orlando, Florida.

[2] Caltrans. (1999). Project Plans for Construction on State Highway in San Francisco County in San Francisco, *Engineering Drawings,* The State of California, Department of Transportation, Sacramento.

[3] ASTM (2011). Standard Specification for Quenched and Tempered Alloy Steel Bolts, Studs, and Other Externally Threaded Fasteners, *ASTM Standard A354-11,* American Society for Testing and Material.

[4] Tower Anchor Rod Workshop, *Two Day Meeting Summary*, June 16 & 17, 2015. Retrieved from http://www.baybridgeinfo.org/sites/default/files/pdf/FinalTBPOCPacket-24Sep15_0.pdf

[5] Nader, M. (2015). Analysis of Self-Anchored Suspension Bridge without Tower Anchor Bolts, Retrieved from http://www.baybridgeinfo.org/sites/default/files/pdf/Analysis-of-SAS-with-No-Tower-Anchor-Rods.pdf

[6] Caltrans. (2002). Self-Anchored Suspension Bridge-Design Criteria-100% Submittal, Prepared by T. Y. Lin International/Moffatt & Nichol Engineers, a Joint Venture, Retrieved from http://www.dot.ca.gov/baybridge/a354report/F1_Self-Anchored_Suspension_Bridge_Design_Criteria_100_percent_submittal.pdf

[7] Nader, M., Manzanarez, R., & Maroney, B. (2000). Seismic Design Strategy of the New East Bay Bridge Suspension Span. *Proceedings of the 12th World Conference on Earthquake Engineering*. Auckland, New Zealand.

[8] Nader, M., Lopez-Jara, J., & Mibelli, C. (2002). Seismic Design of the New San Francisco-Oakland Bay Bridge Self-Anchored Suspension Span. *Proceedings of the 3rd Nat. Seismic Conf. and Workshop on Bridges and Highways,* Portland, Oregon.

[9] Chung, Y. (2014). Corrosion on the New Eastern Span of the San Francisco-Oakland Bay Bridge, Material Performance. *NACE International*, *P53*, *11*, 58.

[10] Chung, Y., & Thomas, L. K. (2014). High Strength Steel Anchor Rod Problems on the New Bay Bridge, Rev 1. *Report to Committee on Transportation and Housing California State Senate, Sacramento, 105pp*. Retrieved from http://media.sacbee.com/smedia/2013/12/07/21/47/Djfhs.So.4.pdf

[11] ANSYS, Inc. (2013). *ANSYS Mechanical APDL Theory Reference, Release 15*. ANSYS Inc., Canonsburg, PA.

[12] Qian, X., & Astaneh-Asl, A. (2016). Behaviour and Seismic Design of Stiffeners for Steel Bridge Tower Legs and Piers. *Proceedings of the World Congress on Civil, Structural, and Env. Engineering (CSEE'16)*, Prague, Czech Republic.

[13] Martin, G. (2013). Bridge Over Troubled Bolts: Cal Experts Question Whether New Bridge is Safe. *California Magazine.* Retrieved from http://alumni.berkeley.edu/california-magazine/just-in/2016-06-20/bridge-over-troubled-bolts-cal-experts-question-whether-new

Biographies

ABOLHASSAN ASTANEH-ASL is a professor in the Department of Civil and Environmental Engineering at the University of California, Berkeley. He has over 48 years of experience in design, research, and teaching courses in structural and earthquake engineering and design of buildings, bridges, and other structures, as well as blast protection of structures. He has testified as an expert before the policy making and judicial bodies, has completed more than 50 major research projects, and has published more than 300 technical papers. Dr. Astaneh-Asl may be reached at Astaneh@berkeley.edu

MARYAM TABBAKHHA is currently a visiting assistant project scientist in the Department of Civil and Environmental Engineering at the University of California, Berkeley. She earned her BS degree from the University of Science and Technology (Iran) and two master's degrees in Earthquake Engineering and Geotechnical Engineering from Sharif University (Iran) and Ecole Nationale des Ponts et Chaussees (France). She earned her PhD from Ecole Centrale Paris and worked as a postdoc at Columbia University for one year. Her research interests include masonry structure, steel moment frame, the effect of the flood on structures, earthquake engineering. and probabilistic theory and uncertainty quantification. Ms. Tabbakhha may be reached at tabbakhha@berkeley.edu

XIN QIAN is currently a PhD candidate at the University of California at Berkeley. She earned her BS degree at the Hong Kong Polytechnic University and MS in Civil Engineering from the University of California, Berkeley. Her research interests include steel and composite structures and earthquake engineering. She is the recipient of the first Professor T. Y. Lin Fellowship in Structural Engineering at UC Berkeley, and is active in student activities in earthquake engineering as the President of the EERI Berkeley student chapter. Ms. Qian may be reached at cindyqian@berkeley.edu

GEOMETRICAL DETERMINATION OF MAXIMUM POWER POINT OF A PHOTOVOLTAIC CELL

Mehmet Goksu, Millersville University of Pennsylvania; Faruk Yildiz, Sam Houston State University

Abstract

Renewable energy is one of the most important topics in energy production today, due to increasing world energy needs and global warming. An increased use of photovoltaic (PV) cells is essential for meeting this need, since sunlight is clean, abundant, and effectively limitless. In this paper, the authors present a new algorithm for determining the maximum power point (MPP) of a PV cell, based on the geometry of a current-voltage (I-V) curve. Even though a PV cell may be operated at any point on the I-V curve, the MPP indicates a point where the maximum power output is obtained from the cell. It is, therefore, necessary to accurately determine the MPP of the cells. This method also shows that geometrical construction of the MPP is independent of the characteristic of PV cells.

Introduction

It is clear that fossil fuel resources are finite, and depletion will happen sooner or later. If the current level of fossil fuel energy consumption continues, the entire world's fossil fuel energy reserve will be depleted in about 100 years [1]. Fossil fuel resources will eventually be replaced by renewable energy sources, especially by solar energy. Currently, only a small portion of the world's energy consumption is produced by renewable energy. There is an increasing demand for clean, renewable energy as the world's fossil fuel reserves continue to diminish. Scientists and engineers are trying to make renewable energy a more viable and cost-effective method of generating electricity in an effort to partially fulfill the world's energy needs.

I-V and power-versus-voltage (P-V) characteristics of PV cells have been studied extensively over the last decade. Some simulations of PV cells have been made primarily to develop an algorithm to determine precisely the location of the MPP while it is operating. The location of the MPP continually changes as the environmental conditions of the PV cell changes. To extract maximum power from a PV cell in any weather condition, an MPP controller is used in the system. An MPP controller is a device that uses either a logical or mathematical algorithm in order to operate the PV cell at the maximum efficiency under varying weather condition and loads. There are many MPP controller algorithms reported in the literature [2-5]. These algorithms vary in control strategies, variables, and hardware implementation. Each algorithm has its own unique property, with advantages and disadvantages with respect to these parameters [6-10].

The perturb-and-observe (P&O) and incremental conductance (INC) algorithms are the most widely used methods in MPP controllers. A P&O algorithm periodically compares power at different steps by perturbing voltage and current. This process continues until the MPP is reached. Even though this algorithm is one of the simplest to implement, a P&O algorithm suffers from slow dynamic response [11] and oscillation around the MPP, due to loss in power [12] in rapidly changing weather conditions. An INC algorithm uses the conductance of the P-V curve [13]. Similarly, this algorithm compares the instantaneous conductance and the perturbed conductance. Comparison between these conductance values is used to determine the location of the MPP. To improve the response time reaching the MPP, an INC algorithm in the perturbation uses variable step size instead of a fixed step for tracking the MPP [14].

The MPP algorithms used to determine the location of the MPP require some physical parameters related to the PV cells. Also, some algorithms use higher levels of computational analysis. This present study explains a new and simple method to determine the location of the MPP on the I-V curve. This method does not require any mathematical computation or knowledge about the PV cell. Kumar and Pachal [15] presented the geometrical prediction of the MPP by forming a parallelogram on the I-V characteristic curve. The method described in their work required different values of voltage and current on the I-V curve, including short-circuit current and open-circuit voltage, to construct the parallelogram.

After forming the parallelogram, the Lagrangian interpolation method was used to precisely determine the location of the MPP. Those authors presented their work in another study to predict the location of the MPP, based on quadratic regression analysis of the geometry on the P-V characteristic curve [16]. The new method proposed in this current study presents the geometrical location of the MPP in a very straightforward fashion without using any characteristics of the PV cell. With this method, the location of the MPP is

independent of the PV cell's characteristics. It is also applicable to any type of PV cells in any environmental condition.

Theory

In this paper, the authors describe the geometrical location of the MPP on the I-V curve using the fact that the maximum of a function is obtained by setting the differential of the function to zero. Figure 1 shows the nonlinear I-V characteristic curve of a PV cell. The I-V curve represents the possible voltage and current operating points of the PV cell that depend mainly on solar insolation, temperature of the cell, and the partial shading condition. A PV cell produces maximum power only at a single point along the I-V curve at a specific condition. Also, the maximum power delivered by a PV cell is given by the largest rectangle fitting under the I-V curve.

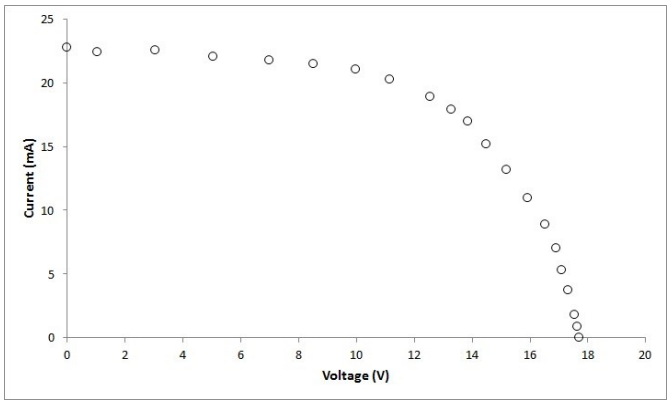

Figure 1. I-V Characteristic Curve of the PV Cell

Figure 2 shows a plot of the P-V characteristic of the cell with the I-V curve. The operating voltage and current at the MPP are called maximum power point voltage and current, respectively.

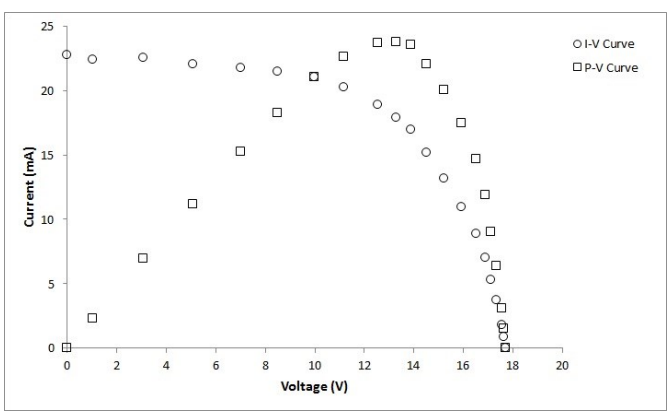

Figure 2. I-V and P-V Characteristic Curves

The MPP of a PV cell is usually located at the knee of the I-V curve, where the product of current and voltage is maximum. The condition for the maximum power yields that derivative of power with respect to voltage is zero, as given by Equation (1):

$$\frac{dP}{dV} = 0 \tag{1}$$

where, power is a function of voltage and current and is defined by Equation (2):

$$P = P(I,V) = I \cdot V \tag{2}$$

Differentiating both sides of the equation yields Equation (3):

$$\frac{dP}{dV} = I \cdot \frac{dV}{dV} + V \cdot \frac{dI}{dV} = I + V \cdot \frac{dI}{dV} = 0 \tag{3}$$

and rearranging the equation at the MPP yields Equation (4):

$$\left(\frac{I}{V}\right)_{mp} = -\left(\frac{dI}{dV}\right)_{mp} \tag{4}$$

The right-hand side of the equation represents the tangent to the MPP on the I-V curve. The left-hand side of the equation represents the slope of a line that connects the coordinate origin and the MPP. Figure 3 geometrically illustrates this relationship. From the geometrical construction, Equation 4 can be viewed in two different ways in order to describe the location of the MPP in the figure:

1. The MPP occurs on the knee of the I-V curve, where the I-V line and the I-V tangent both make the same angle, α, with the horizontal V-axis, as Figure 3 shows.
2. At the MPP, the tangent to the characteristic curve makes the same angle, β, with a vertical line to V_{mp} as the line connecting the origin and the MPP.

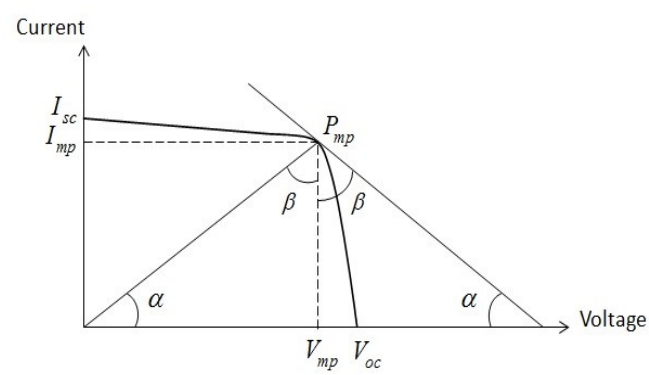

Figure 3. The Geometry of the MPP on the I-V Curve

In this paper, the authors present a new interpretation of Equation (1) that is different from all of the algorithms reported in the literature. The same mathematical condition was used in some MPP controller devices, such as INC, which compared the instantaneous conductance and the perturbed conductance. Other MPP controllers were based on the fact that the sign of derivative of power with respect to voltage changes from positive to negative when the operating point of a PV cell changes from the left-hand side of the MPP to the right-hand side of the MPP.

Analysis

The theory of the algorithm was tested using two different types of solar panels: a 5-watt multicrystalline solar panel from Clean Dependable Technology (CDT) and a 255-watt monocrystalline solar panel from Perlight Solar (PLM-255M-60). Table 1 shows the parameters of the panels from the manufacturers' data sheets. The 5-watt CDT panel was physically used in the laboratory to obtain the temperature and light intensity dependence of the I-V curves in order to test the algorithm described here. On the other hand, the 255-watt panel was tested using the I-V curves provided by the manufacturer [17].

Table 1. Specifications of the Solar Panels

Parameters	5-watt CDT Panel (Multicrystalline)	255-watt Perlight Panel (Monocrystalline)
I_{sc} (A)	0.32	9.05
V_{oc} (V)	21.01	37.20
P_{mp} (W)	5.18	255
I_{mp} (A)	0.31	8.17
V_{mp} (V)	16.68	31.20

Figure 4 shows the I-V characteristics of the 5-watt solar panel. The light intensities used in the experiments were 200.0 W/m^2, 400.0 W/m^2, 600.0 W/m^2, and 800.0 W/m^2 at a temperature of 22.0°C. A light sensor from Vernier Software & Technology (LS-BTA) was used to measure the light intensity in the experiment. Figure 5 represents the temperature dependence of the I-V curve. The 5-watt solar panel was tested at a fixed light intensity of 900.0 W/m^2 and temperatures of 14.0°C, 24.0°C, 46.7°C, and 54.0°C. An infrared thermometer (FLUKE 62-Max) was used to measure the temperature of the cell. It is important to emphasize that, as the temperature of the solar panel increased, the size of the energy gap between the conduction and valance bands decreased. This decrease in the energy gap allows the solar panel to absorb photons with longer wavelengths and lower energy. As a result, the short-circuit current of the solar panel increased. This is a signature of the semiconductors used in the PV cells. Due to the scaling of Figure 5, it is difficult to see the increase in the current.

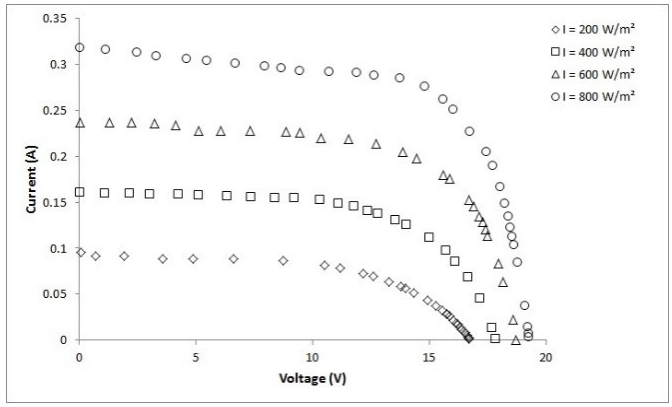

Figure 4. The Intensity Dependence of I-V the Curves

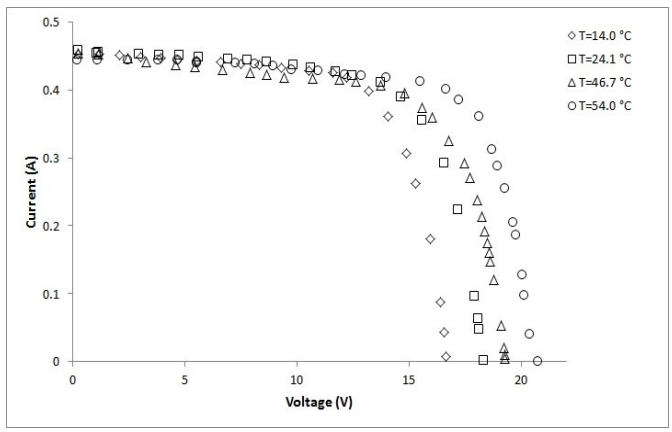

Figure 5. The Temperature Dependence of the I-V Curves

Tables 2 and 3 illustrate the average of experimental angle measurements, α and β, based on the algorithm. Each average in the tables represents the average of two angle measurements at a specified condition. The estimated uncertainty in the measurements is 0.2°. As the tables illustrate, the average angles are different for the same panel at different conditions. It is also true that angles might be different for different panels at the same condition of radiation intensity or temperature. However, the theoretical sum of angles α and β should be 90°. The sum is independent of any parameters, as long as angles are measured as described in the algorithm. The experimental sum of angles at different light intensities were (90.3 ± 0.4)° and (90.4 ± 0.5)° for the 5-watt CDT panel and 255-watt PML panel, respectively. Similar results were obtained at different temperatures: (89.7 ± 0.6)° for the 5-watt CDT panel and (90.3 ± 0.5)° for the 255-watt PML panel.

The experiment also revealed that the algorithm, described for determining the location of the MPP based on angle measurements, appeared to be independent of the type of solar panel. It should be valid for any PV cell.

Table 2. Angle Measurements at Different Intensities

Intensity (W/m^2)	5-watt Panel		Intensity (W/m^2)	255-watt Panel	
	α_{ave}(°)	β_{ave}(°)		α_{ave}(°)	β_{ave}(°)
200	12.2	78.6	200	8.2	82.6
400	21.2	69.2	400	15.8	74.8
600	24.8	65.4	600	23.2	67.6
800	28.2	62.6	800	29.0	61.4
			1000	35.2	54.2

Table 3. Angle Measurements at Different Temperatures

Temperature (°C)	5-watt Panel		Temperature (°C)	255-watt Panel	
	α_{ave} (°)	β_{ave}(°)		α_{ave}(°)	β_{ave}(°)
14.0	28.8	60.8	10	32.2	58.4
24.1	31.6	59.0	25	34.6	56.0
46.7	33.4	56.0	40	35.4	54.4
54.0	36.5	52.8	55	38.6	52.2
			70	40.0	49.8

Conclusion

In this study, the authors presented a new simple algorithm that explains the geometrical location of the MPP on the I-V curve. The proposed method was applied to two different kinds of solar panels under different light intensities and temperatures. The sum of angles in the algorithm is 90°. The experimental results clearly support the theory that this algorithm is applicable to any PV cell technology at any fixed environmental condition. The algorithm described in the paper could be easily implemented in any MPP controller device to operate the PV cell at the MPP under varying weather conditions.

Acknowledgments

The authors wish to acknowledge Dr. Michael Nolan for helpful conversations.

References

[1] US Energy Information Administration. (2015). *Annual energy outlook with projections to 2040*. Retrieved from http://www.eia.gov/outlooks/aeo/pdf/0383(2015).pdf

[2] Eltawil, M. A., & Zhao, A. (2013). MPPT techniques for photovoltaic applications. *Renewable and Sustainable Energy Reviews*, *25,* 793-813.

[3] Hussain, K. H., Muta, I., Hoshiono, T., & Osakada, M. (1995). Maximum photovoltaic power tracking: An algorithm for rapidly changing atmospheric condition. *IEEE Proceeding: Generation, Transmission, and Distribution*, *142*(1), 59-64.

[4] Casadei, D., Grandi, G., & Rossi, C. (2006). Single-Phase-stage photovoltaic generation system based on a ripple correlation control maximum power point tracking. *IEEE Transactions on Energy Conversion*, *21*(2), 562-568.

[5] Bhatnagar, P., & Nema, R. K. (2013). Maximum power point tracking control techniques: State-of-the-art in photovoltaic applications. *Renewable and Sustainable Energy Reviews*, *22,* 224-241.

[6] Esram, T., & Chapman, P. L. (2007). Comparison of Photovoltaic Array Maximum Power Point Tracking Techniques. *IEEE Transactions on Energy Conversion*, *22*(2), 439-449.

[7] Dolara, A., Faranda, R., & Leva, S. (2009). Energy comparison of seven MPPT techniques for PV systems. *Journal of Electromagnetic Analysis and Applications*, *1*(3), 152-162.

[8] Tofoli, F. L., Pereira, D. C., & Paula, W. J. (2013). Comparative study of maximum power point tracking techniques for photovoltaic systems. *International Journal of Photoenergy*, *2015,* 1-10.

[9] Bhatnagar, A. P., & Nema, B. R. K. (2013). Conventional and global maximum power point tracking techniques in photovoltaic application: A review. *Journal of Renewable and Sustainable Energy*, *5*(3), p032701-22.

[10] Subudhi, B., & Pradhan R. (2013). A comparative study of maximum power point tracking techniques for photovoltaic power systems. *IEEE Transactions on Sustainable Energy*, *4*(1), 89-98.

[11] Femia, N., Petrone, G., Spagnuolo, G., & Vitelli, M. (2005). Optimization of perturb and observe maximum power point tracking method. *IEEE Transactions on Power Electronics*, *20*(4), 963-973.

[12] Chung, H. S-K., Tse, K. K., Hui, S. Y., Mok, C. M., & Ho, M. T. (2003). A novel maximum power point tracking techniques for solar panels using a SEPIC or Cuk converter. *IEEE Transactions on Power Electronics*, *18*(3), 717-725.

[13] Koizumi, H., & Kurokawa, K. (2005). A novel maximum power point tracking method for PV module integrated converter. In *Proceedings of the IEEE Power Electronics Specialist Conference* (pp. 2081-2086), Recife, Brazil.

[14] Liu, F., Duan, S., Liu, F., Liu, B., & Kang, Y. (2008). A variable step size INC MPPT method for PV system. *IEEE Transactions on Industrial Electronics*, *55* (7), 2622-2628.

[15] Kumar, G., & Pachal A. K. (2014). Geometrical prediction of maximum power point for photovoltaics. *Applied Energy*, *119*, 237-245.

[16] Kumar, G., Trivedi, M. B., & Pachal A. K. (2015). Innovative and precise estimation using P-V curve geometry for photovoltaics. *Applied Energy*, *138*, 640-647.

[17] Perlight Solar. (n.d.). Retrieved from http://www.perlight.com/images/pdf/plm-m-60-series-spec-sheet.pdf

Biographies

MEHMET I. GOKSU is an associate professor of Physics at Millersville University of Pennsylvania. He is a condensed matter experimentalist with extensive experience in low-temperature physics. His research interests include quantum computing, physics education, and renewable energy. He has a strong interest in sustainability and energy-related issues are his passion. Dr. Goksu may be reached at mehmet.goksu@millersville.edu

FARUK YILDIZ is currently an associate professor of Engineering Technology at Sam Houston State University. His primary teaching areas are electronics, computer-aided design, and alternative energy technologies. His research interests include low-power energy harvesting, conversion, and storage, renewable energy education and technologies. Dr. Yildiz may be reached at fxy001@shsu.edu

SERVICEABILITY PERFORMANCE OF CONCRETE BEAMS REINFORCED WITH MMFX STEEL

Faris Malhas, Central Connecticut State University; Mustafa Mahamid, University of Illinois at Chicago;
Adeeb Rahman, University of Wisconsin-Milwaukee

Abstract

In this paper, the authors report on the serviceability performance of concrete beams reinforced with high-strength MMFX steel. The measured serviceability parameters were deflection, elastic stiffness, cracking moment, and crack width. The experimental program involved testing 22 13-ft beams with a 12x18-in. cross-section. Two classes of concrete strength were used: 6200 psi and 8700 psi. Three reinforcement ratios were used for each concrete class. For comparison purposes, Grade 60 steel was also used in two beams for each concrete strength. This experimental program to investigate MMFX steel was the first of its kind. The testing of these beams was performed using a monotonic static two-point loading to failure. Strain measurements in the middle portion of the beam were obtained using LVDTs with a gage length of about 20 inches. Mid-span deflection and crack widths were measured at all times and from both sides of the beam.

The experimental results showed that the beams exhibited more flexibility under service loads. The general behavior was similar to regular Grade 60 steel. The presence of half the steel as regular beams did not yield excessive deflection under service loads. The stiffness of the beams was significantly reduced after cracking and was more pronounced when compared to computed behavior of regular steel. However, deflection under service load for all specimens indicated that live load deflection would most probably satisfy the ACI Code, and at no time was it excessive. Also, crack widths under service load were reasonable and within normal ranges typically exhibited by concrete beam with 60 -ksi steel.

Introduction

The number of aging concrete structures has become significant. The corroding reinforcement and the durability of such structures makes it clear that alternative types of steel should be used to produce much more durable concrete structures. Much work in recent years has been focused on the critical issues associated with the durability of concrete. Reinforcement corrosion has emerged as the single most important factor impacting the durability of reinforced concrete. The corrosion of reinforcing steel leads to severe cracking of concrete and to serious structural damage. In many cases, corrosion of the reinforcement is so significant that the whole structure is rendered unusable and must be demolished. Normal reinforcing steel, such as ASTM A615, is protected from corrosion by the surrounding concrete and the PH level normally created by the concrete. Once the PH level is altered by the ingress of aggressive salts, such as chloride, the steel becomes vulnerable to corrosion. Most of the work in combating this phenomenon has historically focused on preventing or inhibiting the corrosion activities of the steel.

Until the advent of MMFX's steel technology, the corrosion problem was addressed by either treating steel materials with coatings, or by substituting standard steel with expensive alloy steels. Currently, epoxy-coated rebar is the reinforcing bar for the industry's primary method of reducing damage due to corrosion. Material costs for epoxy-coated rebars are significantly higher than standard black rebars. MMFX steel addresses the corrosion problem by essentially engineering the materials at the microstructure level for the intended performance, by reducing the vulnerability of steel to corrosion. MMFX steel provides high-strength steel as an effective solution to the corrosion problem. In this current study, the authors evaluated the experimental results of the overall flexural behavior of full-size concrete beams reinforced with MMFX steel. A comprehensive research project was conducted at the University of North Florida, sponsored by MMFX, to evaluate the ductility, the ultimate strength, and the serviceability of beams when using MMFX steel [1].

Research Significance

This experimental study was aimed at studying the behavior of concrete beam specimens for two different concrete strengths and three levels of reinforcement [2-4]. One objective of this experimental research project was to assess the flexural behavior of concrete beams reinforced with MMFX steel at service load, and compare the experimental results to the ACI requirements and provisions [5, 6]. To evaluate the performance of the beams at service load, the following parameters were measured or observed: moment curvature, stiffness reduction due to cracking, first crack formation, crack width, and deflection under service load. The second objective entailed a comparative analysis of experimental

results against analytical moment curvature. Finally, the investigation examined the validity of ACI provisions in predicting the service load deflection measured in the experimental results.

Concrete and Steel Mechanical Properties

The experimental program was designed to include two levels of strength, namely 5000 psi (mix A) and 8000 psi (mix B). Eight 6-in. diameter by 12-in. high cylinders were sampled from each concrete mix for a total of 16 cylinders. The compressive strength was determined at 3 days, 7 days, 14 days, 21 days, and 28 days. These cylinders were left next to the form during the curing period, and were exposed to the same identical temperature and humidity as the beams. For each concrete mix, three cylinders were tested at 28 days. The average 28-day compressive strength was 6200 and 8700 psi. Table 1 shows the results of compression tests of all 16 specimens. The 28-day strength is an average value of three cylinders for each mix.

Table 1. Concrete Strength

Cylinder age (days)	A- mix (psi)	B-mix (psi)
3	2650	4430
7	3750	6100
10	4460	6430
14	5430	7210
21	6050	8100
28	6200	8700

Figure 1 shows the experimental stress-strain diagram for the MMFX steel that was used in all of the computations of this project and which was obtained from the test results conducted by El-Hacha et al. [7]. Grade 60 steel was used for beams with regular reinforcement.

Experimental Program

Fabrication and Construction of the Beams

The forms and steel cages were all fabricated at the UNF campus. The plan was to transport the forms to Gainesville for concrete pouring and subsequent testing in the structural laboratory at the University of Florida. To simplify the transportation process and to save on the cost of materials in fabricating the forms, ¾-in. plywood was used to make three-cell boxes for three beams, as shown in Figure 2. Eight boxes were fabricated, six boxes with three cells and two boxes with two cells, for a total of 22 beam forms. The reinforcing steel cages posed a bit of a challenge, especially when dealing with #8 MMFX bars.

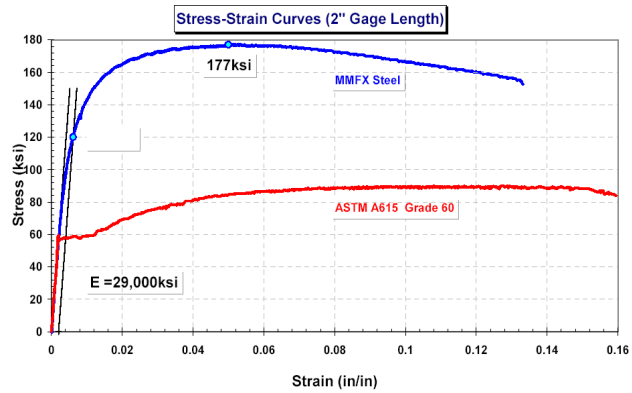

Figure 1. Stress-Strain Behavior of MMFX Steel [7]
Note. From "Fundamental Material Properties of MMFX Steel Bars," by El-Hacha, R., and Rizkalla, S. H., 2002, *Research Report RD02/04, North Carolina State University*, Constructed Facilities Laboratory, Raleigh, North Carolina. Reprinted with permission.

Figure 2. Steel Cages Placed in the Three-Cell Form

Strict quality control was observed during the entire process in order to eliminate any sources of error due to workmanship. The forms were then watered to saturation. The eleven A beams were first poured with 6200 psi concrete, followed by the B beams with 8700 psi concrete. The process was tremendously simplified because the trucks were able to come close to the form. Figure 3 shows how the truck chute was used to directly pour the concrete into the forms, and how the forms were then covered with burlap and dripping irrigation hoses were placed on top to allow for moist curing. The beams were left for 35 days under moist conditions.

Figure 3. The Finished Beams Covered with Burlap

Figure 4 shows how the beams were then stripped and transported to the laboratory.

Figure 4. The Cured Beams Stacked in the Laboratory

Test Setup, Instrumentation, and Data Collection

The testing program was carried out at the University of Florida's structural testing facilities. The laboratory has a strong floor with 50-kip tie-down anchor grid. Theoretical estimation of the failure load for the B1 beams indicated that the required maximum load would be about 130 to 150 kips. Therefore, it was decided that four tie-down points would be utilized to assemble a double frame with a cross beam, as shown in Figure 5. A 200-kip Enerpac double-acting actuator with a manual hand pump was used to apply the load.

Figure 5. Test Setup Showing the Loading Frame and Actuator

Schavetz LVDTs were used to measure the mid-span deflection, and to measure the strain at the top of the beam and at the level of reinforcement. The strain measurement was performed at both sides of the beam. Each beam had eight transducers attached to it, four from each side. The applied force was measured with a load cell below the actuator. The double readings allowed for verifying the reliability of the readings and to ensure that the measurements were captured, in case of transducer failure. The data were collected using a National Instrument's data acquisition system. Data logging was controlled using a LABVIEW module called Virtual Bench. The strain measurements were taken in the middle of the beam, where the moment is constant and maximum, and where the shear is zero. Figure 6 clearly shows the instrumentation of the test specimen.

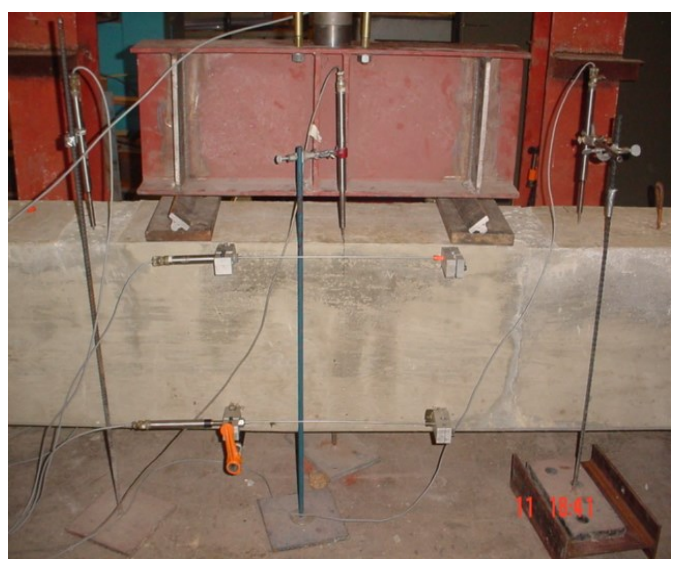

Figure 6. LVDTs Mounted to the Side of the Beam

Test Specimens

The basic experiment involved a 12-ft simple span rectangular beam with two-point loading, to create a pure bending zone in the middle. All beams were tested to failure. At the estimated service load, the loading was stopped and crack width measurements were conducted. Figure 7 shows how special attention was given to the basic loading arrangement.

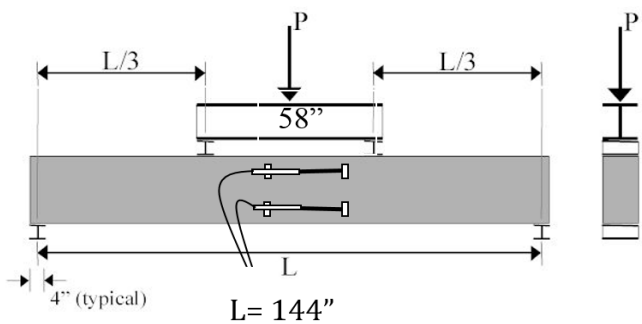

Figure 7. Testing Setup

Twenty-two beams were fabricated for the testing program. The typical cross-section of the beam was a 12-in. width and an 18-in. depth. Table 2 shows that two concrete strengths were used.

Table 2. Concrete Cylinder Strengths

BEAM DESIGNATION	f'_c
A SERIES	6200 PSI
B SERIES	8700 PSI

The MMFX steel has a yield strength in the vicinity of 120 ksi, which is twice that of the usual Grade 60 steel. In principal, the amount of steel required in design would be cut in half when using MMFX steel instead of Grade 60 steel. However, the minimum ductility is controlled by the combined effect of the strengths of both concrete and steel. The ACI maximum reinforcement ratio, based in minimum ductility [5], was used to select the amount of steel. The selection of the reinforcement to be used was based on a target compressive strength of 5000 and 8000 psi. However, compressive testing of cylinders taken from both batches yielded a higher compressive strength of 6200 and 8700 psi. These higher compressive strength values altered the correlation of the level of reinforcement with minimum ductility, but kept the selected reinforcement levels within an acceptable ductility range. Based on the two levels of concrete strength and an assumed yield stress of 120 ksi, three levels of reinforcement were selected to reflect a variation from high to low reinforcement. Tables 3 and 4 show the calculations that resulted in the following reinforcement areas.

Table 3. High, Medium, and Low Reinforcement Specimens

Target Concrete Strength (psi)	High Reinforcement Specimen			Medium Reinforcement Specimen			Low Reinforcement Specimen		
	ρ_{max} / A_s (in^2)/ Beam			1/2 ρ_{max} / A_s(in^2)/ Beam			1/4 ρ_{max} / A_s(in^2)/ Beam		
5000	0.00893	1.661	A1	.00447	0.831	A2	.00224	0.416	A3
8000	0.0116	2.16	B1	0.00581	1.080	B2	0.00291	0.540	B3

Table 4. Reinforcement Details for All Concrete Beam Specimens

BEAM	Bottom Steel	A_s	Top Steel	A'_s	Stirrups	f'_c
A1	2-#8	1.57	2-#4	0.39	#4@ 6 in	6200
A2	4-#4	0.78	2-#4	0.39	#4@ 6 in	6200
A3	2-#4	0.39	2-#4	0.39	#4@ 6 in	6200
B1	2-#8 + 2-#5	2.18	2-#4	0.39	#4@ 6 in	8700
B2	4-#5	1.23	2-#4	0.39	#4@ 6 in	8700
B3	2-#5	0.61	2-#4	0.39	#4@ 6 in	8700
CA2	2-#8+2#5	2.18	2-#4	0.39	#4@ 6 in	6200
CB2	2-#8	1.57	2-#4	0.39	#4@ 6 in	8700

Time restriction did not allow for trial batches within the concrete mix design, and the 28-day cylinder concrete strengths were measured to be higher than targeted. The new maximum reinforcement ratios and the actual ratios, as a fraction of the maximum, were:

For the A-Beam series: $\rho_{max} = 0.0102$
A1: with actual $\rho = 0.83\ \rho_{max}$
A2: with actual $\rho = 0.41\ \rho_{max}$
A3: with actual $\rho = 0.21\ \rho_{max}$

For the B-Beam series: $\rho_{max} = 0.0144$
B1: with actual $\rho = 0.81\ \rho_{max}$
B2: with actual $\rho = 0.46\ \rho_{max}$
B3: with actual $\rho = 0.23\ \rho_{max}$

However, the increase in concrete strength did not affect the significance of the original variations. The consequence was a slight decrease of all the reinforcement ratios relative to the maximum allowed by ACI.

Experimental Results

For the three levels of reinforcement that were used, the experimental results were compared to the analytical values that were obtained using the computer program Response2000 that utilizes section analysis based on the constitutive materials properties for both concrete and steel [8, 9]. This allowed for an accurate estimate of the deflection, based on actual curvature across the entire span. By carrying out these comparisons, a clear assessment can be made on the behavior of concrete beams with MMFX steel under service loads.

Analysis Results for Beam A1

Initial stiffness of beam A1 was difficult to measure exactly, but was rationally construed to correlate with the analysis. From the experimental plots for A1, the measured cracking moment was in the range of 13 to 18 ft-kips. The analysis showed the theoretical cracking moment to be about 18 ft-kips for all three models. The measured cracked stiffness averaged about 37×10^4 kips/ft, while the MMFX model resulted in a stiffness that was 30% higher. The computed cracked stiffness with the Grade 120 steel was 54% higher than the measured value from beam A1. As expected, the Grade 60 steel resulted in stiffness that was two and half times the measured value, due to the double amount of reinforcement. The service load deflection was satisfactory, as it fell within the acceptable limits of the ACI Code [5]. Table 5 summarizes the measured elastic structural response values of beam A1.

Table 5. Summary of Measured Elastic Structural Response Values for A1

Parameter	Experiment	MMFX Model	Grade 120	Grade 60
Initial Stiffness EI_g (ft-kips)	NA	231E4	231E4	231E4
Cracking Moment (ft-kips)	13.0 to18.0	18.0	18.0	18.0
Cracked Stiffness EI_{cr} (kip/ft)	37E4	48E4	57E4	96E4
Deflection at service load (inches)	0.63	NA	NA	NA
Crack width at service load (inches)	0.015 to .035	NA	NA---------	NA--------

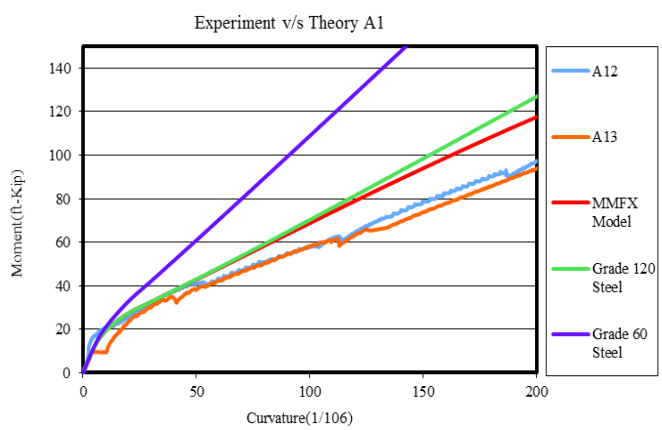

Figure 8. Experimental Moment-Curvature for A1, Compared to Three Analysis Models

Analysis Results for Beam A2

Comparing the measured initial flexural stiffness to the three analytical values, Figure 9 shows that the measured stiffness compared well with all three computed values. After cracking, the measured stiffness was reduced by about 90%. The MMFX model and the Grade 120 model cracked stiffness were reasonably close to the measured cracked stiffness. However, the Grade 60 analytical value was two and half times the measured stiffness. The measured ductility index of the A2 series average was 5.7. The three beams

exhibited a satisfactory level of ductility. Significant deformation preceded the failure of the beam, which was caused by concrete crushing. Pronounced yielding of the tension reinforcement was also observed. The ductility index was computed with reference to the computed yield moment of the Grade 120 model. The measured crack width of 0.01 inches at service load was considered within the acceptable range of values specified by ACI. Grade 60 and Grade 120 models yielded a failure moment within 7% of the measured value. Table 6 summarizes the measured elastic structural response values.

Table 6. Summary of Measured Elastic Structural Response Values for A2

Property	Experiment	MMFX Model	Grade 120	Grade 60
Initial Stiffness EI_g (ft-kips)	210E4	220E4	220E4	220E4
Cracking Moment (ft-kips)	18.0	22.0	22.0	22.0
Cracked Stiffness EI_{cr} (kip/ft)	23E4	31E4	31E4	55E4
Deflection at service Load (inches)	0.77	NA	NA	NA
Crack width at service load (inches)	0.01	NA	NA	NA

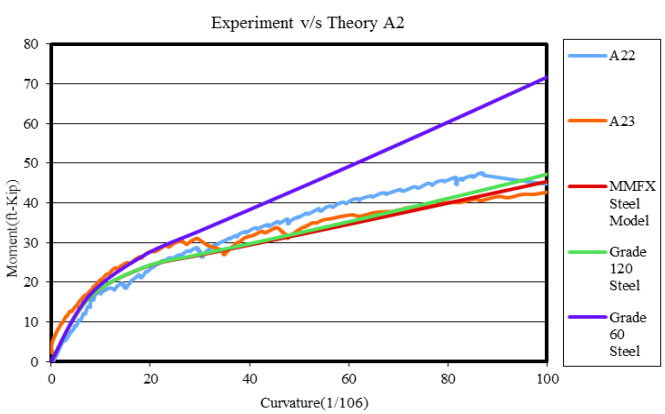

Figure 9. Experimental Moment Curvature for A2, Compared to Three Analysis models

Analysis Results for Beam A3

As shown in Figure 10, the initial flexural stiffness predicted by all models correlated to within 8% of recorded value. The measured cracked flexural stiffness was only 4% of the initial stiffness, which reflects a 96% loss of stiffness within the cracked zone. The MMFX model yielded a stiffness that was reasonably close to the measured value. However, the model with Grade 120 steel resulted in twice the stiffness. This difference was attributed to the gradual reduction in the elastic modulus for the MMFX steel. The analytical model with an equivalent amount of Grade 60 steel yielded a stiffness value three times the measured stiffness. Even though the amount of steel was only twice that of A3. The measured crack width under service load was about 0.025 inches, and exceeded the 0.016 inches specified in the ACI code, as a limit for normal exposure. Table 7 shows a summary of the measured structural properties for A3.

Table 7. Summary of Measured Structural Properties for A3

Property	Experiment	MMFX Model	Grade 120	Grade 60
Initial Stiffness EI_g (ft-kips)	240E4	220E4	220E4	220E4
Cracking Moment (ft-kips)	18.0	22.0	22.0	22.0
Cracked Stiffness EI_{cr} (kip/ft)	8E4	12E4	15E4	25E4
Deflection at service Load (inches)	0.66	NA	NA	NA
Crack width at service load (inches)	0.025	--------	---------	--------

Analysis Results for Beam B1

Figure 11 shows a measured initial stiffness of 287×10^4 ft-kips, which compared favorably to the computed values for all three analytical models. The same conclusion was observed with reference to the cracking moment, where the computed values overestimated the measured cracking mo-

ment by 10%. The measured average flexural stiffness after cracking correlated perfectly with the MMFX model. However, the Grade 120 model analysis resulted in a computed value of $75x10^4$ ft-kips, which was 20% over the measured value. The Grade 60 model yielded a computed cracked stiffness of $127x10^4$ ft-kips that was double the measured value.

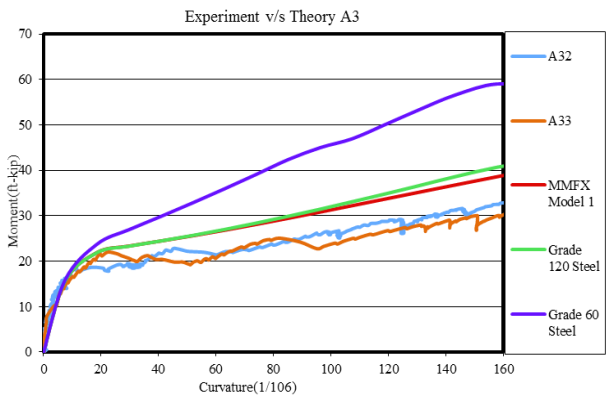

Figure 10. Experimental Moment Curvature for A3, Compared to Three Analysis Models

The deflection of the beam under service load was measured at 0.72 inches. Assuming 60% was due to a live load, this yielded a deflection due to a live load of about 0.432 inches, which was less than the maximum deflection allowed by ACI when using the limit L/360. Table 8 summarizes the measured elastic structural properties of beam B1.

Analysis Results for Beam B2

Figure 12 shows that the measured initial stiffness of beam B2 exhibited some softening that occurred prior to reaching the theoretical cracking load. This was attributed to loading and unloading B32 to 13 kips without logging the data. Therefore, the measured initial stiffness for B2 was not included in the analysis and, hence, it was not listed in Table 9. From the experimental plots for all B2s, the cracking moment was approximately 25 ft-kips. The analysis of the three models also indicated that the cracking moment was about 22 ft-kips. The measured cracked stiffness averaged about 25 ft-kips, while the MMFX model yielded a stiffness that was 28% higher. The computed cracked stiffness with the Grade 120 steel was about twice the measured value and the Grade 60, which yielded a cracked stiffness three times the measured value.

The deflection at service load was satisfactory and fell within the acceptable limits of the ACI Code. Table 8 summarizes the elastic structural response values of beam B2.

Table 8. Summary of Measured Structural Properties for B1

Parameter	Experiment	MMFX Model	Grade 120	Grade 60
Initial Stiffness EI_g (ft-kips)	287E4	267E4	267E4	267E4
Cracking Moment (ft-kips)	25.0	22.0	22.0	22.0
Cracked Stiffness EI_{cr} (ft-kips)	62E4	61E4	75E4	127E4
Deflection at service load (inches)	0.72	NA	NA	NA
Crack width at service load (inches)	.015 to .02	NA	NA	NA

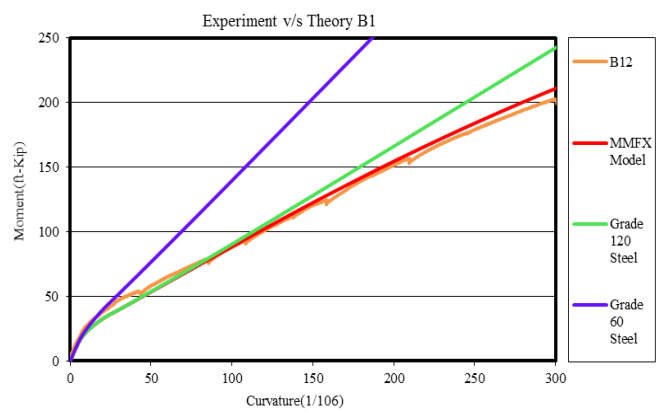

Figure 11. Experimental Moment Curvature for B1, Compared to Three Analysis Models

Analysis Results for Beam B3

Figure 13 shows that the measured initial stiffness for B3 was $248x10^4$ ft-kips. This value was almost a perfect match to the computed gross stiffness for all three models. For beam B3, the cracking moment was around 25 ft-kips. The analysis for all three models indicated that the cracking moment was about 22 ft-kips. The measured cracked stiffness averaged about $16x10^4$ ft-kips, while the MMFX model yielded a stiffness 18% higher than the measured value. The

computed cracked stiffness with the Grade 120 steel was 50% higher than the measured value, and the Grade 60 yielded a stiffness two and half times the measured value.

The deflection at service load was satisfactory and fell within the acceptable limits of the ACI Code. Table 10 summarizes the measured elastic structural response values of beam B3.

Table 9. Summary of Measured Structural Properties for B2

Parameter	Experiment	MMFX Model	Grade 120	Grade 60
Initial Stiffness EI_g (ft-kips)	------	253E4	253E4	253E4
Cracking Moment (ft-kips)	25.0	22.0	22.0	22.0
Cracked Stiffness EI_{cr} (ft-kips)	25E4	32E4	48E4	82E4
Deflection at service load (inches)	0.701	NA	NA	NA
Crack width at service load (inches)	.015 to .03	NA	NA	NA

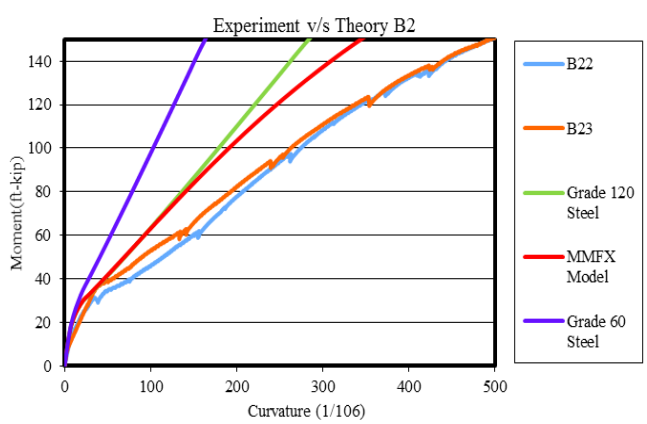

Figure 12. Experimental Moment Curvature for B2, Compared to Three Analysis Models

Table 10. Summary of Measured Structural Response Values for B3

Parameter	Experiment	MMFX Model	Grade 120	Grade 60
Initial Stiffness EI_g (ft-kips)	248E4	243E4	243E4	243E4
Cracking Moment (ft-kips)	25.0	22.0	22.0	22.0
Cracked Stiffness EI_{cr} (ft-kips)	16E4	19E4	24E4	43E4
Deflection at service load (inches)	0.54 to 0.82	NA	NA	NA
Crack width at service load (inches)	.01 to .03	NA	NA	NA

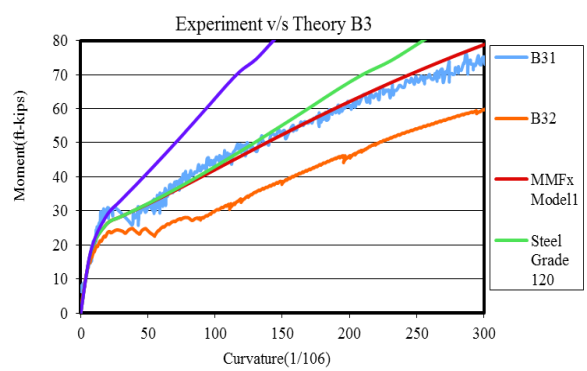

Figure 13. Experimental Moment Curvature for B3, Compared to Three Analysis Models

Conclusions

The primary goal of this experimental research project was aimed at assessing the overall flexural behavior of concrete beams reinforced with MMFX steel. The objectives of this paper were to report the results for the elastic composite behavior of these beams. The two levels of concrete strength sheds some light on the impact of the concrete strength on the beams' behavior. The reinforcement ratios

chosen for all MMFX beams were such that steel yielding was theoretically ensured. The conclusions that can be drawn from the experimental results are:

1. The stiffness of the MMFX beams was significantly reduced after cracking, and was shown to have a significant reduction when compared to computed results of regular steel beams.
2. Deflection under service load for all specimens indicated that live load deflection would most likely satisfy the ACI Code, and at no time was it excessive.
3. The measured values of crack width under service load for all tested beams were within the acceptable range.
4. The cracking moment of the MMFX beams can be accurately predicted using the ACI procedure.
5. The computer program RESPONSE2000 can be used with confidence to carry out further parametric studies.
6. The behavior of the different beam groups confirmed the consistency and reliability of the MMFX steel.

Comparison with control beams showed that, other than the reduced flexural stiffness, the MMFX beams were comparable in behavior to regular steel beams, and the replacement of regular steel with MMFX steel seems to be a viable alternative that would not compromise the structural serviceability and flexural characteristics of the beams.

Acknowledgement

The authors would like to thank Dr. Salem Faza of MMFX for the financial support to fund this research project, and to Dr. Ronald Cook of the University of Florida for providing their structural laboratory to carry out the testing.

References

[1] Malhas, F. (2002). Preliminary experimental investigation of the flexural behavior of reinforced concrete beams using MMFX steel. University of North Florida, report # 904311021.

[2] Hongestad, E. (1951). A Study of Combined Bending and Axial Load in Reinforced Concrete Members. Bulletin 399, University of Illinois Engineering Experiment Station, Urbana, Ill.

[3] Rusch, H. (1961). Research toward a General Flexural Theory for Structural Concrete. *ACI Journal*, *57* (1), 1-28.

[4] Ulfkjaer, J. P. (1998). Experimental Investigation of Over-Reinforced Concrete Beams of Three Different Types of Concrete and Two Different Size Scales. *Proceedings FRAMCOS-3,* AEDIFICATI Publishers.

[5] ACI Committee 318 (2008). Building Code Requirements for Structural Concrete and Commentary (ACI 318 08). American Concrete Institute, Farmington Hills, MI, 465 pp.

[6] ACI Committee 435 (2003). Control of deflection in concrete structures (ACI 435R-95). American Concrete Institute, Farmington Hills, MI, 89 pp.

[7] El-Hacha, R., & Rizkalla, S. H. (2002). Fundamental Material Properties of MMFX Steel Bars. Research Report RD02/04, North Carolina State University, Constructed Facilities Laboratory, Raleigh, North Carolina USA, 62 pp.

[8] Bentz, E. C (2002). *Sectional Analysis of Reinforced Concrete*. Doctoral Dissertation, Department of Civil Engineering, University of Toronto, Toronto, Canada.

[9] Bentz, E. C. (2000). Response-2000. Retrieved from http://www.ecf.utoronto.ca/~bentz/r2k.ht

Biographies

FARIS MALHAS is Dean of the School of Engineering & Technology at Central Connecticut State University. He earned a BSE and an MSE in Civil Engineering from the University of Michigan-Ann Arbor, and an MS in Engineering Mechanics and a PhD in Civil Engineering from the University of Wisconsin-Madison. His research interests include the behavior of concrete structures and structural steel design codes and provisions. Dr. Malhas may be reached at fmalhas@ccsu.edu

MUSTAFA MAHAMID is a Clinical Associate Professor at the University of Illinois at Chicago and an independent consultant working for several engineering firms. He earned a BS in Civil Engineering from the Eastern Mediterranean University in Turkey, an MS in Civil Engineering from Bradley University, and a PhD in Civil Engineering from the University of Wisconsin–Milwaukee. Dr. Mahamid has extensive practical experience in industry and has worked on projects in the U.S., Europe, the Middle East, and China. His interests include earthquake engineering, structural steel building behavior and connection design, concrete structures, and computational mechanics. Dr. Mahamid may be reached at mmahamid@uic.edu

ADEEB RAHMAN is an associate professor of engineering mechanics in the Department of Civil Engineering and Mechanics at the University of Wisconsin-Milwaukee. He received a PhD from the University of Wisconsin-Madison in the area of solid mechanics. His area of expertise includes computational structural mechanics, the re-

sponse of steel connections to fire loading, and computational modeling of structural frames in seismic loading. He has more than fifty journal and conference publications in highly specialized publications. He is currently active in research focusing on the performance of steel connections in elevated temperatures. He was twice the recipient of the prestigious Fulbright Award for the U.S. Fulbright Scholarship program. Dr. Rahman may be reached at adeeb@uwm.edu

A General Method for Failure Analysis and Re-Design of a Mechanical Diode

Kevin M. Hubbard, Missouri State University; Martin P. Jones, Missouri State University; Nebil Buyurgan, Missouri State University

Abstract

In this study, the authors performed an extensive investigation on mechanical diode failures and, in this paper offer recommendations for re-designing elements associated with the failure of the mechanism. The analysis can be employed as a case study, which outlines a general method of approach for solving similar problems. Mechanical diode failure data were analyzed based on demographics, component dimensional/geometric and material properties, and mechanics of materials. Strut failure and spring weakening were identified as the two major causes of failure, after a series of investigations on demographics and component properties. In-depth mechanics of materials analyses for struts and springs reveal that weakening and/or failure of the mechanical diode's springs may lead directly to potential strut failures and strut failure may lead to major diode failure. A number of changes in the processing of springs and struts, the material, and geometry are recommended to yield additional benefits.

Introduction

Mechanical diodes are unidirectional clutches used to transmit extremely high torques from the crankshaft of an engine to the driveshaft of a vehicle [1]. In conventional unidirectional clutches (sprag- and roller-style clutches), the torque transmission function takes place as a result of the frictional contact of several small sprags or rollers between inner and outer races [2]. The components incorporated in these types of unidirectional clutches must be machined to extremely small tolerances [3]. Mechanical diodes incorporate rectangular struts, which engage between two plates called a pocket plate and a notch plate, in order to transmit torque. These types of unidirectional clutches incorporate fewer components and, therefore, are capable of transmitting larger torques than sprag- or roller-style clutches, and may be fabricated using less-demanding tolerances.

One manufacturer of agricultural tractors incorporates mechanical diodes as a torque amplifier option on several models. Mechanical diodes incorporated into these tractors experienced high failure rates in service, resulting in significant negative financial impact on the company. In this paper, the authors describe the methods employed for performing failure analyses and re-design of the mechanical diode elements associated with the failure of the mechanism.

The mechanical diode assembly considered in this study exhibited a relatively high failure rate. Failed units exhibited lives of approximately 15 months, on average. Figure 1 depicts the failed unit of a typical mechanical diode, and Figure 2 depicts a complete mechanical diode assembly, which has been cut away to reveal its internal components. Figure 3 shows a schematic diagram of the mechanical diode mechanism.

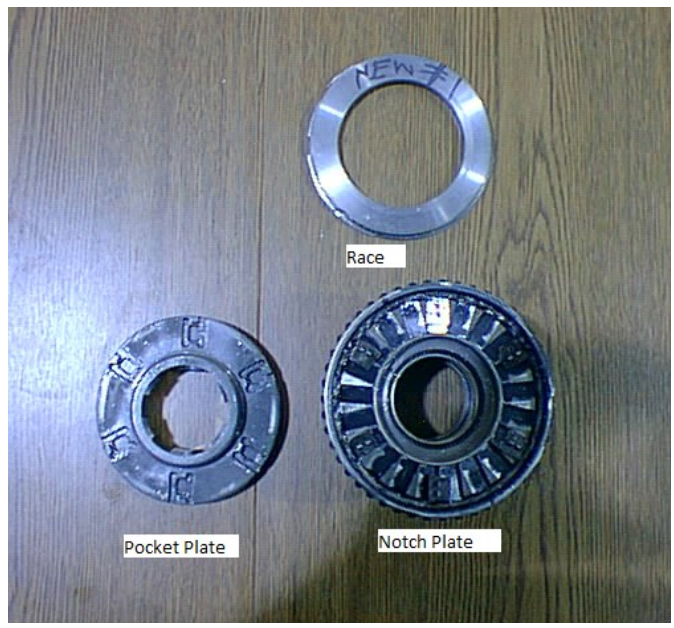

Figure 1. Components of a Failed Mechanical Diode

In order to establish possible causes for these failures and formulate corrective actions, data were collected and analyzed in the following areas:

1. Demographics: The data collected and analyzed in this category related to assembly calendar life, geographic region of service, customer complaint, and causal/symptomatic diagnosis of the failed unit.
2. Component Dimensional/Geometric and Material Properties: The data collected and analyzed in this category related to the conformance of the assembly's component parts with print specifications.

3. Mechanics of Materials Analyses: These calculations related to the strength of the component materials, and the stresses/strains to which these components are subjected in service. Static, dynamic, and fatigue analyses were performed. These analyses focused primarily on the mechanical diode's strut and the double-helical torsion spring components.

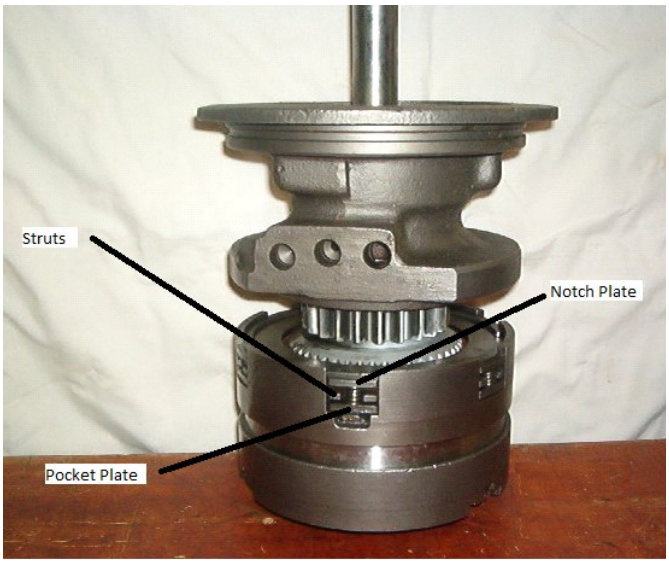

Figure 2. Mechanical Diode Assembly

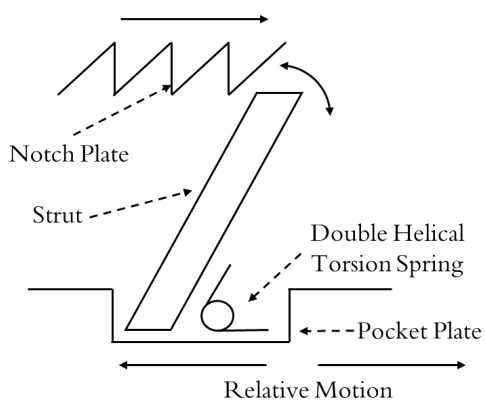

Figure 3. Schematic of a Mechanical Diode Mechanism

Analysis indicated that no correlation existed between unit failure and demographic data. In addition, no major problems with dimensional/geometric and material properties conformance of component parts with print specifications were identified. Furthermore, the number of stress cycles experienced by the spring in service quickly exceeded the spring's fatigue life. It was also noticed that spring weakening might cause non-full engagement of the strut with the tooth and pocket plates, leading to strut failure in compression or buckling.

Materials and Methods

A database containing demographic data was provided by the manufacturer along with failure cause types and failure modes. Failure cause types included broken cap on mechanical diode, low lube pressure, strut failure, and no problem found. Failure modes included freewheel-failure to engage, lockup, intermittent engagement, and no failure mode identified. Failure causes and modes were categorized by using a fishbone diagram, which is a common practice for process improvement [4]. The most common failure mode was complete lockup (85%), followed by freewheel (15%) and intermittent engagement (5%).

Failures were categorized by the U.S. states in which the failure occurred. Sales figures for the mechanical diode were used to determine the approximate percentage of diode failures rates for each state (i.e., number failed/number sold). Failures were also categorized by the month of the year, in an attempt to determine whether extreme temperatures had an effect on mechanical diode life. Table 1 presents the top ten U.S. states with the highest failure rates, and Table 2 presents monthly distribution of failures.

Table 1. States with the Highest Failure Rates

State	% Failure	State	% Failure
IA	14.68	MI	7.61
MD	10.26	OH	6.94
KS	8.93	MO	6.82
PA	8.33	NE	6.41
WI	7.75	AL	6.25

Table 2. Failure Rate by Month

Month	% Failure	Month	% Failure
February	15.58	December	7.37
August	12.21	April	6.95
November	12.00	May	5.26
July	11.79	October	5.26
September	9.89	January	2.32
June	9.47	March	1.89

Another set of data was collected for inspection and measurement of the components' dimensions and material properties, in comparison to specifications shown in Table 3.

Table 3. Components and Measured Properties

Strut	Double-Helical Torsion Spring
dimensions parallelism of surfaces strut included angle visual surface inspection die-penetrant inspection fluor. mag. particle inspection surface hardness	coil diameter wire diameter coil axial length spring constant (k) coil leg length
Pocket Plate	Notch Plate
surface parallelism per print pocket dimensions	visual inspection dimensions

Based on the collected and analyzed data, no correlation was found between climatological conditions, such as temperature as a function of region or of month, and mechanical diode failure rate. The measurements of component properties were compared to the specifications supplied by the manufacturer. No significant departures from the specified dimensional tolerances were found in any of the new or in-service struts, pocket plates, or notch plates. Visual inspection of the struts revealed impact marks on the top (notch plate side) surface of struts, which had seen service and occasional heavy wear and deformation of these struts' contact edges. Material hardness was found to be within specifications, and there appeared to be no external or internal cracks in the struts when inspected using die-penetrant. Fluorescent magnetic particle inspection of the struts also found no discontinuities. A number of struts that had been in service were bent.

An inspection of springs that had been in service revealed a significant incidence of heavy wear on the legs and tongues, and a greatly reduced spring constant (k). Springs that had not been placed in service exhibited spring constants that were within, or were higher than, specification. This indicated that the springs weakened in service. It was concluded that the springs were unlikely to have been subjected to loading in service at or near their natural frequencies, which are a function of spring constant and mass of the sprung load [5]. Analysis of demographic and geometric measurement data dismissed a number of possible failure causes. Two primary failure causes were determined to have high probabilities: strut failure and spring weakening (failure in fatigue).

Strut Stress/Strain Analysis

Many of the possible modes of failure arise as a result of strut column buckling or strut beam bending [6]. It is unlikely that the strut fails in column buckling, since the force required to buckle the column (strut) is so great that compressive fracture should occur before buckling. The following variables are defined for buckling:

P_{cr} = force required to buckle the strut
E = Young's modulus of the strut material
I = second moment of inertia of the strut's column cross-sectional area
L = length of the strut: axial from notch plate to pocket plate
b = the length of the base of the strut's cross-section
h = the thickness of the strut's cross-section

Then, if the strut is loaded as a column, the buckling force can be calculated, as given by Equation (1):

$$P_{cr} = \frac{\pi^2 EI}{L^2} \tag{1}$$

where,

$$\mathrm{I} = \frac{\mathrm{bh}^3}{12}$$

Figure 4 shows the geometry and loading of the strut as a column. Here, b = 0.450 in., h = 0.090 in./cos(15°) = 0.093 in., and I = 3.02×10^{-5} in^4. A typical modulus of elasticity for 1075 steel is approximately 30×10^6 psi and a general value for the modulus of elasticity of 4340 steel is 29×10^6 psi. With E = 29×10^6 psi and L = 0.440 in., the load necessary to induce a column buckling-type failure of the strut is about 44,600 lb. If the strut were to experience a 44,600 lb compressive load, then in the small cross-section (where the cross-sectional area is 0.450 in×0.093 in. = 0.042 in^2), the strut would experience a compressive stress of about 1,061,900 psi.

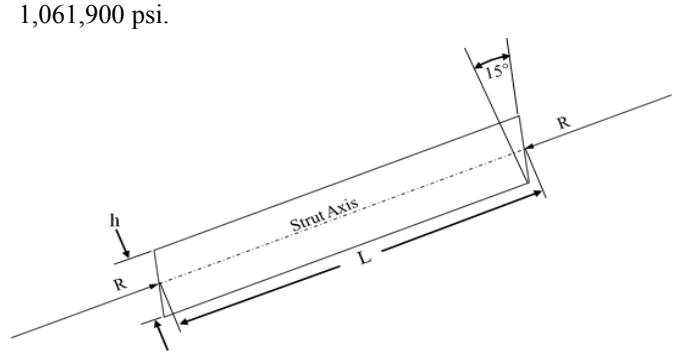

Figure 4. Strut-Free Body Diagram: Zero Eccentricity Loading

Figure 5 shows critical buckling load as a function of strut thickness. If the strut is within dimensional specification, the compressive strength of the material should always be exceeded before pure column buckling occurs. A typical value for compressive strength of this material is 164,500 psi, which is smaller than the stress needed to induce buckling by a factor of approximately six. As a result, strut buckling is an unlikely failure mode.

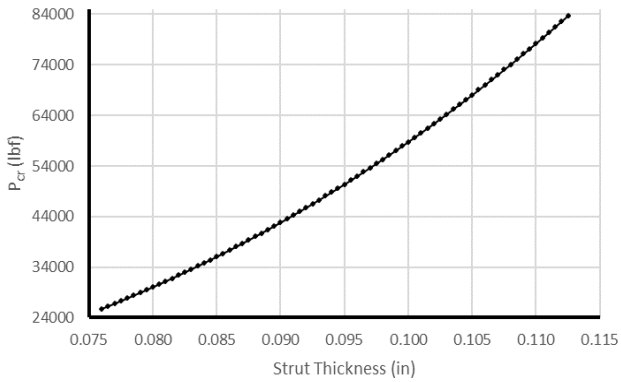

Figure 5. Critical Column Buckling Load versus Strut Thickness

A finite element analysis was also conducted on the strut. If the strut is not misused in service, and assuming that a minimum of three struts engage during any loading cycle (per design specifications), each strut would bear 1840 lb of compressive force with an 800 lb×ft maximum torque carried by the mechanical diode. If only one strut were engaged, that strut would carry 5520 lb of compressive force. If at least three struts are engaged, the stress induced in the small cross-section of the strut is approximately 45,400 psi, which is too small to cause compressive fracture.

However, if only one strut were to be engaged, the stress induced in the small cross section of the strut would be about 136,000 psi. Usually, the compressive strength of 4340 steel ranges between about 109,000 psi and 220,000 psi. If only one strut were engaged while the mechanical diode transmitted a torque of 800 ft×lb, a failure of that strut by compressive fracture is a real possibility. Note that these analyses do not take into consideration any surface imperfections on the faces of the strut. Wear and other sources of notching on the strut face can cause local stress concentrations, making failure more likely. Specifically, if the strut is notched, scratched, or worn, stress concentration factors of 0.5 to 2.0 may apply [7].

The strut experiences complex loading and must be modeled as a beam in compression and bending. Figure 4 also depicts static loading on one strut when that strut is fully engaged. The notch plate is at the top of the figure and the pocket plate is below. The assumption that three struts are engaged during loading results in a compressive stress of σ_{axial} = 45,400 psi, which is significantly below the compressive strength of the material. If the strut is not fully engaged upon loading, however, the forces exerted by the notch plate/pocket plate combination may be off-axis, resulting in eccentric strut loading. In this case, the two resultants form a couple, placing the strut in both bending and compression, as shown in Figure 6.

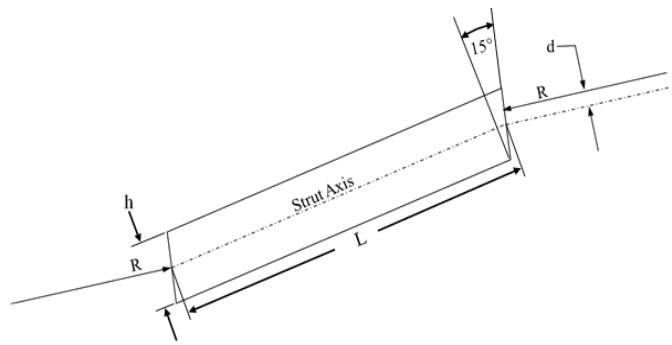

Figure 6. Strut-Free Body Diagram: Eccentrically Loaded

The moment, M, generated by this couple is calculated using Equation (2):

$$M = dR \tag{2}$$

The normal stress due to bending, σ_b, is then calculated using Equation (3):

$$\sigma_b = \frac{My}{I} \tag{3}$$

where, y is the distance from the strut's neutral axis to the fiber of interest and I is the second moment of inertia of the beam's cross-section area.

The neutral axis in this case coincides with the centroidal axis. Evaluating σ_b at the top and bottom surfaces of the strut, where s_b is maximum, with y = 0.045 in., I = 2.73´10^{-5} in^4, and an eccentricity d = 0.023 in., results in a moment of 42.3 in×lb and a bending stress of 69,725 psi, which is safely below the tensile and compressive yield strengths of the strut material. Note that, as designed, the strut would experience compression on its top surface and tension on its lower surface. If the strut were subjected only to bending, and if at least three struts were engaged as the mechanical diode transmitted 800 lb×ft of torque, the struts would not experience a significant probability of failure. With only two struts engaged, σ_b = 139,400 psi leads to a significant possibility of strut bending failure. With a single strut engaged, σ_b = 209,200 psi and strut bending failure is almost a certainty.

If d = 0.030 in. and σ_b = 90,990 psi (with three struts engaged), then this leads to a significant chance of strut bending, given the range of strengths for 4340 steel due to batch variation of struts. It is evident that only a small increase in the eccentricity of the strut loading causes a correspondingly large increase in the normal stress induced in the strut due to bending moment. If the strut is loaded complexly in compression and bending, the following variables are related in Equation (4), where σ_c is the compressive normal stress due to the resultant force, R, in a cross-sectional area, A:

$$\sigma_c = \frac{R}{A} \tag{4}$$

With three struts engaged and with the mechanical diode transmitting a torque of 800 lb×ft, σ_c evaluates to 45,432 psi compressive. The principle of superposition states that the stresses in the member may be algebraically added at any given point. Equation (5) shows this force, which defines σ_{tot} as the total stress in the strut at a point of interest:

$$\sigma_{tot} = \sigma_c + \sigma_b \tag{5}$$

With three struts engaged and d = 0.023 in., while the diode transmits a torque of 800 lb×ft, then $\sigma_{tot\ top}$ = -45,432 + 69,725 = 24,293 psi (tension) and $\sigma_{tot\ bottom}$ = -45,432 + -69,725 = -115,157 psi (compression). Note: subscript "top" indicates the stress on the top (notch plate engaging) surface and the subscript "bottom" denotes the bottom (pocket plate engaging) surface of the strut. Eccentric loading also produces a shear stress, τ, in the strut, as defined by Equation (6):

$$\tau = R/A_L \tag{6}$$

where, A_L is the transverse cross-sectional area of the strut.

Under the same assumptions (three struts engaged, 800 lb×ft torque) and with L = 0.440 in., A_L = 0.440 in×0.450 in. = 0.198 in^2, then τ is evaluated at 9300 psi. The shear strength of 4340 steel is approximately 124,000 psi. Under this complex loading situation, the principal stresses (σ_{p1}, σ_{p2}, and τ_{max}) induced in the strut were evaluated using the standard Mohr's Circle plane-stress method. Table 4 enumerates these principal stresses. In Cases 1 and 2, the potential exists for strut failure in compression. Note that if one strut fails to engage, then the likelihood of failure of the engaged struts increases dramatically. Also note that these principal stresses rise dramatically with increases in eccentricity.

Each of the preceding analyses was done under the best-case assumption that the strut is loaded statically. The following analysis is based on equations developed in mechanical design textbooks. If the strut is loaded dynamically, impact deformation can be calculated [8] using Equation (7):

$$\delta_{max} = \delta_{st}\left[1 + \left(1 + 2\frac{h}{\delta_{st}}\right)^{\frac{1}{2}}\right] \tag{7}$$

where,

δ_{max} = maximum deformation of a mechanical member under a sudden or impact dynamic load
δ_{st} = mechanical member deformation under static load
h = height corresponding to a gravitational potential energy absorbed by a mechanical member when a weight is dropped on that member
R = load on the member
L = length of the member along the axis of the load
E = Young's modulus of the member
A = member cross-sectional area perpendicular to load

Table 4. Principal Stresses at Two Values of Eccentricity

d = 0.0225 in., Torque = 800 lb×ft, 3 struts engaged	
Top Surface (Case 1) Principal Stress Values (psi)	Bottom Surface (Case 2) Principal Stress Values (psi)
s_{p1} = 26100 (T)*	s_{p1} = 114400 (C)
s_{p2} = 3300 (C)	s_{p2} = 755 (T)
t_{max} = 14700	t_{max} = 57600
d = 0.0300 in., Torque = 800 lb×ft, 3 struts engaged	
Top Surface (Case 3) Principal Stress Values (psi)	Bottom Surface (Case 4) Principal Stress Values (psi)
s_{p1} = 47400 (T)	s_{p1} = 137000 (C)
s_{p2} = 1800 (C)	s_{p2} = 630 (T)
t_{max} = 24600	t_{max} = 69000

* (T) denotes tension and (C) denotes compression

Note that δ_{st} is given by Equation (8):

$$\delta_{st} = \frac{RL}{EA} \tag{8}$$

Since h = 0 for these struts, Equation (7) simplifies to Equation (9):

$$\delta_{max} = 2\delta_{st} \tag{9}$$

If for a resultant R = 1840 lb (for three struts engaged as the diode transmits a torque of 800 lb×ft) and assuming L = 0.440 in, A = 0.090 in×0.450 in. = 0.0405 in^2, and E = 29´10^6 psi, then δ_{st} = 6.89´10^{-4} in. and δ_{max} = 1.38´10^{-3} in. As a result, the maximum strain induced in the strut by

this sudden load is 0.00313 in/in. Assuming a stress of 164,500 psi, which is the midpoint of the 4340 steel yield range, the strain at which the strut yields is 0.00567 in/in. For sudden loading, then, the strut was designed with a factor of safety of less than two. In the event that a single strut fails to engage, the likelihood is very high that the remaining two struts will fail. In addition, any eccentricity with which the load is applied reduces the effective cross-sectional area of the strut, also making strut failure likely. In the preceding analysis, a number of problems were shown to arise if one or more struts (out of three) fail to engage, or fail to engage fully. The most likely cause of partial- or non-engagement of the strut is spring weakening or failure, which will now be discussed.

Spring Life Analysis

When a torque is applied to a torsion spring, the wire in the spring coil is placed in tension on its outer (farthest from the coil axis) surface and in compression on its inner surface. The residual stresses left behind in the wire after the spring winding operation are in the same plane as the working stress, but of opposite sense. These residual stresses tend to prolong the life of the spring as long as the load is applied to the spring in such a way as to cause the spring to wind up, not un-wind [9]—see Equations (10) and (11):

$$M = Fr \text{ and } \sigma = K\frac{Mc}{I} \tag{10}$$

where,
M = bending moment to which the spring is subjected
F = external force applied to spring
r = perpendicular distance: force application to coil axis
σ = normal stress induced in coil wire by applied load F
K = a stress concentration factor
c = distance from spring wire neutral axis to a fiber
I = moment of inertia of wire cross sectional area with respect to neutral axis

$$C = \frac{D}{d},\ K_i = \frac{4C^2 - C - 1}{4C(C-1))},\ K_o = \frac{4C^2 + C - 1}{4C(C+1)} \tag{11}$$

where,
K_i = stress concentration factor for inner surface of wire
K_o = stress concentration factor for outer surface of wire
C = spring index
D = mean spring diameter
d = spring wire diameter

For this current study, since the spring index C was greater than one, the stress concentration factor for the outer surface, K_o, of the wire was less than one, and K_i was greater than one. For the worst case, K_i would be employed for stress determination. Substituting M = Fr into the normal stress Equation (10), Equations (12)-(15) are obtained for round wire:

$$\frac{I}{c} = \frac{\pi d^3}{32} \quad \text{results in} \quad \sigma = K_i\left(\frac{32Fr}{\pi d^3}\right) \tag{12}$$

where,
θ = spring angular deflection from its "at-rest" position (rad)
E = Young's modulus of the spring wire
k = torsion spring constant, aka spring rate (torque/rad)
N = number of coils (turns) in the spring under zero load

$$\theta = \frac{67.8\ FrDN}{d^4E} \tag{13}$$

$$k = \frac{Fr}{\theta} = \frac{d^4E}{67.8DN} \tag{14}$$

$$D_i' = \frac{N}{N'}D_i \tag{15}$$

where,
D_i = inside coil diameter under zero load
D_i' = inside coil diameter when loaded
N' = number of spring coil turns when loaded

The ultimate tensile strength of the wires commonly used in springs depends on the diameter of the spring wire. A good approximation for this relationship is given by Equation (16):

$$S_{ut} = \frac{A}{d^m} \tag{16}$$

where, A and m are taken from Table 5 [10].

Table 5. Constants and Wire Diameters Used in S_{ut} Calculation for Spring Types Used by the Manufacturer

Type	Material	ASTM	m	A (kpsi)	d (in)
1	Music Wire	A228	0.163	186	0.0140
2	Cr-V	A232	0.155	173	0.0136
3	302 Stainless	A313	0.146	169	0.0120

Equation (17) was used to determine the maximum operating torque for "infinite" (10^6 cycles) spring life, and the deflection θ, which corresponds to that torque:

where,
$(Fr)_a$ = torque amplitude
$(Fr)_m$ = mean torque

$(Fr)_{max}$ = maximum cyclic external torque on the spring
$(Fr)_{min}$ = minimum cyclic torque on the spring

$$(Fr)_a = \frac{(Fr)_{max} - (Fr)_{min}}{2}$$
$$(Fr)_m = \frac{(Fr)_{max} + (Fr)_{min}}{2} \quad (17)$$

The current analysis employed the Goodman fatigue model, since it is among the most conservative [11]. The mod-Goodman equation is given in Equation (18):

$$\frac{\sigma_a}{S_e} + \frac{\sigma_m}{S_{ut}} = \frac{1}{n} \quad (18)$$

where, S_e is further defined in Equation (19) as the endurance limit of spring wire:

$$S_e = \frac{0.5S_r}{1 - \left(\frac{0.5S_r}{S_{ut}}\right)^2} \quad (17)$$

where,

$$S_r = aS_{ut}$$

Using Equation (19) for unpeened springs, the endurance limits for spring types 1, 2, and 3 were 100 kpsi, 99 kpsi, and 86 kpsi, respectively. Note the factors for "a" used in Equation (19) were 0.50, 0.53, and 0.50 for spring types 1, 2, and 3, respectively.

By substitution of Equations (10), (12), and (17) into Equation (18), Equation (20) shows how infinite life can be obtained:

$$(Fr)_{max} = \frac{\frac{S_{ut}S_e\pi d^3}{16K_i n} - S_e(Fr)_{min} + S_{ut}(Fr)_{min}}{S_{ut} + S_e} \quad (20)$$

Based on the geometry of the pocket/notch plate, the spring can "unwind" at most to approximately 35°, experiencing an angular deflection, θ, of 25º (0.436 rad) during over-run. As the strut passes under a tooth on the notch plate, the spring must deflect to an included angle of approximately 12°, resulting in an angular deflection of 48º (0.838 rad). For the three types of springs incorporated in various production runs of the mechanical diode, Table 6 delineates the spring constants and maximum/minimum torques to which the spring was subjected, corresponding to these θ values.

Table 6. Spring Maximum and Minimum Actual Torques at Low Rotational Speed

Type	k (lb×in/rad)	$(Fr)_{max}$ (lb×in)	$(Fr)_{min}$ (lb×in)
1	0.0283	0.0237	0.0123
2	0.0280	0.0235	0.0122
3	0.0124	0.0104	0.0054

The results obtained through the use of Equation (20) are detailed in Table 7. $T_{max\ N=10^6}$ is the maximum torque allowable, if the strut is to survive for 10^6 cycles.

Table 7. Maximum Allowable Torques for "Infinite" Life with Factor of Safety = 1

Type	$T_{max\ N=10^6}$ (lb×in)
1	0.0440
2	0.0389
3	0.0237

The $(Fr)_{max}$ torque values in Table 6 should not be allowed to exceed those in Table 7. The torque values in Table 7 are based on the following assumptions:

- All spring wire diameters are exactly nominal.
- All other spring dimensions are exactly nominal.
- All spring properties (E, S_{ut}, etc.) are exactly equal to their theoretical properties.

Considering spring Type 2, listed in Tables 6 and 7, further analysis was made considering the following items:

1. If the coil diameter is allowed to go to its lower limit, then $T_{max\ N=10^6}$ remains unchanged.
2. If the wire diameter is as small as d = 0.0136 in (a ± 0.0004-in. tolerance is not unusual for this size spring wire), then $T_{max\ N=10^6}$ = 0.0387 lb×in,, which is a significant decrease.
3. With a combination of both Items 1 and 2 above, $T_{max\ N=10^6}$ = 0.0389 lb×in.
4. These groups of geometric changes result in the same sort of corresponding change in $T_{max\ N=10^6}$, regardless of spring type.
5. Changes in the Young's modulus of the spring wire do not affect $T_{max\ N=10^6}$.
6. For all spring types, with a factor of safety of two, $(Fr)_{max}$ nearly equals or exceeds $T_{max\ N=10^6}$, resulting in a less than "infinite" life.

Figure 1 show how each of the 21 teeth in the notch plate travels across each strut of the mechanical diode. Therefore, at a maximum over-run rotational speed of 5000 rpm, the

strut experiences 6.3×10^6 stress cycles per hour. This indicates that each spring in the mechanical diode, at 5000 rpm over-run, may be expected to experience 10^6 cycles in only 9.5 minutes of service. In approximately 16 hours of 5000 rpm over-run service, each spring sees 10^8 cycles. As the rotational speed of the mechanical diode decreases, the number of hours of service that the springs can be expected to survive in over-run increases, so that at 500 rpm, for example, the springs should see 10^8 cycles of service in 160 hours.

This analysis was performed under the assumption that the spring deflects as far toward its relaxed position, as is geometrically permitted when the tip of the strut passes through the cavity between notch-plate teeth during over-run. It was also assumed that the tip of the strut would make physical contact with each tooth as it passes over the strut. As $(Fr)_{min}$ decreases, the life of the strut also decreases, with the worst possible case (shortest life) occurring when $(Fr)_{min} = 0$. In light of this fact, this analysis covered the worst-case scenario: rotational speed is low enough to allow full relaxation of the spring into the notch-plate cavity.

It is possible that, at higher rotational speeds, the spring does not relax to as great an extent as at low rotational speeds. Here, the force preventing spring relaxation is the dynamic pressure caused by the relative velocity of the fluid with respect to the strut. In order to ascertain the angles to which the struts and springs were deflected by the fluid's dynamic pressure, equations were developed that dealt with the effective area of the strut presented to the fluid stream, the relative velocity of the fluid with respect to the strut (using mass continuity), the dynamic pressure caused by fluid velocity, and the force arising from that dynamic pressure. The torque produced on the strut-spring system by this force was then balanced against the torque provided by the spring, since at the top and bottom of the strut's rotation, angular acceleration was zero and these torques must balance. These equations were then solved iteratively for θ. This analysis was performed at 5000, 2500, and 1000 rpm. The results are presented in Table 8.

Table 8. q_{max} as a Function of Rotational Speed Accounting for Fluid Dynamic Pressure

	Speed (rpm)	q_{max} (deg.)	Speed (rpm)	q_{max} (deg.)	Speed (rpm)	q_{max} (deg.)
1	5000	25.26	2500	25.28	1000	0
2	5000	25.26	2500	25.28	1000	0
3	5000	25.25	2500	25.26	1000	0

Even at 5000 rpm, θ_{min} was calculated to be zero degrees. Neither the θ_{max} values in Table 8, nor the θ_{min} value of zero is possible, if the geometry of the notch-plate is taken into account. This analysis did not include the effects of fluid viscosity and the time response of the strut to moments and forces acting upon it. However, one conclusion drawn from these θ values was that the geometry of the notch-plate (not the rotational speed of the mechanical diode) is most likely the controlling factor in determining the maximum and minimum values of θ. Therefore, the maximum and minimum values of torque experienced by the spring are limited by the geometry of the notch plate. If this is the case, then the life values obtained previously are valid, regardless of the rotational speed at which the mechanical diode is operated.

Results and Discussion

One conclusion arising from this extensive analysis is that there was no correlation between unit failure and demographic data. Also, no major problems were identified with dimensional/geometric and material properties conformance of the component parts with print specifications. Weakening and/or failure of the mechanical diode's springs may lead directly to potential strut failures. The following corrective measures are indicated:

1. Prevention of Spring Wire Mechanical Stress Relief during Service: It is likely that the residual stresses left behind by the spring winding operation are being mechanically relieved. This stress relief shortens the spring's fatigue life and reduces the Young's Modulus of the spring wire, leading to reductions in the spring constant, k. This leads to eccentric loading of the strut, potentially causing the strut to fail in compression. One way that this may be prevented is to subject the spring, after the winding operation, to a stress relief heat treatment, thus removing residual stresses before the spring is placed in service. If this is done, the spring constant should remain constant, or nearly so, throughout the spring's time in service. Note that if the spring is subjected to a stress relief heat treatment before being placed in service, its geometry must be modified so that the proper spring constant is obtained after heat treatment [12].
2. Modification of Spring Geometry: The spring's geometry governs the stress to which the spring wire is subjected during loading. Increasing the spring wire diameter, d, and/or decreasing coil diameter, D, reduces stress developed in the wire in service.
3. Spring Wire Material Substitution: A spring wire material with a higher ultimate tensile strength

should provide a longer fatigue life [13]. Implementation of this action alone is not recommended, however. One or both of the two actions listed previously should also be employed.

Strut failure may lead to both the lockup-failure mode and the failure-to-engage mode. Strut failures are likely to occur primarily as a result of spring weakening and/or failure. Changes in the processing of the strut, the strut material, and the strut geometry may, however, yield additional benefits. The following corrective actions are indicated with respect to the strut components:

1. Elimination of Any Residual Compressive Stresses: The strut is subjected to a deburring operation, which may leave behind residual stresses. These residual stresses increase the effective stress experienced by the strut during loading and may lead to premature strut failure. These residual stresses may be removed using a stress relief heat treatment, followed by a strengthening heat treatment to produce the final desired material properties. In addition, if decarburization of the strut is a concern, the strut may be carburized during this heat treatment cycle.
2. Strut Yield Strength Improvement: A higher yield and/or ultimate tensile strength may be desirable, and may be obtained by material substitution or selection of the proper heat treatment. Care should be taken, however, when strengthening the material, to avoid causing susceptibility to failure during sudden loading or impact.
3. Strut/Pocket Plate/Notch Plate Geometry Modification: Sharp corners on the strut act as stress risers. If a change in geometry becomes necessary, these corners should be radiused. Also, the triangular region at each end of the strut has a smaller cross sectional area than the body of the strut. Thus, stresses in these regions are higher than those calculated previously, which could be avoided by providing, if feasible, a generous radius on each end of the strut. This change, while costly, would have the additional benefit of making the strut self-aligning. Actions 1 and 2 should be considered first, before recommendation 3 is implemented.

Conclusions

Focusing on mechanical diode failures, the authors conducted an extensive study on struts, spring design, and their properties. Major changes are recommended in the processing of springs, the material, and the geometry, including those of the spring wire and coil diameter. Also recommended are strut material strength improvement (via heat treatment) and strut geometry modifications. The analysis presented in this paper represents a thorough approach to the investigation of the mechanical failure of components subjected to a wide variety of service conditions, and may be used as a case study that outlines a general method of solution for similar problems. Demographic factors based on geography and seasons were considered. While these factors were concluded not to have measurable impact on failure, it is recommended to include these in future failure investigations.

References

[1] Thorpe, J. F. (1989). *Mechanical System Components*. Prentice Hall.

[2] Budynas, R. G., & Nisbett, J. K. (2015). *Shigley's Mechanical Engineering Design.* (10th ed.). McGraw-Hill Education. New York.

[3] Chesney, D. R., & Kremer, J. M. (1998). *Generalized equations for sprag one-way clutch analysis and design*. (SAE Technical Paper, no. 981092).

[4] Farahmand, K., Grajales, J. V. M., & Hamidi, M. (2010). Application of Six Sigma to Gear Box Manufacturing. *International Journal of Modern Engineering*, *11*(1), 12-19.

[5] Maier, J. R., Mears, M. L., & Summers, J. D. (2013). Design of an Apparatus to Detect Small Changes in the Mass of Rotational Machine Components. *International Journal of Modern Engineering*, *13*(2), 5-16.

[6] Hayduk, R.J., & Wierzbicki, T. (1984). Extensional Collapse Modes of Structural Members. *Computers & Structures*, *18*(3), 447-458.

[7] Blandford, G. E. (1997). Review of Progressive Failure Analyses for Truss Structures. *Journal of Structural Engineering*, *123*(2), 122-129.

[8] Collins, J. A., Busby, H. R., & Staab, G. H. (2010). *Mechanical Design of Machine Elements and Machines.* (2nd ed.). Wiley.

[9] Akiniwa, Y., Stanzl-Tschegg, S., Mayer, H., Wakita, M., & Tanaka, K. (2008). Fatigue Strength of Spring Steel under Axial and Torsional Loading in the Very High Cycle Regime. *International Journal of Fatigue*, *30*(12), 2057-2063.

[10] Associated Spring-Barnes Group. (1987). *Design handbook: engineering guide to spring design.* Bristol, CT.

[11] Osakue, E. E. (2011). A Linearized Gerber Fatigue Model. *International Journal of Modern Engineering*, *12*(1), 64-72.

[12] Del Llano-Vizcaya, L., Rubio-Gonzalez, C., Mesmacque, G., & Banderas-Hernández, A. (2007).

Stress Relief Effect on Fatigue and Relaxation of Compression Springs. *Materials & Design*, *28*(4), 1130-1134.

[13] Kaiser, B., & Berger, C. (2005). Fatigue Behaviour of Technical Springs. *Material Science and Engineering Technology, 36*(11), 685-696.

Biographies

KEVIN M. HUBBARD is an assistant professor of Technology and Construction Management at Missouri State University. He earned his BS degree (Aerospace Engineering, 1991), MS (Engineering Management, 1993), and PhD (Engineering Management, 1996), all from the University of Missouri–Rolla. Dr. Hubbard is currently teaching at Missouri State University. His interests include in automation and device control, manufacturing systems, device design, and process optimization. Dr. Hubbard may be reached at KHubbard@MissouriState.edu

MARTIN P. JONES is an associate professor of Technology and Construction Management at Missouri State University. He earned his BS degree (Physics, 1981) from University of Maryland Baltimore County, MS (Materials Science and Engineering, 1984) from the Johns Hopkins University, and PhD (Materials Science and Engineering, 1987) from the Johns Hopkins University. Dr. Jones is currently teaching at Missouri State University. His interests include in scanner technology, nondestructive evaluation, manufacturing processes, and quality assurance. Dr. Jones may be reached at MartinJones@MissouriState.edu

NEBIL BUYURGAN is an associate professor of Technology and Construction Management at Missouri State University. He earned his BS degree (Industrial Engineering, 1998) from Istanbul Technical University, Turkey, MS (Engineering Management, 2000) from the University of Missouri–Rolla, and PhD from the University of Missouri–Rolla (Engineering Management, 2004). Dr. Buyurgan is currently teaching at Missouri State University. His interests include in optimization of logistics operations in manufacturing, healthcare, military and retail, and supply chain management. Dr. Buyurgan may be reached at NebilBuyurgan@MissouriState.edu

LATENCY AND PHASE TRANSITIONS IN INTERCONNECTION NETWORKS WITH UNLIMITED BUFFERS

Lev B. Levitin, Boston University; Yelena Rykalova, UMass Lowell

Abstract

In this paper, the authors present theoretical and numerical results for the performance of one-dimensional and a two-dimensional multiprocessor network models wrapped around a network of routers with local processors that generate messages with rate λ. The router models had two and four output/input ports, respectively. Output ports were assumed to have infinite capacity and are presented here as M/D/1 queues. Explicit expressions for the distribution of the number of messages in output port queues, the average message delivery time (latency), and critical network load depending on distance between source and destination were found. Theoretical results were verified with a simulation, which proved the validity of the mean field theory for these types of networks, in accordance with the Jackson theorem.

Introduction

Current state-of-the-are computers usually consist of self-contained processing nodes, with associated memory and other supporting devices. This type of architecture provides many advantages, making it possible to perform massively parallel information processing. However, parallel computing in such systems requires extensive communications between processors. These inter-processor communications are implemented by sending messages from one node to another via a communication network. This network is implemented as a set of interconnected routers, each connected to its local processor. Several of the most advanced supercomputers, such as Sequala (BlueGene/Q, IBM), Titan (Cray XK7), and Trinity (Cray Xc40), have a multi-dimensional toroidal inter-processor network topology. This implementation of a network reduces the path length between nodes and simplifies routing algorithms for static or dynamic routing.

Many studies [1, 2] have been devoted to analyzing computer communication networks as networks of queues. The first most important result was obtained by Jackson [3], where he proved that for an open network of single-server queues with exponential arrival/departure rates, "the equilibrium joint probability distribution of queue lengths is identical with what would be obtained by pretending that each individual service center is a separate queuing system independent of the others." Subsequently, Gordon and Newell [4] and Buzen [5] showed that the state distribution for the M/M/m queuing network has a product form for the first-come-first-served (FCFS) queuing discipline. (The M/M/m queuing network consists of nodes that have a Poisson flow of incoming messages, exponential distribution of service time, and m servers.) The Baskett, Chandy, Muntz, and Palacios (BCMP) theorem [6] extends this property of the state distribution for cases in which the service rate is not necessarily exponential, but has a distribution with a rational Laplace transform, and the queuing discipline is one of the following four cases: FCFS, processor sharing (PS), infinite server (IS), or last-come-first-served (LCFS). For FCFS, the service time distribution must be a negative exponential. Subsequently, three other classes of networks with exponential service times have been shown to have product form distributions [7-9]. Networks with this property have been analyzed further in [10-14]. Yet other models have been based on queueing theory [15-20]. Recently, efforts of many researchers focused on critical phenomena in computer communication networks [21-33]. Congestion and other phase transitions were observed and analogies with statistical mechanics were considered.

One-Dimensional Case: Ring Topology

Each node in the current model consisted of a local processor, a router, and buffers of infinite capacity. In this one-dimensional case, each node was connected to two neighbors, left and right, and had two output ports/buffers. The following conventions were made in the model.

1. At any clock cycle, a message intended for each of the output ports could be generated by the local processor at every node, independently of others, with a constant probability λ.
2. All messages are to be sent to a destination at a distance exactly l hops from the source. (The distance between neighbors is equal to one hop.)
3. Any message generated at the node or arriving from a neighboring node is placed immediately in the output buffer in the direction of the shortest path to the destination.

4. At any clock cycle, if a buffer is not empty, exactly one message is transferred to the neighboring node, and it appears at that node at the next clock cycle. Thus, the service time is equal to one clock cycle.
5. If there is more than one message in the buffer, a message to be transferred is chosen at random with equal probabilities, the so-called SIRO (service-in-random-order) queueing discipline.
6. At the time (clock cycle) when a message reaches its destination, it is immediately consumed and leaves the network.

Two-Dimensional Case: Torus

In the two-dimensional case, each node had four neighbors and, correspondingly, four output ports/buffers. In addition to the conventions listed for the 1-dimentional case, the following rules were accepted.

1. At any clock cycle, a message intended for each of the output ports could be generated independently at every node with probability λ.
2. Each of $4l$ destinations at distance l from the source has the same probability of receiving a message.
3. If there is a choice between intermediate nodes on a shortest path to the destination, each of them is chosen with probability ½.
4. Two different queueing disciplines were considered: SIRO and the priority discipline in which a newly generated message is sent first (new-first-order, or NFO).

It can be seen that this current system differs from networks for which the product form of the limiting state probabilities was proved earlier for a number of characteristics.

1. Time is discrete and arrivals occur with specific probabilities, depending on the distance l (non-Poisson and non-binomial), as given below by (12).
2. Both SIRO and NFO queueing disciplines were considered.
3. The service time is deterministic and does not belong to the class of service time distributions with rational Laplace transforms.

In general, the choice of models was dictated by two opposing considerations. On the one hand, the models were supposed to reflect some important features of real-life situations. In particular, the assumption of deterministic service time is quite natural for homogeneous messages of the same volume. This case is interesting for researchers, since it does not satisfy the conditions for which Jackson's theorem was proved. On the other hand, the model should be simple enough to allow a full-fledged theoretical analysis that would reveal fundamental properties of the communication process in the network, in the most general closed form as functions of the parameters of the process. (In particular, it was important to fix the distance between the source and destination as one such parameter). Of course, this task cannot be accomplished by computer simulation.

Theoretical Analysis

The Ring

The time evolution of the queue at each node buffer was considered as a Markov chain, where the next state depends on the present state of the buffer, while assuming the steady - state probability distribution for states of all other buffers. This approach is similar to the "mean field theory" in statistical physics. The goal of this current project was to obtain an explicit analytical expression for the distribution of the number of messages in a buffer at the steady state (equilibrium) of the network, as it depends on the load λ, and to determine the critical value of the load that results in saturation. Let us call the grade of a message the number k of hops the message has made towards the destination. For the chosen value of the parameter l, there exist messages of l different grades in the system: $k = 0,1,\ldots, l - 1$, since the messages of grade l disappear from the system. Note that a message of grade k that leaves a node appears at the next node as a message of grade k+1. The state of a buffer can be described as a vector $(n_0, n_1,\ldots, n_{l-1})$, where n_k is the number of messages of grade k. Denote the limiting (steady-state probabilities) of a state by $p(n_0, n_1,\ldots, n_{l-1})$ in Equation (1):

$$\sum_{k=0}^{l-1} n_k = n \tag{1}$$

According to the SIRO discipline, the probability that a message of grade k will be transferred is equal to n_k/n. Under the steady-state condition, at any clock cycle, the expected number of messages generated at a node should be equal to the expected number of messages of grade 0 that leave the queue. On the other hand, these messages have grade 1 when they enter the next node, and their expected number is equal to the expected number of the messages of grade 1 that leave the next node, and so on, as shown in Equation (2):

$$\begin{aligned}\lambda &= \sum_{n=1}^{\infty}\sum_{n_0=0}^{n}\cdots\sum_{n_{l-1}=0}^{n}\frac{n_0}{n}p(n_0,n_1,\ldots,n_{l-1})\\ &= \sum_{n=1}^{\infty}\sum_{n_0=0}^{n}\cdots\sum_{n_{l-1}=0}^{n}\frac{n_1}{n}p(n_0,n_1,\ldots,n_{l-1}) = \ldots\\ &= \sum_{n=1}^{\infty}\sum_{n_0=0}^{n}\cdots\sum_{n_{l-1}=0}^{n}\frac{n_{l-1}}{n}p(n_0,n_1,\ldots,n_{l-1})\end{aligned} \tag{2}$$

Since exactly one message is transferred from any state except the zero state, Equation (3) follows from Equation (2),

$$\sum_{k=0}^{l-1}\sum_{n=1}^{\infty}\sum_{n_0=0}^{n}\cdots\sum_{n_{l-1}=0}^{n}\frac{n_k}{n}p(n_0,n_1,\ldots,n_{l-1}) = l\lambda = 1-p(0,0,..,0) \tag{3}$$

and, finally, Equation (4):

$$p(0,0,\ldots,0) = 1 - l\lambda \tag{4}$$

Equation (5) shows how the limiting probabilities of all states with the same total number n of messages of all grades are equal:

$$p(n_0,n_1,..,n_{l-1}) = \frac{m!(l-1)!}{(m+l-1)!}P(n) \tag{5}$$

where, n is given by (1), $\frac{(m+l-1)!}{m!(l-1)!}$ is the number of different states with n messages; and, $P(n)$ is the total probability of all states with n messages.

After simplification, the balance equations for the limiting probabilities are given as Equation (6):

$$\begin{aligned}&\left(\frac{1-\lambda}{l}+\frac{(l-1)(1-2\lambda)}{l}P(0)\right)P(n)\\&=\lambda\frac{l-1}{l}(1-P(0))P(n-1)+(1-\lambda)\left(\frac{1}{l}+\frac{l-1}{l}P(0)\right)P(n+1)\\&\text{(for } n\geq 3)\\&\left(\frac{1-\lambda}{l}+\frac{(l-1)(1-2\lambda)}{l}P(0)\right)P(n)\\&=\lambda\frac{l-1}{l}(1-P(0))P(n-1)+(1-\lambda)\left(\frac{1}{l}+\frac{l-1}{l}P(0)\right)P(n+1)\\&\text{(for } n\geq 3)\end{aligned} \tag{6}$$

where, $P(0) = p(0,0,..,0)$ is given in Equation (4):

Limiting probabilities are obtained by solving the system of Equation (6) into Equation (7):

$$\begin{aligned}P(1)&=(1-l\lambda)\left[\frac{1}{(1-\lambda)(1+\lambda-l\lambda)}-1\right],\\P(n)&=(1-l\lambda)\frac{\lambda^{2(n-1)}(l-1)^{n-1}}{(1-\lambda)^n(1+\lambda-l\lambda)^n}, \qquad \text{for } n\geq 2\end{aligned} \tag{7}$$

Hence, the distribution of the size of the queue is geometric starting with n =2, and the average number of messages in a queue is given by Equation (8);

$$\bar{n} = \sum_{n=1}^{\infty} nP(n) = \frac{\lambda^2(l-1)}{1-l\lambda} + l\lambda \tag{8}$$

average latency is given by Equation (9);

$$\tau = \frac{\bar{n}}{\lambda} = \frac{\lambda(l-1)}{1-l\lambda} + l \tag{9}$$

and critical load is given by Equation (10):

$$\lambda_{crit} = \frac{1}{l} \tag{10}$$

Note that the critical exponent of Equations (8) and (9) is equal to 1.

The Torus

In the two-dimensional case, similar to the ring case, the limiting probabilities of all states with the same total number n of messages of all grades are equal. Therefore, the equations for limiting probabilities can be written in terms of $P(n)$, where n is the total numbers of messages in the buffer. However, an important difference between the 1-dimentional and 2-dimentional cases is that, while in the Markov chain for the 1-dimentional case there are transitions from a state with n messages only to states with $n-1$, n, and $n+1$ messages $n \geq 1$), in the 2-dimentional case, there exist transitions from a state with n messages to the states with $n-1$, n, $n+1$, $n+2$, and $n+3$ messages ($n \geq 1$). Interestingly, the balance equations for $P(n)$ turn out to be the same for both SIRO and NFO.

Denoting a_i (i = 0,1,2,3) as the probability that exactly i messages arrive at a particular buffer from neighboring nodes during one clock cycle, Equation (11) follows from the description of the model given above:

$$\begin{aligned}a_0&=\left(1-\frac{(l-1)\lambda}{2}\right)\left(1-\frac{(l-1)\lambda}{4}\right)^2\\a_1&=\frac{(l-1)\lambda}{2}\left(1-\frac{(l-1)\lambda}{2}\right)\left[\left(1-\frac{(l-1)\lambda}{2}\right)+\left(1-\frac{(l-1)\lambda}{4}\right)\right]\\a_2&=\frac{(l-1)^2\lambda^2}{16}\left[\left(1-\frac{(l-1)\lambda}{2}\right)+4\left(1-\frac{(l-1)\lambda}{4}\right)\right]\\a_3&=\frac{(l-1)^3\lambda^3}{32}\end{aligned} \tag{11}$$

Since a message intended for this buffer can also be generated independently with probability λ by the local processor, the probability of the total number of arrivals being equal to i is given by Equation (12):

$$\lambda a_{i-1} + (1-\lambda)a_i \qquad (i = 0,1,2,3,4) \tag{12}$$

where, $a_{-1} = a_4 = 0$.

Then, after simplification, the balance equations for each buffer can be written as Equation (13):

$$\begin{aligned}
P(0) &= 1 - l\lambda, \\
P(1) &= \big((1-\lambda)a_1 + \lambda a_0\big)\big(P(0)+P(1)\big) + (1-\lambda)a_0 P(2), \\
P(2) &= \big((1-\lambda)a_2 + \lambda a_1\big)\big(P(0)+P(1)\big) \\
&\quad + \big((1-\lambda)a_1 + \lambda a_0\big)P(2) + (1-\lambda)a_0 P(3), \\
P(3) &= \big((1-\lambda)a_3 + \lambda a_2\big)\big(P(0)+P(1)\big) \\
&\quad + \big((1-\lambda)a_2 + \lambda a_1\big)P(2) + \big((1-\lambda)a_1 + \lambda a_0\big)P(3) \\
&\quad + (1-\lambda)a_0 P(4), \\
P(4) &= \lambda a_3\big(P(0)+P(1)\big) + \big((1-\lambda)a_3 + \lambda a_2\big)P(2) \\
&\quad + \big((1-\lambda)a_2 + \lambda a_1\big)P(3) + \big((1-\lambda)a_1 + \lambda a_0\big)P(4) \\
&\quad + (1-\lambda)a_0 P(5),
\end{aligned} \tag{13}$$

$$\begin{aligned}
(1-\lambda)a_0 P(n+1) = \\
&\lambda a_3 P(n-2) + (\lambda a_2 + a_3)P(n-1) \\
&+ (\lambda a \ + a_2 + a_3)P(n), \\
&(n \geq 5)
\end{aligned}$$

The characteristic equation is cubic, as shown in Equation (14):

$$\begin{aligned}
&(1-\lambda)a_0 x^3 - (\lambda a_1 + a_2 + a_3)x^2 \\
&-(\lambda a_2 + a_3)x - \lambda a_3 = 0
\end{aligned} \tag{14}$$

The general solution of the system from Equation (13) has a form given by Equation (15):

$$P(n) = Ax_1^n + Bx_2^n + B^* x_3^n, \quad n \geq 5 \tag{15}$$

where, A, B, and B^* are functions of λ and l; A is real, while B and B^* are complex conjugates; x_1 is the real root of Equation (14); and, x_2 and x_3 are two complex conjugate roots of the characteristic equation. In particular,

$$P(1) = (1 - l\lambda)\left(\frac{32}{(1-\lambda)(2-(l-1)\lambda)(4-(l-1)\lambda)^2} - 1\right)$$

Explicit expressions for larger n are too complex to be written here. However, with some technical contrivances, rather simple explicit expressions for the average number $\bar{n}$ of messages in the buffer, and the average latency τ can be obtained, and are described by Equations (16) and (17):

$$\bar{n} = \frac{\lambda^2(l-1)(11+5l)}{16(1-l\lambda)} + l\lambda \tag{16}$$

$$\tau = \frac{\lambda(l-1)(11+5l)}{16(1-l\lambda)} + l \tag{17}$$

Again, the saturation point is given by Equation (18):

$$\lambda_{crit} = \frac{1}{l} \tag{18}$$

and the critical exponent is equal to 1.

Simulation

The Ring

Simulations were done for rings of length 8 and 16 for several values of l, starting with $l = 2$. After achieving the steady-state regime, the simulation was run for about 50,000 clock cycles at 64 and 256 nodes. Figure 1 shows the probability distribution of the number of messages (queue length) n for the ring length of 8 nodes, $l = 2$, and a near-critical message generation rate of $\lambda = 0.45$. The solid red line represents predicted theoretical values, while the green circles show numerical simulation results.

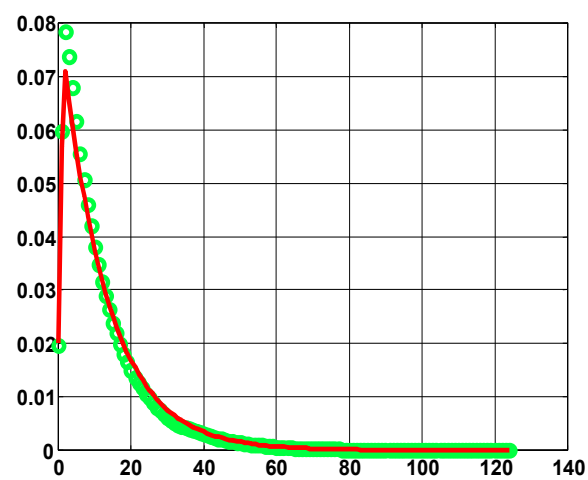

Probabilities $P(n)$

Figure 1. Probability Distribution of the Queue Length

Figure 2 shows the inverse value $1/\bar{n}$ of the average number of messages as a function of the load λ for $l = 2$. The solid red line represents theoretical values given by Equation (8). The numerical simulation results for ring lengths 8 and 16 are shown by crosses and circles, respectively.

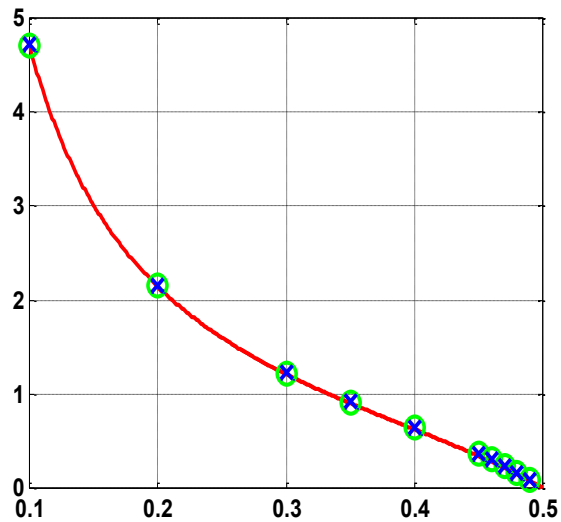

λ (probability message generation)

Figure 2. The Inverse Length of the Queue

Figure 3 shows the inverse values of the latency, $1/\tau$, as a function the network load for $l = 2$. The solid red line represents theoretical values given by Equation (9). The numerical simulation results for ring lengths 8 and 16 are shown as blue crosses and green circles, respectively.

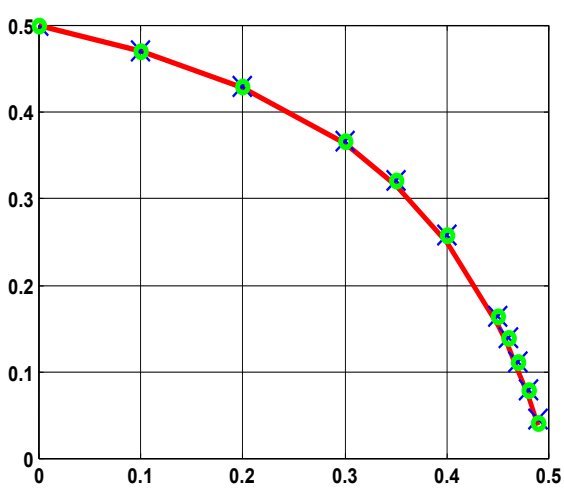

λ (probability message generation)

Figure 3. The Inverse Latency

The Torus

Simulations were done for 16×16 toroidal square lattices for distances $l = 2$ and $l = 5$. The total number of 256´4 buffers were observed at 15,000 points in time with intervals starting with 10 and going up to 400 clock cycles to guarantee the independence of the samples. Sufficient time was allowed for the network to come to the steady-state regime before samples were taken. The probability distribution of the number of messages $\bar{n}$ in one buffer is given in Figure 4 for a torus size of 256 nodes, $l = 5$, and $\lambda = 0.193$. The solid red line represents predicted theoretical values; the blue dashed line represents numerical simulation results.

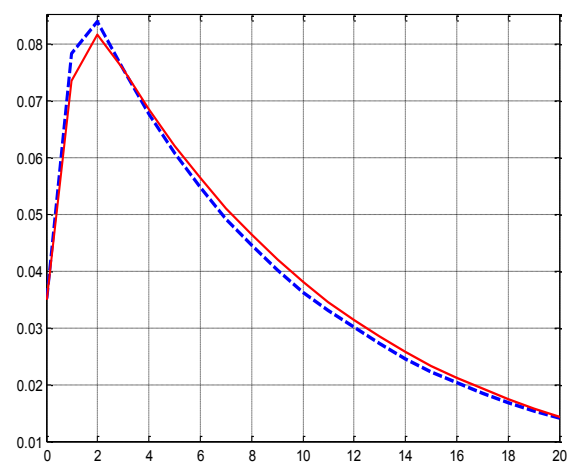

Probabilities $P(n)$

Figure 4. Probability Distribution of the Queue Length

Figure 5 shows the inverse value of the average number of messages, $1/\bar{n}$, as a function of the load λ. The solid red line represents theoretical values given by Equation (16); numerical simulation results for a torus of 256 nodes are shown as blue dots. The standard deviations of the mean values were calculated, but because of the large sampling size, they were too small to be shown in the plot. Figure 6 shows the inverse values of the latency, $1/\tau$. The solid red line represents theoretical values given by Equation (17); numerical simulation results for a 16×16 torus are shown as blue crosses.

Discussion of Results

The results showed an excellent agreement between the theory and numerical experiments. Thus, the presented theoretical model of the network as a system of independent queues provides a very accurate prediction of network be-

havior. This fact is remarkable, since this system has properties different from those for which the product form of the state probability distribution has been proven.

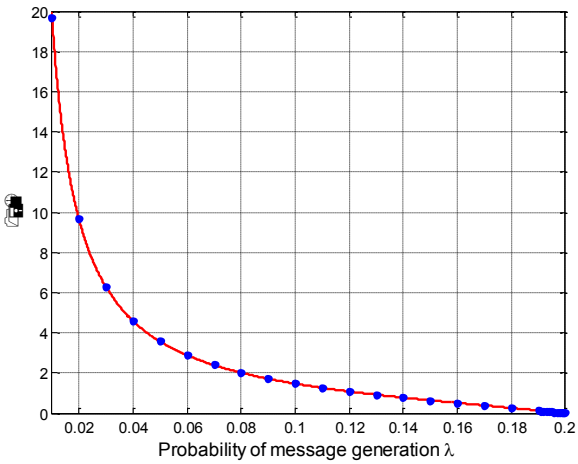

λ (probability of message generation)

Figure 5. The Inverse Length of the Queue for $l = 5$

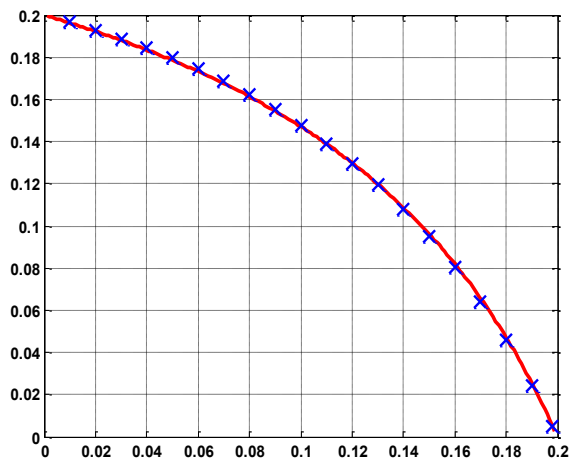

λ (probability of message generation)

Figure 6. The Inverse Average Latency as a Function of Load λ for $l = 5$

The saturation phenomenon in 1-dimensional and 2-dimensional interconnection networks was shown to be a phase transition with a critical exponent equal to 1. From the standpoint of statistical physics, this means that the mean field theory is exact for the types of networks considered. In contrast with physical systems, where critical phenomena are observed only in the "thermodynamic limit," the saturation in networks occurred for finite systems and, moreover, the characteristics of network performance seemingly did not depend on the size the system, provided that the distance l is smaller than the maximum distance between nodes. It was seen that in both 1-dimensional and 2-dimensional cases, the phase transition was continuous (of the second order), and the critical load was inversely proportional to the distance between the source and the destination. This fact is not surprising, since the utilization of every link in the network (the fraction of time when the link is busy) is given by Equation (19):

$$\rho = 1 - P(0) = l\lambda \tag{19}$$

Also, the analysis showed that the choice of the queueing discipline had no effect on network behavior.

Conclusions and Future Work

The results of this study demonstrated the existence of a strong analogy between phenomena in communication networks and in systems studied by statistical physics. It opens a prospect for the development of a consistent physical theory of computer communication systems that would be able to employ the powerful and well-developed apparatus of statistical physics for the analysis and control of the processes in communication networks. The other possible extension of this research would be application of a similar approach to other network topologies, sets of parameters, queueing disciplines, etc.

References

[1] Kleinrock, L. (1975). *Queueing Systems Volume I: Theory*. New York: Wiley.

[2] Kleinrock, L. (1976). *Queueing Systems Volume II: Com. Applications*. New York: Wiley,

[3] Jackson, P. (1963). Job shop like queueing systems. *Management Sci*., *10*(1), 131–142.

[4] Gordon, W. J., & Newell, G. F. (1967). Closed queueing systems with exponential servers. *Oper. Res., 15*, 254-265.

[5] Buzen, J. P. (1973). Computational algorithms for closed queueing networks with exponential servers. *Commun. ACM., 16*(9), 527-531.

[6] Baskett, F., Chandy, K. M., Muntz, R. R., & Palacios, F. G. (1975). Open, closed, and mixed networks of queues with different classes of customers. *J. ACM*, *22*(2), 248-260.

[7] Spirn, J. P. (1979). Queueing networks with random selection for service. *IEEE Trans. Software Eng., SE-5*, 287-289.

[8] Noetzel, A. S. (1979). A generalized queueing discipline for product form network solution. *J. ACM*, *26* (4), 779-793.

[9] Chandy, K. M., & Martin, J. (1983). A characterization of product form queueing networks. *J. ACM*, *30* (2), 286-299.

[10] Reiser, M. (1979). Mean Value Analysis of Queueing Networks—A New Look at an Old Problem. *Proceedings of the Third International Symposium on Modelling and Performance Evaluation of Computer Systems: Performance of Computer Systems*, M. Arató, A. Butrimenko, and Erol Gelenbe (Eds.). North-Holland Publishing Co., Amsterdam, The Netherlands, The Netherlands, 63-77.

[11] Reiser, M., & Lavenberg, S. S. (1980). Mean value analysis of closed multichain queueing networks. *J. ACM*, *27*(2), 313-322.

[12] Reiser, M. (1981). Mean value analysis and convolution method for queueing dependent servers in closed queueing networks. *Perform. Eval.*, *I*(1), 7-18.

[13] Sauer, C. H., & Chandy, K. M. (1981). *Computer Systems Performance Modeling*. Englewood Cliffs, NJ: Prentice-Hall.

[14] Akyildiz, I. F., & Sieber, A. (1988). Approximate analysis of load dependent general queueing networks. *IEEE Transactions on Software Engineering*, *14*(11), 1537-1545.

[15] Nikitin, N., & Cortadella, J. (2009). A performance analytical model for Network-on-Chip with constant service time routers. In *Proceedings of the 2009 International Conference on Computer-Aided Design* (ICCAD '09). ACM, New York, NY, USA, 571-578.DOI=10.1145/1687399.1687506 http://doi.acm.org/10.1145/1687399.168750

[16] Fischer, E., Fehske, A., & Fettweis, G. P. (2012). A flexible analytic model for the design space exploration of many-core network-on-chips based on queueing theory. In *SIMUL 2012, The Fourth International Conference on Advances in System Simulation*, 119-124.

[17] Zhang, Y., Xiaoguo, D., Siqing, G., & Weimin, Z. (2012). A Performance Model for Network-on-Chip Wormhole Routers. *Journal of Computers, 7*(1), 76-84.

[18] Kiasari, A. E., Lu, Z., & Jantsch, A. (2013). An analytical latency model for networks-on chip. *IEEETrans. Very Large Scale (VLSI) Syst.*, *21*(1), 113-123.

[19] Qiu, T., Lin, F., Feng, X., Wu, G., & Yu, Z. (2011). A packet buffer evaluation method exploiting queueing theory for wireless sensor networks. *Computer Science and Information Systems/ComSIS, 8*(4), 1027 -1049.

[20] Nagendrappa, T., Muddenahalli, F., Takawira, F. (2013). Queuing analysis of distributed and receiver-oriented sensor networks: distributed DS-CDMA-based medium access control protocol for wireless sensor networks. *IET Wireless Sensor Systems, 3*(1), 69-79.

[21] Dabrowski, C. (2015). Catastrophic event phenomena in communication networks. *Comput. Sci. Rev.* 18, C (November 2015), 10-45. DOI=http://dx.doi.org/10.1016/j.cosrev.2015.10.001

[22] Sarkar, S., Mukherjee, K., Srivastav, A., & Ray, A. (2009). Understanding phase transition in communication networks to enable robust and resilient control. *2009 American Control Conference*, St. Louis, MO, 1549-1554. doi: 10.1109/ACC.2009.5159994

[23] Sarkar, S., Mukherjee, K., Srivastav, A., & Ray, A. (2010). Critical phenomena and finite-size scaling in communication networks. *Proceedings of the 2010 American Control Conference*, Baltimore, MD, 271-276. doi: 10.1109/ACC.2010.5530594

[24] Sarkar, S., Mukherjee, K., Ray, A., Srivastav, A., & Wettergren, T. A.(2012). Statistical Mechanics-Inspired Modeling of Heterogeneous Packet Transmission in Communication Networks. *IEEE Transactions on Systems, Man, and Cybernetics, Part B (Cybernetics)*, *42*(4), 1083-1094. doi: 10.1109/TSMCB.2012.2186611

[25] Li, W., Bashan, A., Buldyrev, S. V., Stanley, H. E., & Havlin, S. (2012). Cascading failures in interdependent lattice networks: The critical role of the length of dependency links. *Physical review letters*, *108*(22), 228702.

[26] Radicchi, F., & Arenas, A. (2013). Abrupt transition in the structural formation of interconnected networks. *Nature Physics*, *9*(11), 717-720.

[27] Lawniczak, A. T., Lio, P. P., Xie, S., & Xu, J. (2007, April). Study of packet traffic fluctuations near phase transition point from free flow to congestion in data network model. In *2007 Canadian Conference on Electrical and Computer Engineering*. IEEE. 360-363

[28] Dabrowski, C., & Mills, K. (2016). The Influence of Realism on Congestion in Network Simulations. *NIST Technical Note, 1905*, 1-62. http://dx.doi.org/10.6028/NIST.TN.190

[29] Wang, D., Cai, N., Jing, Y., & Zhang, S. (2009, June). Phase transition in complex networks. In *2009 American Control Conference*. IEEE. 3310-3313

[30] Goltsev, A. V., Dorogovtsev, S. N., & Mendes, J. F. F. (2003). Critical phenomena in networks. *Physical Review E*, *67*(2), 026123.

[31] Liu, R. R., Wang, W. X., Lai, Y. C., & Wang, B. H. (2012). Cascading dynamics on random networks: Crossover in phase transition. *Physical Review E*, *85* (2), 026110.

[32] Rykalova, Y., Levitin, L. B., & Brower, R. 2010. Critical phenomena in discrete-time interconnection networks. *Physica A: Statistical Mechanics and its Applications, 389*(22), 5259-5278

[33] Levitin, L. B., Rykalova, Y. (2015). Analysis and Simulation of Computer Networks with Unlimited Buffers. In Al-Sakib Pathan, Muhammad Monowar, and Shafiullah Khan (Eds.) *Simulation Technologies in Networking and Communications*: Selecting *the Best Tool for the Test.* CRC Press 2015, 3-30.
Print ISBN: 978-1-4822-2549-5 eBook ISBN: 978-1-4822-2550-1

Biographies

LEV LEVITIN is a Distinguished Professor of Engineering Science in the Department of Electrical and Computer Engineering at Boston University. He has published over 190 papers, presentations, and patents. His research areas include information theory, quantum communication systems, physics of computation, quantum computing, quantum theory of measurements, mathematical linguistics, theory of complex systems, coding theory, theory of computer hardware testing, reliable computer networks, and bioinformatics. He is a Life Fellow of IEEE, a member of the International Academy of Informatics, and is involved with other professional societies. Professor Levitin may be reached at levitin@bu.edu

YELENA RYKALOVA is currently a visiting researcher with the Department of Electrical and Computer Engineering at Boston University and teaches at UMass Lowell. Her research interests include computer networks, in particular application of concepts and models of statistical physics to the analysis of network performance. She is a member of IEEE and the Society for Modeling and Simulation International (SCS). Since 2008, she has been active in the organization and preparation of the SpringSim Multiconference as a technical committee member, reviewer, and publicity and session chair. Dr. Rykalova may be reached at rykalova@bu.edu

THE ROLE OF ADHESIVE FORCES DURING SEPARATION OF LIQUID-MEDIATED CONTACTS

Prabin Dhital, Minnesota State University, Mankato; Shaobiao Cai, Minnesota State University, Mankato

Abstract

Menisci may form between two solid surfaces in the presence of an ultra-thin liquid film. When a separation operation is needed, meniscus and viscous forces contribute to an adhesion leading to stiction, high friction, possible high wear, and potential failure of the contact systems such as micro-devices, magnetic head disks, and diesel fuel injectors. "The situation may become more pronounced when the contacting surfaces are ultra-smooth and the normal load is small [1, 2]." In this study, the authors investigated the effects of different lubricants on the roles of the meniscus and viscous forces during the separation process for flat-on-flat liquid-mediated contact separation. Also evaluated were the factors that influence any change in role of meniscus and viscous forces.

Introduction

"Menisci may be formed around the contacting and near contacting asperities due to surface energy effect of a thin liquid film, when liquid is present at the contact interface of two surfaces" [3]. A meniscus is formed wherever an asperity touches the liquid. Small amounts of liquid at the point of contact between the solid surfaces are called pendular rings. "During the formation of menisci, pendular rings are formed on contacting surfaces asperities and liquid bridges are formed on near-contacting asperities" [3]. "When liquid mediated contact is considered, the formed menisci are the center of interest." "The geometric description of the meniscus is the meniscus curve. It is formed between the upper and lower surfaces of the liquid when the two surfaces are brought in contact. The shape of the meniscus is determined by the properties of the liquid and solid" [1-3]. "In some cases, the liquid spreads evenly on the surface, and sometimes it forms into tiny droplets. Liquid spreading evenly on the surface with maximizing contact angle is known as hydrophilic phenomenon and liquid forming into a droplet is known as hydrophobic phenomenon."

"The meniscus is convex for a hydrophobic surface, and it is concave for a hydrophilic surface. Attractive force (meniscus force) acts on the interference for hydrophilic surfaces in contact and repulsive meniscus force for hydrophobic surfaces" [1-3]. "The angles formed between the meniscus curve and the contact surfaces are called contact angles. The contact angle can be measured through the liquid where a liquid/gas interface meets the solid surface with sessile drop technique" [2, 4]. The contact angle is an important indicator of the contacting system. For a multi-phase solid, such as liquid and gas system under certain conditions (i.e., different pressures and temperatures), the equilibrium of the system (represented by the unique contact angles) reflects the strength or energy level of the materials. "The formation of the menisci around the contacting and near contacting surface asperities are due to the effect of the surface energy of the liquid film."

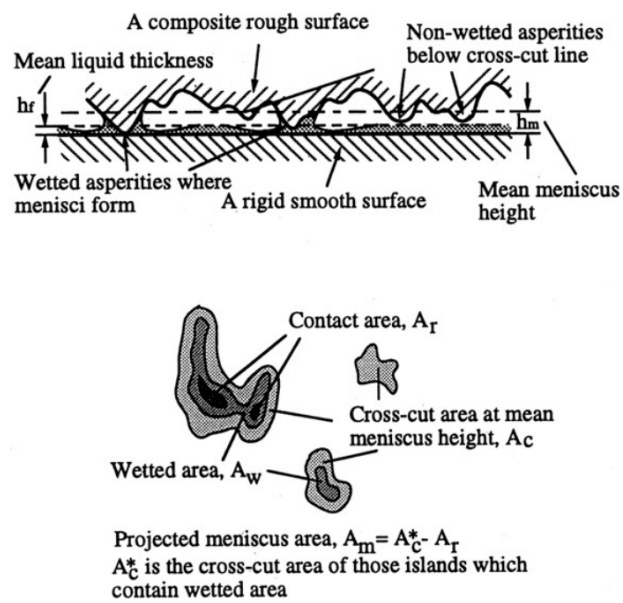

Figure 1. Schematics of Formation of Menisci between Liquid-Mediated Contacts [1-3]

"Meniscus and viscous forces are believed to be the major contributors to adhesion during separation of liquid-mediated contact" [2]. Many studies have been conducted to study the separation of liquid-mediated contacts. Cai and Bushan [5-6] and Cai et al. [7] developed models (CB model) and studied the separation of two flat-on-flat surfaces and sphere-on-flat surfaces. In the CB model, various design parameters, such as contact angle and initial separation height for specified surface tension and liquid viscosity, were investigated. More importantly, it was found that the role of the involved meniscus and viscose forces changes when the so-called critical meniscus area is reached.

The behaviors of a liquid bridge, when compressed and stretched in a quasi-static fashion between two solid surfaces that have contact angle hysteresis (CAH), was studied by Chen et al. [8]. They developed a theoretical model to obtain the profiles of the liquid bridge, given a specific separation between the surfaces, where the model is able to correctly predict the behavior of the liquid bridge during a quasi-static compressing/stretching loading cycle in experiments. It was found that the liquid bridge can have two different profiles at the same separation during one loading and unloading cycle, and more profiles can be obtained during multiple cycles, where maximum adhesion forces are influenced by contact angle hysteresis (CAH).

When a separation of two liquid-mediated contact surfaces is needed, various factors need to be considered in order to characterize the involved forces. The effects of separation distance, initial meniscus height, separation time, and roughness were studied by Cai and Bhushan [1, 3, 5]. Contact angle, as one of the major factors in liquid-mediated contacts, has been studied intensively. The study on adhesion contributed by meniscus and viscous forces during the separation of two hydrophilic smooth surfaces with symmetric and asymmetric contact angles was studied by Cai and Bhushan [3, 5]. In these studies, a critical meniscus area (at which meniscus force equals the viscous force) was first identified and defined as the meniscus area at which meniscus and viscous forces change roles. It was found that, with the increase in separation distance, meniscus forces decrease and the integrative viscous force needed to overcome increases. The increase in initial meniscus height for rough surfaces and the increase in surface roughness cause an increase in meniscus force but do not have a significant effect on the viscous force [5].

A three-dimensional model for liquid-mediated adhesion between two rough surfaces was developed by Rostami and Streator [9] by analyzing the effect of liquid surface tension, nominal contact area, and external load on the stability of contact interface. They found that an increase in external load causes more interaction between contact surfaces, which causes the reduction in the average gap and an increase in separation height and contact area as a result of an increase in tensile force. Wang et al. [10] investigated the effect of various parameters such as the mass and radius of the sphere, viscosity, surface tension, and volume of the liquid during a dynamic separation process for two different configurations (sphere from a flat surface and sphere from a sphere surface). They found that the separation time is longer for sphere-on-sphere surfaces for the same limitations. An increase in mass leads to a decrease in external force, so that separation time increases. Between two configurations, they been found that the influence of the mass and radius of the sphere on separation time are much weaker on sphere-on-sphere separation. An increase in viscosity and surface tension leads to an increase in separation time, and it is determined that the influence of the liquid's viscosity and surface tension on separation time are much weaker in sphere-on-sphere surfaces than that for the sphere-on-flat cases.

For the separation of two surfaces with a formed liquid bridge, an external force larger than the meniscus force is required to initiate the separation process, and higher level forces may be needed to overcome the additional viscous force contribution thereafter. It was noticed that meniscus force decreases, whereas the integrated viscous force over the separation distance from the initial position increases. This indicates that the role of meniscus and viscous forces may be changed during the separation process. This has been numerically verified through the simulation of separation processes [1]. Further, the effects of separation distance, initial meniscus height, separation time, contact angle, division of menisci, and roughness on meniscus and viscous force were analyzed in this current study.

The results showed that the viscous force increases with an increase in separation distance. Initial meniscus height is also one of the major factors affecting the magnitude of viscous forces during the separation process, where the viscous force decreases with an increase in the initial meniscus height. The time taken to break the meniscus during the separation process is the separation time. It is common that the separation time is less than a second, and even at or about the microsecond scale. The longer the separation time, the smaller the magnitude of the viscous force, since the viscous force during the separation process is inversely proportional to the separation time [1-6].

"During the separation of two flat contact surfaces, the viscosity of the liquid causes an additional attractive force, a rate dependent viscous force" [2]. Both the meniscus and viscous forces cause an adhesive force during the separation. "When separation operation of two contact surfaces is needed, adhesion due to the meniscus and viscous force is one of the major reliability issues leading to failure or reduction in the consistency of devices such as diesel fuel injectors in operation." "The issue becomes more severe when the applied load is small (which is common) for micro or nanoparticle devices. The force required to separate two surfaces is dependent on both meniscus and viscous forces" [1, 3, 5]. It was found that this type of adhesive force is highly dependent on the formed meniscus area (neck cross-sectional area at a given meniscus height, which overlaps the wetted area), separation time, surface tension, and viscosity of the liquid. During the separation process, the meniscus force decreases, whereas the integrated viscous force

(to be overcome) over the separation distance from the initial position increases. The roles of the two forces change before the surfaces are separated.

Although the effects on meniscus and viscous forces contributing to adhesion during separation of liquid-mediated contacts have been studied, the role of changes of the contributing forces have not been adequately investigated. It is known that a critical meniscus area determines the role change of the forces. However, questions such as how the critical meniscus area changes with a change in the affecting factors, such as liquid properties, need to be answered in order to effectively solve issues associated with adhesion. In this paper, the authors present a comprehensive study of the roles of meniscus and viscous forces with the critical meniscus area (at which meniscus force equals the viscous force) during liquid-mediated contact separation. The effect on critical meniscus area with a change in viscosity and surface tension were studied for flat-on-flat liquid-mediated contact separation.

Approaches

As part of the data collection procedure, an established mathematical model was simulated in MATLAB in order to analyze the roles of the meniscus and viscous forces, considering the liquid properties as silicon oil. Figure 2 shows the configuration of the meniscus formed between flat-on-flat contact surfaces.

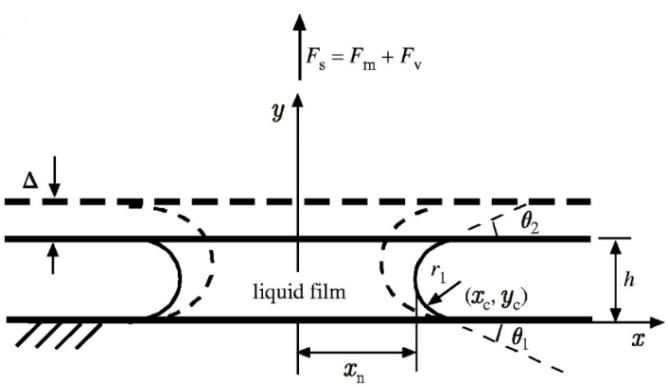

Figure 2. Formation of a Liquid Bridge with Hydrophilic Flat-on-Flat Liquid-Mediated Surface Contact Separation [1, 2]

Meniscus Force

"The meniscus force on flat on flat contact due to the formation of a meniscus is obtained by integrating the Laplace pressure over the meniscus area and adding the surface tension effect acting on the circumference of the interface" [5], which can be represented by Equations (1) and (2):

$$F_m = F_L + F_T \tag{1}$$

$$F_m = \pi\chi_n^2 \frac{\gamma}{\kappa_k} + 2\pi\gamma\chi_n \sin\theta_{1,2} \tag{2}$$

where,

F_s	is the external force needed to overcome the intrinsic forces contributed by the meniscus force.
F_m	is the meniscus force.
F_v	is the viscous force.
F_L	is the attractive force due to Laplace.
F_T	is the attractive force due to surface tension.
h	is the separation height.
γ	is the liquid surface tension.
r_1	is the radii of the meniscus in orthogonal plane.
X_n	is the discrete meniscus radius at time step n.
θ	is the contact angle.
$\theta_{1,2}$	is the contact angle between solid surface and meniscus for the upper and lower surfaces, respectively.
κ_k	is the kelvin radius.
x_c, y_c	are the center coordinates.

The meniscus height WAS calculated using Equation (3):

$$h = r_k\left(\cos\theta_1 + \cos\theta_2\right) \tag{3}$$

The meniscus force, in terms of separation height, can be calculated by using Equation (4):

$$F_m = \frac{\pi\chi_n^2\gamma(\cos\theta_1 + \cos\theta_2)}{h} + 2\pi\gamma\chi_n \sin\theta_{1,2} \tag{4}$$

Viscous Force

"Viscous force occurs due to the presence of viscosity when two surfaces are separated within a short time" [1]. Characterization of the viscous force is important in order to estimate the total force needed to separate two liquid-mediated contact surfaces. The equation for viscous force during the separation of flat-on-flat surfaces was derived by using the Reynold's lubrication equation with a cylinder coordinate system [5], as given by Equation (5):

$$\frac{\partial}{\partial r}\left(rh^3\frac{\partial p}{\partial r}\right) = 12\eta r\frac{dh}{dt} \tag{5}$$

where, η is a kinematic viscosity; h is the separation distance; and, r is an arbitrary distance (the same as X_n, as shown in Figure 2) in the central plane of the meniscus in the direction of separation.

For the separation of two smooth, flat surfaces, the viscous force during the separation of two flat-on-flat surfaces at a given separation height is given by Equation (6) [4]:

$$F_v = \frac{3\pi\eta\chi_{ni}^4}{4t_s}\left(\frac{1}{h_s^2} - \frac{1}{h_0^2}\right) \quad (6)$$

where, t_s is the time to separate the two surfaces; h_s is the break point, which is infinite (theoretically) during the separation; and, h_o is the initial gap between the two flat surfaces.

"Both the meniscus and viscous force is operating inside the meniscus during the separation process in surface contact" [1, 3, 5]. So the condition like the asymmetric angles, division meniscus, separation time, and height can significantly affect the properties of the meniscus and viscous forces during the separation. An external force is required to initiate the separation process. "During the break point external force should be larger than total of meniscus and viscous force" [2]. Through the contact of the two liquid-mediated surfaces, if the meniscus force is larger than the viscous force, the meniscus will slowly break without the application of external forces; however, the time to separate is longer.

Results and Discussion

"It is known that larger meniscus area leads to larger meniscus and viscous force." "Critical meniscus area (at which meniscus force equals the viscous force) is a function of surface tension, which increases with increase in surface tension" [2]. The critical meniscus area and the forces exhibit a nonlinear relationship when the surface tension is changed. In order to establish the relationship between viscosity and surface tension with the critical meniscus area at which the forces change the role, an analysis was performed on silicon oil at room temperature at a viscosity of 0.4860 Ns/m^2, a surface tension of 0.0633 N/m, and a separation time of 1 second, with a contact angle of 60°. Initially, the preliminary value of the liquid's viscosity and surface tension at room temperature were inserted into Equations (4) and (6), during flat-on-flat contact separation and solved numerically. The resulting critical meniscus area, and meniscus and viscous force values were recorded. The simulation gave the values of critical meniscus area at different heights (2 nm to 6 nm) for corresponding meniscus and viscous forces for different liquid properties. Each time the values of the different liquid properties were inserted, the simulation program gave the corresponding value of the meniscus and viscous forces, and a critical meniscus area, which was noted for further analysis.

The symbols ●■▲♦○ represent the critical meniscus area values for different viscosities and surface tension values for initial meniscus height, which varied from 2 nm to 6 nm, respectively, and the highlighted dashed box on left side of the graph represents the initial critical meniscus area for different initial meniscus heights for silicon oil (η_o=0.4860 Ns/m^2 and γ= 0.0633 N/m) at room temperature during flat-on-flat liquid-mediated contact separation. In order to study the effect of viscosity, the initial value of the liquid properties was taken as silicon oil (η_o=0.4860 Ns/m^2 and γ= 0.0633 N/m). The initial value of the surface tension was kept constant at 0.0633N/m, while the viscosity value was increased at 5% intervals from its initial value. Each time, the constant surface tension value of 0.0633N/m and the resulting increase in viscosity value were inserted into the simulation program.

For example, an increase of 5% of the initial viscosity yielded 0.510 Ns/m^2, and 10% of the initial viscosity yielded 0.535 Ns/m^2; hence, the new liquid properties of 0.0633N/m and 0.510Ns/m^2, 0.0633N/m and 0.535 Ns/m^2, and so on, were inserted into the program. To analyze the effect of surface tension, the initial value of the liquid properties was also taken as silicon oil (η_o=0.4860 Ns/m^2 and γ= 0.0633 N/m). The initial value of viscosity was kept constant at 0.4860 Ns/m^2; however, the surface tension value was increased in increments of 5%, starting from its initial value. Each time, the constant viscosity value of 0.4860 Ns/m^2 and the resulting increase in surface tension value were inserted into the simulation program. For example, an increase of 5% of the initial surface tension yielded 0.0665 N/m, and 10% of the initial viscosity yielded 0.0696 N/m; hence, the new liquid properties of 0.0665N/m and 0.4860Ns/m^2, 0.0696N/m and 0.4860 Ns/m^2, and so on, were inserted into the program. Table 1 shows the corresponding increase in viscosity and surface tension values compared to initial values. These different viscosity and surface tension values were used for meniscus and viscous force calculations, and the critical meniscus areas were recorded for different initial heights.

To study the effect of liquid properties, the viscosity value was increased in 5% increments up to 40%, then 50% and 100% (see Figure 3) from the initial value of the surface tension constant (0.0633 N/m). Figure 3 shows the effect of liquid viscosity on the critical meniscus area during flat-on-flat liquid-mediated contact separation. It also shows the effect of increasing viscosity of the liquid on constant surface tension. "It is observed that initial meniscus height and viscosity of the liquid have a significant effect on the critical meniscus area. The results show that with the contact angles of Θ_1 and Θ_2 as 60°, any increase in the initial menis-

cus heights leads to a larger critical meniscus area for the same viscosity." "This is because a larger initial meniscus height leads to a much faster decrease in viscous force compared to the meniscus force so a larger meniscus area is needed for the viscous force to become comparable to the meniscus force, which explained previously" [2]. The ratio of the increase of critical meniscus area for increasing viscosity was always same for 2 nm to 3 nm, 3 nm to 4 nm, 4 nm to 5 nm, and 5 nm to 6 nm separation heights. The results show that changing the critical area from 5 nm to 6 nm had a higher ratio, followed by 4 nm to 5 nm, 3 nm to 4 nm, and 2 nm to 3 nm. It was observed that critical meniscus area decreased with an increase in viscosity. The decrease in critical meniscus area resulted in a decrease in meniscus force. From Figure 3, it can also be observed that the change in the critical meniscus area from 2 nm to 6 nm initial separation was almost constant as viscosity increased.

Table 1. Viscosity and Surface Tension after Increasing the

Initial Viscosity and Surface Tension at Room Temperature for Silicon Oil	η_o= 0.4860 Ns/m^2	γ_o = 0.0633 N/m
Increased percentage with initial value	Viscosity (Ns/m^2)	Surface tension (N/m)
5%	0.510	0.0665
10%	0.535	0.0696
15%	0.559	0.0728
20%	0.583	0.0760
25%	0.608	0.0791
30%	0.632	0.0823
35%	0.656	0.0855
40%	0.680	0.0886
50%	0.729	0.0950
100%	0.972	0.1266

Initial Value at Room Temperature

To study the effect of surface tension, the liquid viscosity value of η_o=0.4860 Ns/m^2 at room temperature was kept constant and the surface tension was increased. The surface tension value was increased 5% increments up to 40%, then 50% and 100% (see Figure 4). Figure 4 also shows the effect of liquid surface tension on critical meniscus area during flat-on-flat liquid-mediated contact separation. It was observed that initial meniscus height and surface tension of the liquid had a significant effect on the critical meniscus area. The results also showed that with the contact angles of Θ_1 and Θ_2 at 60°, an increase in the initial meniscus heights leads to a larger critical meniscus area for same surface tension. "This is because a larger initial meniscus height leads to a much faster decrease in viscous force compared to the meniscus force" [2]. Thus, a larger meniscus area is needed for the viscous force to be comparable to the meniscus force. The ratio of the increase of critical meniscus area for increasing surface tension is also always the same for 2 nm to 3 nm, 3 nm to 4 nm, 4 nm to 5 nm, and 5 nm to 6 nm separation heights. The results showed that changing the critical meniscus area from 5 nm to 6 nm had a higher value followed by 4 nm to 5 nm, 3 nm to 4 nm, and 2 nm to 3 nm, the same as the viscosity analysis in Figure 3. It was observed that the critical meniscus area moved to a higher value with an increase in surface tension. From Figure 4, one can also conclude that the change in the critical area from 2 nm to 6 nm initial separation is constant, as surface tension increases.

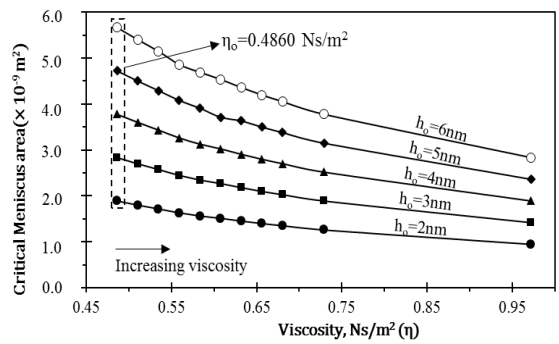

Figure 3. Dimensional Relationship between Viscosity and Critical Meniscus Area at Contact Angles $\theta_1 = \theta_2 = 60^o$, Constant γ with 0.0633 N/m (silicon oil) for Separation Time = 1s. Note: η_o = 0.4860 Ns/m^2. Initial Meniscus Area = 8.50×10^{-10}m^2

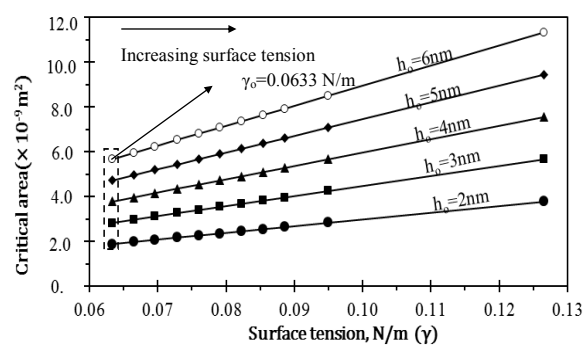

Figure 4. Relationship between Surface Tension and Critical Area with Contact Angles $\theta_1 = \theta_2 = 60^o$, Constant η with 4860 Ns/m^2 (silicon oil) for Separation Time = 1s. Note: γ_o = 0.0633 N/m

Figure 5 shows the relationship between meniscus and viscous forces with critical meniscus area and the corresponding effects of viscosity and separation height. It was

observed that critical meniscus area decreased with an increase in liquid viscosity for the cases where the surface tension was constant with constant initial meniscus height. This was due to the most rapid increase in viscous force when the viscosity of the liquid is higher. Thus, viscous force can dominate at smaller critical meniscus areas. It was also noticed that the lower initial meniscus height had a smaller critical meniscus area. In addition, the rate of decrease in critical meniscus area was also smaller for a lower initial meniscus height, when the liquid viscosity was increased.

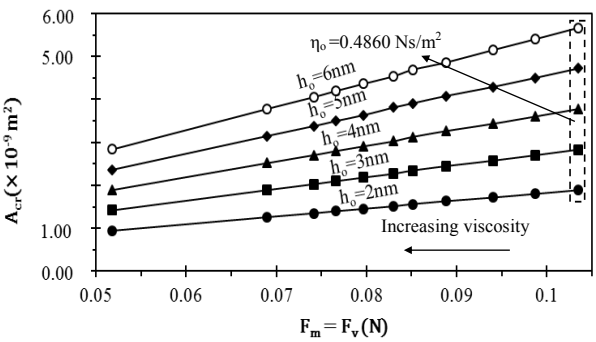

Figure 5. Relationship between Meniscus Force and Critical Area with Contact Angles $\theta_1 = \theta_2 = 60^o$, Constant η (0.4860 Ns/m^2) for Separation Time = 1s. Note: γ_o = 0.0633 N/m (silicon oil) [2]

Figure 6 presents the relationship between meniscus and viscous forces, as a function of critical meniscus area with the effect of surface tension and separation height. The figure also shows the effects of initial meniscus height and surface tension on the critical meniscus area in a dimensional analysis. It was observed that, for a constant initial meniscus height, the critical meniscus area (at which meniscus force equals the viscous force) increased with an increase in liquid surface tension. The lower initial meniscus height had a smaller critical meniscus area. In addition, the rate of increase in critical meniscus area was also smaller for a lower initial meniscus height. This confirmed the observations made previously. These observations indicated that viscous force may be likely to take a dominant role, when initial meniscus height is smaller.

Conclusion

In this paper, the authors present a study of critical meniscus area at which meniscus and viscous forces change roles during flat-on-flat liquid-mediated contact separation. It was observed that the critical meniscus area depends upon contact configurations such as viscosity, surface tension, and separation height.

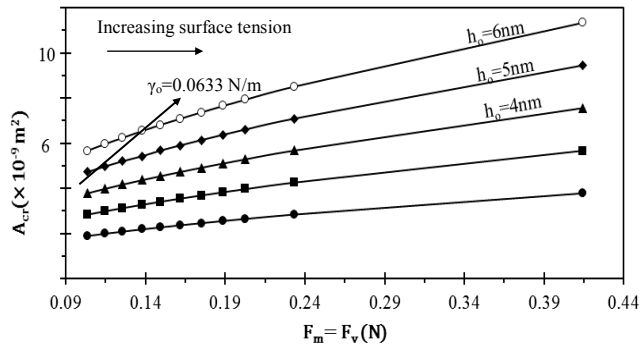

Figure 6. Relationship between Meniscus Force and Critical Area with Contact Angles $\theta_1 = \theta_2 = 60^o$, Constant η (0.4860 Ns/m^2) for Separation Time = 1s. Note: γ_o=0.0633 N/m (silicon oil) [2]

For the same separation time, initial meniscus height, change in viscosity, and surface tension of the liquid had a significant effect on the critical meniscus area. Critical meniscus area decreased at a higher rate for the higher separation height (i.e., 6 nm) followed by decreasing initial separation (5 nm, 4 nm, 3 nm, and 2 nm). Also, it was observed that critical meniscus area decreased as the viscosity increased. The change in the critical meniscus area from 2 nm to 6 nm initial separation height was almost constant, as viscosity increased. With the increase in surface tension, critical meniscus area increased and the change in critical meniscus area from 2 nm to 6 nm initial separation was nearly constant. The critical meniscus area always increased with an increase in initial separation for a fixed viscosity or surface tension. For a fixed initial separation, the critical meniscus area decreased with an increase in viscosity, but increased with an increase in surface tension.

The increase or decrease in meniscus and viscous forces during liquid-mediated contact separation were significantly affected by changes in meniscus area. These two types of forces were comparable, when the critical meniscus area was reached. The domination of either meniscus force or viscous force depends on the size of the critical meniscus area.

References

[1] Cai, S., & Bhushan, B. (2007). Meniscus and viscous forces during normal separation of liquid-mediated contacts. *Nanotechnology*, 465-704.

[2] Cai, S., Dhital, P., & Zhao, Y. (2015). Interfacial Adhesion due to Liquid Mediated Contact of Hydrophilic Solid Surfaces. *Proceedings of the 2015 Inter-*

national Conference on Structural, Mechanical and Material Engineering.

[3] Cai, S., & Bhushan, B. (2008). Meniscus and Viscous Forces during Separation of Hydrophilic and Hydrophobic Smooth/rough Surfaces with Symmetric and Asymmetric Contact Angles. *Philos. Trans. A Math. Phys. Eng. Sci., 366*(1870), 1627-1647.

[4] Orr, F. M., Scriven, L. E., & Rivas, A. P. (1975). Pendular rings between solids: meniscus properties and capillary force. *J. Fluid Mech., 67*, 723- 742.

[5] Cai, S., & Bhushan, B. (2008). Viscous force during tangential separation of meniscus bridges. *Philosophical Magazine*, *88*(3), 449-461.

[6] Cai, S., & Bhushan, B. (2008). Meniscus and viscous forces during separation of hydrophilic and hydrophobic surfaces with liquid-mediated contacts. *Material Science and Engineering-R*, *61*(1-6), 78-106.

[7] Cai, S., Zhao, Y., & Bhushan, B. (2009). Dry and wet contact analyses for the study of friction and wear trends. *Proceedings* of *the Society of Tribologists and Lubrication Engineers Annual Meeting and Exhibition,* 326-328.

[8] Chen, H., Amirfazli, A., & Tang, T. (2013). Modeling Liquid Bridge between Surfaces with Contact Angle Hysteresis. *Langmuir*, 3310-3319.

[9] Rostami, A., & Streator, J. L. (2015). Study of Liquid -mediated Adhesion between 3D Rough Surfaces: A Spectral Approach. *Tribology International*, *84*, 36-47.

[10] Wang, L., Rong, W., Guo, B., Huang, G., & Sun, L. (2011). Dynamic Separation of a Sphere from a Flat or Sphere in the Presence of a Liquid Meniscus. *Tribology Transactions*, 542-547.

Biographies

PRABIN DHITAL is a graduate student in the Department of Mechanical and Civil Engineering at Minnesota State University, Mankato. He is currently pursuing his master's degree in Mechanical Engineering. He earned his bachelor's degree in Mechanical Engineering from Kathmandu University, Nepal. His areas of interest include mechanical system design and modeling, application of DFMA principles for mechanical design, CAD modeling, and manufacturing processes. He is a student member of the American Society of Mechanical Engineers (ASME). Mr. Dhital may be reached at prabin.dhital@mnsu.edu

SHAOBIAO CAI is an assistant professor in the Department of Mechanical and Civil Engineering at Minnesota State University, Mankato. His areas of interest include material design and manufacturing. His areas of expertise and research interest include interfacial contact mechanics and tribology, mechanical failure of materials, layered medium and design, hydrophobic and hydrophilic micro/nano roughness modeling/fabrication and their various multidisciplinary applications, and the application of DFMA principles in the development of robust design solutions. He is a registered professional engineer in the state of Minnesota. He is a member of the American Society of Mechanical Engineers (ASME) and the Society of Tribologists and Lubrication Engineers (STLE). Dr. Cai may be reached at shabiao.cai@mnsu.edu

INSTRUCTIONS FOR AUTHORS: MANUSCRIPT REQUIREMENTS

The INTERNATIONAL JOURNAL OF MODERN ENGINEERING is an online/print publication designed for Engineering, Engineering Technology, and Industrial Technology professionals. All submissions to this journal, submission of manuscripts, peer-reviews of submitted documents, requested editing changes, notification of acceptance or rejection, and final publication of accepted manuscripts will be handled electronically. The only exception is the submission of separate high-quality image files that are too large to send electronically.

All manuscript submissions must be prepared in Microsoft Word (.doc or .docx) and contain all figures, images, and/or pictures embedded where you want them and appropriately captioned. Also, for all accepted manuscripts, each figure, image, or picture that was imported into your Word document must be saved individually as a **300dpi or higher JPEG (.jpg)** file and submitted separately; your manuscript and figure numbers must be used in the title of the file (e.g., **M12-S-18 Figure 4**); that means one additional file for each image imported into your manuscript. These 300dpi images do NOT need to be embedded in your manuscript. For tables or graphs created directly in Word, you do not need to submit them as separate files.

Included below is a summary of the formatting instructions. You should, however, review the sample Word document on our website for details on how to correctly format your manuscript. The editorial staff reserves the right to edit and reformat any submitted document in order to meet publication standards of the journal.

The references included in the References section of your manuscript must follow APA-formatting guidelines. In order to help you, the sample Word document also includes numerous examples of how to format a variety of scenarios. Keep in mind that an incorrectly formatted manuscript will be returned to you, a delay that may cause it (if accepted) to be moved to a subsequent issue of the journal.

1. **Word Document Page Setup**: Two columns with ¼" spacing between columns; Top of page = ¾"; Bottom of page = 1" (from the top of the footer to bottom of page); Left margin = ¾"; Right margin = ¾".

2. **Paper Title**: Centered at the top of the first page with a 22-point Times New Roman (Bold), Small-Caps font.

3. **Page Breaks**: Do not use page breaks.

4. **Body Fonts**: Use 10-point Times New Roman (TNR) for body text throughout (1/8" paragraph indention); 9-point TNR for author names/affiliations under the paper title; 16-point TNR for major section titles; 14-point TNR for minor section titles; 9-point TNR BOLD for caption titles for tables and figures; other font sizes as noted in the sample document.

5. **In-text Referencing**: List and number each reference when referring to them in the body of your document (e.g., [1]). The first entry must be [1] followed by [2], [3], etc., continuing in numerical order to the final entry in your References section. Again, see the sample Word document for specifics. Do not use the End-Page Reference utility in Microsoft Word. You must manually place references in the body of the text.

6. **Tables and Figures**: Center all tables and figures. Captions for tables must be above the table, while captions for figures are below; all captions are left-justified.

7. **Page Limit**: Manuscripts should not be more than 15 pages (single-spaced, 2-column format).

8. **Page Numbering**: Do not use page numbers.

9. **Publication Charges:** Manuscripts accepted for publication are subject to mandatory publication charges.

10. **Copyright Agreement:** Review the **copyright transfer agreement**.

11. **Submissions:** All manuscripts and associated files must be submitted electronically; the only exception would be if you wish to submit a CD with the individual files for your high-quality images, as noted above.

    MANUSCRIPTS should be submitted to Dr. Philip D. Weinsier, manuscript editor, at philipw@bgsu.edu along with a copy to editor@ijme.us.

    FILES containing your high-quality images should ONLY be submitted to philipw@bgsu.edu.

CUTTING EDGE JOURNAL OF RESEARCH AND INNOVATION IN ENGINEERING

www.ijeri.org

Print ISSN: 2152-4157
Online ISSN: 2152-4165

www.iajc.org

INTERNATIONAL JOURNAL OF ENGINEERING RESEARCH AND INNOVATION

ABOUT IJERI:

- IJERI is the second official journal of the International Association of Journals and Conferences (IAJC).
- IJERI is a high-quality, independent journal steered by a distinguished board of directors and supported by an international review board representing many well-known universities, colleges, and corporations in the U.S. and abroad.
- IJERI has an impact factor of **1.58**, placing it among an elite group of most-cited engineering journals worldwide.

OTHER IAJC JOURNALS:

- The International Journal of Modern Engineering (IJME) For more information visit www.ijme.us
- The Technology Interface International Journal (TIIJ) For more information visit www.tiij.org

IJERI SUBMISSIONS:

- Manuscripts should be sent electronically to the manuscript editor, Dr. Philip Weinsier, at philipw@bgsu.edu.

  For submission guidelines visit www.ijeri.org/submissions

TO JOIN THE REVIEW BOARD:

- Contact the chair of the International Review Board, Dr. Philip Weinsier, at philipw@bgsu.edu.

  For more information visit www.ijeri.org/editorial

INDEXING ORGANIZATIONS:

- IJERI is currently indexed by 16 agencies. For a complete listing, please visit us at www.ijeri.org.

Contact us:

Mark Rajai, Ph.D.

Editor-in-Chief
California State University-Northridge
College of Engineering and Computer Science
Room: JD 4510
Northridge, CA 91330
Office: (818) 677-5003
Email: mrajai@csun.edu

www.tiij.org

www.ijme.us

THE LEADING JOURNAL OF ENGINEERING, APPLIED SCIENCE AND TECHNOLOGY

The latest impact factor (IF) calculation (Google Scholar method) for IJME of 3.0 moves it even higher in its march towards the top 10 engineering journals.

IJME IS THE OFFICAL AND FLAGSHIP JOURNAL OF THE INTERNATIONAL ASSOCATION OF JOURNALS AND CONFERENCE (IAJC)
www.iajc.org

The International Journal of Modern Engineering (IJME) is a highly-selective, peer-reviewed journal covering topics that appeal to a broad readership of various branches of engineering and related technologies. IJME is steered by the IAJC distinguished board of directors and is supported by an international review board consisting of prominent individuals representing many well-known universities, colleges, and corporations in the United States and abroad.

IJME Contact Information

General questions or inquiries about sponsorship of the journal should be directed to:

Mark Rajai, Ph.D.
Editor-in-Chief
Office: (818) 677-5003
Email: editor@ijme.us
Department of Manufacturing Systems Engineering & Management
California State University-Northridge
18111 Nordhoff St.
Northridge, CA 91330